

An Efficient Computational Method for Thermal Radiation in Participating Media

by

Pedram Hassanzadeh

A thesis
presented to the University of Waterloo
in fulfilment of the
thesis requirement for the degree of
Master of Applied Science
in
Mechanical Engineering

Waterloo, Ontario, Canada, 2007

© Pedram Hassanzadeh 2007

I hereby declare that I am the sole author of this thesis. This is a true copy of the thesis, including any required final revisions, as accepted by my examiners.

I understand that my thesis may be made electronically available to the public.

Abstract

Thermal radiation is of significant importance in a broad range of engineering applications including high-temperature and large-scale systems. Although the governing equations of thermal radiation have been known for many years, the complexities inherent in the phenomenon, such as the multidimensionality and integro-differential nature of these equations, have made it difficult to obtain an accurate, efficient, and robust computational method. Developing the finite volume radiation method in the 1990s was a significant progress but not a panacea for computational radiation. The major drawback of this method, which is common among all methods that solve for directional intensities, is its slow convergence rate in many situations which increases the solution cost dramatically. These situations include large optical thicknesses, strongly reflecting boundaries, and any other factor that causes strong directional coupling like complex geometries.

Several acceleration schemes have been developed in the heat transfer and neutron transport communities to expedite the convergence and reduce the solution cost, but none of them led to a general and reliable method. Among these available schemes, the two most promising ones, the multiplicative scheme and coupled ordinates method, suffer from failing on fine grids and being very complicated for complex scattering phase functions, respectively.

In this research, a new computational method, called the Q_L method, has been introduced. The main idea of this method is using the phase weight concept to relate the directional and average intensities and re-arranging the Radiative Transfer Equation to find a new expression for the radiant heat flux. This results in an elliptic-type equation for the average intensity at each control volume which conserves the radiant energy in all directions in the control volume. This formulation gives the Q_L method a great advantage to solve for the average intensity while including the directional effects. Since the directional effects are included and the radiant energy is conserved in each control volume, this method is expected to be accurate and have a good convergence rate in all conditions. The phase weight distribution required by the Q_L method can be provided by a method like the finite volume method or discrete ordinates method.

The Q_L method is applied to several 1D and 2D test cases including isotropic and anisotropic scattering, black and partially reflecting boundaries, and emitting-absorbing problems; and its accuracy, convergence rate, and solution cost are studied. The method has been found to be very stable and efficient, regardless of grid size and optical thickness. This method establishes very accurate predictions on the tested coarse grids and its results approach the exact solution with grid refinement.

Acknowledgments

I would like to deeply thank my supervisor, Prof. George Raithby, for his help, guidance, kindness, and especially, for our enlightening and informative discussions. Working with him was an inspiring and enjoyable experience.

I want to express my gratitude to Dr. Eddy Chui from CANMET for his support, and for partially funding this research. I would also like to thank Prof. Gordon Stublely for attentively and patiently answering my questions. Special thanks are extended to Prof. Vahid Esfahanian and Prof. Ali Ashrafizadeh for their encouragement and guidance. Financial supports from CANMET, NSERC, and the University of Waterloo are gratefully acknowledged.

Furthermore, my thanks go to my friends and colleagues Arash Tajik, Sara Toutiaie, Mohsen Shahini, Arman Hajati, Ahmad El Sayed, Mehdi Dargahi, William Chung, Nader Nouroozi, Azad Qazi Zade, Arash Raessi, and Meghdad Saffaripour who made these two years very joyful and rewarding.

Above all, I want to thank my wonderful family, my parents Hossein and Safa, and my sister Pegah, for their care, patience and endless love. This thesis is dedicated to them.

Contents

1	Introduction	1
1.1	Radiative Transfer Equation	2
1.1.1	Review of Computational Radiation Methods	4
1.2	The Finite Volume Radiation Method	6
1.2.1	The Discrete Equations	6
1.2.2	Isotropic Scattering	11
1.2.3	Radiative Equilibrium	12
1.3	Iterative Solution	12
1.4	Acceleration Schemes	13
1.5	Objectives of this Study	14
1.6	Main Approximations	15
1.7	Outline of the Thesis	15
2	The Q_L Method	16
2.1	Mathematical Formulation	16
2.1.1	The Radiation Energy Equation	16
2.1.2	The Equation for $\mathbf{q}(\mathbf{r})$	17
2.1.3	Approximate Equations for $\mathbf{q}(\mathbf{r})$ in the Interior	20
2.1.4	Equation for q_{ip} at Boundary Integration Points	21
2.2	The Discrete Equation	22
2.3	Solution Procedure	23

2.4	Accuracy and Efficiency	25
2.4.1	Accuracy	25
2.4.2	Computational Cost	26
2.5	Concluding Remarks	27
3	The Numerical Solution	28
3.1	Geometry	28
3.2	Computational Grid	28
3.3	Solver	31
3.3.1	The Q_L Equations	31
3.3.2	The FVM Equations	32
3.4	Convergence Criterion for Cycle	33
4	Results	37
4.1	One-Dimensional Problems	38
4.1.1	Isotropic Scattering	40
4.1.2	Anisotropic Scattering	45
4.1.3	Isothermal Slab	49
4.2	Two-Dimensional Problems	49
4.2.1	Pure Isotropic Scattering	52
4.2.2	Absorbing-Scattering Medium	66
4.2.3	Pure Anisotropic Scattering	69
4.2.4	Isothermal Absorbing-Emitting Medium	72
4.2.5	Robustness	76
5	A New Differencing Scheme	78
5.1	Review of the Existing Differencing Schemes	78
5.2	Mathematical Formulation	80
5.3	Numerical Solution	82
5.4	Results	82

5.4.1	Square Enclosure	83
5.4.2	Rectangular Enclosure	90
5.5	Concluding Remarks	91
6	Summary	94
6.1	Future Directions	96
A	The Multiplicative Method	104
A.1	Formulation of the Multiplicative Method	104
A.2	Performance and Failure	105
A.3	The Breakdown	107
A.3.1	Illustrative Example	108
A.4	Other Differencing Schemes	115
A.5	Concluding Remarks	116
B	Two-Dimensional Discretization	117
B.1	Interior Control Volumes	117
B.2	Boundary Control Volumes	126
B.3	The In-Scattering Term	127
C	Acceleration of the P_1 Solution	129
C.1	The P_1 Equations	130
C.2	Correction Method	130
C.3	Test Case	132
C.4	Concluding Remarks	134

List of Figures

1.1	The control volume used to derive the RTE.	3
1.2	A control volume and its panels and integration points.	8
1.3	A control volume and its integration points to demonstrate the UDS.	10
1.4	Two typical solid angle distributions for $L = 48$	11
2.1	A 2D boundary control volume and its integration points.	23
3.1	The geometry: a 2D rectangular enclosure.	29
3.2	An element and a control volume in a 2D Cartesian grid.	30
3.3	A 4×5 grid for a rectangular enclosure.	31
3.4	Four sweeping patterns for a rectangular enclosure.	34
3.5	The complete solution procedure of the Q_L method.	36
4.1	Geometry of the 1D problems.	38
4.2	Four levels of the spatial mesh used in the multigrid solver in the 1D problems.	39
4.3	Nondimensional heat transfer on the hot bottom surface for a purely isotropically scattering plane medium enclosed between two parallel black surfaces (Case 1).	41
4.4	The UDS approximaion in a strongly participating medium.	42
4.5	Number of cycles required to achieve convergence for a purely isotropically scattering plane medium enclosed between two parallel black surfaces (Case 1).	44

4.6	Nondimensional heat transfer on the hot bottom surface for a purely isotropically scattering plane medium enclosed between two parallel partially reflecting surfaces (Case 2).	46
4.7	Number of cycles required to achieve convergence for a purely isotropically scattering plane medium enclosed between two parallel partially reflecting surfaces (Case 2).	47
4.8	Reflectance on the hot bottom surface for a purely scattering plane medium, with a linear phase function, enclosed between two parallel black surfaces (Case 3).	48
4.9	Reflectance on the hot bottom surface for a purely scattering medium, with a non-linear phase function, enclosed between two parallel black surfaces (Case 4).	50
4.10	Nondimensional heat transfer on the bottom surface of an isothermal slab (Case 5).	51
4.11	Nondimensional heat transfer on the hot bottom surface for a purely isotropically scattering medium enclosed in a square enclosure with black surfaces (Case 6).	53
4.12	Nondimensional temperature along the centerline for a purely isotropically scattering medium enclosed in a square enclosure with black surfaces for $\kappa^* = 0.25$ (Case 6).	54
4.13	Nondimensional temperature along the centerline for a purely isotropically scattering medium enclosed in a square enclosure with black surfaces for $\kappa^* = 1.0$ (Case 6).	55
4.14	Nondimensional temperature along the centerline for a purely isotropically scattering medium enclosed in a square enclosure with black surfaces for $\kappa^* = 10.0$ (Case 6).	56
4.15	Error percentage in the predicted heat transfer at the center of the bottom surface in a purely isotropically scattering medium enclosed in a square enclosure with black surfaces (Case 6).	58
4.16	Comparison of the solution cost of the FVM and Q_L method applied to a square enclosure with a purely isotropically scattering medium (Case 6).	60
4.17	Comparison of the number of cycles required to achieve convergence for the FVM and Q_L method applied to a square enclosure with a purely isotropically scattering medium (Case 6).	61

4.18	Nondimensional heat transfer on the hot bottom surface for a purely isotropically scattering medium with unit optical thickness in rectangular enclosures with black surfaces (Case 7).	64
4.19	Nondimensional temperature along the centerline for a purely isotropically scattering medium with unit optical thickness in rectangular enclosures with black surfaces (Case 7).	65
4.20	Nondimensional heat transfer on the hot bottom surface for an absorbing-isotropically scattering medium enclosed in a square enclosure with black surfaces (Case 8).	68
4.21	Nondimensional heat transfer on the hot bottom surface for an absorbing-anisotropically scattering medium enclosed in a square enclosure with black surfaces (Case 9).	70
4.22	Comparison of the solution cost of the FVM and Q_L method applied to a purely anisotropically scattering medium enclosed in a square enclosure with black surfaces (Case 10).	73
4.23	Comparison of the number of cycles required to achieve convergence for the FVM and Q_L method applied to an purely anisotropically scattering medium enclosed in a square enclosure with black surfaces (Case 10).	74
4.24	Nondimensional heat transfer on the bottom surface of a square enclosure with cold black surfaces enclosing an isothermal absorbing-emitting medium (Case 11).	75
4.25	Control volumes in uniform (a) and non-uniform (b) grids in a square enclosure.	76
5.1	Nondimensional heat transfer on the hot bottom surface for a purely isotropically scattering medium enclosed in a square enclosure with black surfaces.	84
5.2	Nondimensional temperature along the centerline for a purely isotropically scattering medium enclosed in a square enclosure with black surfaces for $\kappa^* = 0.25$	85
5.3	Nondimensional temperature along the centerline for a purely isotropically scattering medium enclosed in a square enclosure with black surfaces for $\kappa^* = 1$	86

5.4	Nondimensional temperature along the centerline for a purely isotropically scattering medium enclosed in a square enclosure with black surfaces for $\kappa^* = 10$	87
5.5	Error percentage in the predicted heat transfer at the center of the bottom surface in a purely isotropically scattering medium enclosed in a square enclosure with black surfaces.	88
5.6	Nondimensional heat transfer on the hot bottom surface for a purely isotropically scattering medium enclosed in a square enclosure with partially reflecting surfaces.	89
5.7	Nondimensional heat transfer on the hot bottom surface for a purely isotropically scattering medium with unit optical thickness in rectangular enclosures with black surfaces.	92
5.8	Nondimensional temperature along the centerline for a purely isotropically scattering medium with unit optical thickness in rectangular enclosures with black surfaces.	93
A.1	The α^l distributions for the first 4 cycles in 3 nodes for $\sigma^s \Delta = 0.3$. . .	110
A.2	Scaled I_a distributions across the enclosure for the first 4 iterations.	114
A.3	Schematic α^l profiles at 3 nodes in the middle of the enclosure . . .	115
B.1	The polar coordinate system (a) and a solid angle (b).	120
B.2	A typical 2D rectangular element.	122
B.3	An interior control volume in a 2D Cartesian grid.	123
B.4	A boundary control volume in a 2D Cartesian grid.	128
C.1	Scaled maximum residual of the P_1 method with Gauss-Seidel without the correction method, Gauss-Seidel with the correction method, and multigrid solvers.	133
C.2	Radiative heat transfer over the solution domain for $\kappa^* = 1$ obtained by the P_1 method with three solvers.	135

List of Tables

4.1	Comparison of the solution cost between the Q_L method and FVM applied to a square enclosure with a purely isotropically scattering medium (Case 6).	62
4.2	Comparison of the solution cost between the Q_L method and FVM applied to a wide enclosure with a purely isotropically scattering medium (Case 7).	66
4.3	Comparison of the solution cost between the Q_L method and FVM applied to a square enclosure with black surfaces containing an absorbing-isotropically scattering medium with $\Omega = 0.5$ (Case 8).	67
4.4	Comparison of the solution cost between the Q_L method and FVM applied to a square enclosure enclosing an anisotropically scattering medium with a linear phase function $\Phi = 1 - \cos(\Psi)$	71
4.5	The solution cost and number of cycles required by the Q_L method applied to a square enclosure with black surfaces enclosing a purely isotropically scattering medium to study the robustness of the Q_L method.	77
5.1	The solution cost and number of cycles required by the UDS and New Scheme applied to an isotropically scattering medium enclosed in a square enclosure with black surfaces.	90
A.1	Number of cycles to achieve convergence in a 2D problem for the multiplicative method.	107
A.2	Number of cycles to achieve convergence in a 1D problem for the multiplicative method with the upwind and exponential schemes.	116
C.1	Performance of three solvers in the P_1 method applied to an emitting-absorbing medium enclosed in a square enclosure.	134

Nomenclature

A_s	surface area [m ²]
AR	aspect ratio of a rectangular enclosure
a	coefficient in the algebraic equations
a_1, a_2	coefficients in the non-linear scattering phase function
b	source term in the algebraic equations
\mathbf{e}_i	unit vector in the i direction
f	forward scattering factor
g	asymmetric factor
I	directional radiant intensity [W / m ² sr]
I_a	average intensity [W / m ²]
I_b	blackbody intensity [W / m ²]
I_s	surface intensity [W / m ² sr]
\mathbf{I}_s	scattering integral [W / m ²]
\mathbf{I}_t	transport integral [W / m ³]
I_P^l	intensity at node P within ω^l [W / m ² sr]
\bar{I}	scattered intensity [W / m ² sr]
ip	integration point
K	absorption coefficient [1 / m]
L	total number of discrete solid angles
L_x, L_y	dimensions of a rectangular enclosure [m]
M	total number of cycles
MN_x, MN_y	size of the coarse-mesh block
N	number of control volumes
N_{ip}	total number of panels in a control volume
N_x, N_y	number of control volumes in the x and y directions
N_θ, N_ϕ	number of discrete angles in the θ and ϕ directions
n_x, n_y	number of elements in the x and y directions
\mathbf{n}	outward unit normal to a control volume surface
Q	radiative heat transfer rate [W]
q	surface heat flux [W / m ²]
q_R	incident radiant heat flux on the surface [W / m ²]
\mathbf{q}	radiant heat flux vector [W / m ²]
q_r'''	radiant source term [W / m ³]

R_P	residual in each cycle
R_{\max}	maximum residual in each cycle
R_{\max}^o	maximum residual at the end of the first cycle
\mathbf{r}	spatial position vector
r_P	residual in each iteration
r_{\max}	maximum residual in each iteration
r_{\max}^o	maximum residual at the end of the first iteration
s	distance along a beam in the \mathbf{s} direction [m]
\mathbf{s}	unit vector in the direction of intensity
\mathbf{s}^l	unit direction vector in the center of discrete solid angle ω^l
T	temperature [K]
T_G	temperature of the medium [K]
T_h, T_c	temperature of the hot and cold surfaces [K]
V	volume [m ³]
x, y, z	Cartesian coordinates [m]

Greek Symbols

α	phase weight
β	control parameter for non-uniform grid
Δ	width of the interior control volumes in a uniform grid [m]
ϵ	surface emissivity
θ	polar angle measured from the z axis
θ_+^l, θ_-^l	boundaries of the solid angle ω^l in the θ direction
κ	extinction coefficient [1/m]
κ^*	optical thickness
ρ	surface reflectivity
σ	Stefan-Boltzmann constant ($= 5.729 \times 10^{-8} \text{ W / m}^2 \text{ K}^4$)
σ^s	scattering coefficient [1/m]
$\kappa\Delta$	cell optical thickness
ϕ	azimuthal angle in the $x - y$ plane measured from the x axis
ϕ_+^l, ϕ_-^l	boundaries of the solid angle ω^l in the ϕ direction
$\Phi(\mathbf{s}', \mathbf{s})$	phase function for scattering from \mathbf{s}' to \mathbf{s}
Ψ	scattering angle between incident (\mathbf{s}') and scattered (\mathbf{s}) directions
Ω	single scattering albedo
ω	solid angle [sr]
ω^+	range of solid angles pointing from the surface to the medium
ω^-	range of solid angles pointing from the medium to the surface

Superscripts

l	in the solid angle ω^l
*	dimensionless

Subscripts

ip	at the integration point
nb	neighbors of node P
P, N, E, \dots	computational nodes
s	related to surface
T, B, R, L	top, bottom, right, and left surfaces
λ	spectral

Acronyms

CMR	Coarse Mesh Rebalance
COMET	Coupled Ordinates METHod
DOM	Discrete Ordinates Method
FVM	Finite Volume Method
GS	Gauss-Seidel solver
REE	Radiation Energy Equation
RTE	Radiative Transfer Equation
UDS	Upwind Differencing Scheme (step scheme)
WU	Work Unit

Chapter 1

Introduction

Thermal radiation refers to a mode of heat transfer caused by electromagnetic waves or photon exchange. Unlike the other two modes of heat transfer, conduction and convection, which depend nearly on the first power of temperature, radiative heat transfer is a very strong function of the absolute temperature level with a power of 4 or 5. Consequently, the importance of radiation becomes more significant as temperature increases. In fact, radiation plays an important role in high-temperature processes, like combustion, and engineering systems, such as boilers, furnaces, reactors, engines, and gas turbines. Even at low temperature, radiation is usually more important than natural convection. Also radiation is of great importance in large-scale systems. For instance, it is not just the high temperature in boilers and furnaces that makes radiation the dominant mode, it is their large size.

The other distinctive feature of thermal radiation is that no medium is required between two locations for heat transfer. This makes radiation the only possibility of heat transfer in space or vacuum, for example to dissipate waste heat from the power systems in space. Because of this broad range of applications, thermal radiation deserves consideration, research and development.

Thermal radiation is a very complex phenomenon and although the governing equations are known, they are difficult to solve. This difficulty originates from the fact that radiation transport depends on radiant intensity which is a function of position, direction, wavelength, and local temperature. In some cases, these dependences are not straightforward. For example the spectral behavior of gases needs very complicated models. In addition, intensities in all directions are usually coupled through a scattering phase function which makes the computational radiation cumbersome. Therefore, while a huge interest exists in predicting radiative heat

transfer because of its applications, these complexities make it very difficult to have a multidimensional robust, accurate, and efficient computational radiation method.

A new computational method for radiative heat transfer in participating media, named the Q_L method, has been introduced in this study. It will be shown that this method is applicable to multidimensional problems and is capable of treating anisotropic scattering and spectral properties.

In this introductory chapter, after a brief explanation of the equations that govern thermal radiation, the existing computational radiation methods and acceleration schemes will be reviewed. At the end of this chapter, the objectives of the present work and the outline of the thesis are given.

1.1 Radiative Transfer Equation

The fundamental variable used to describe radiation is intensity I which is defined as

$$I_\lambda(\mathbf{r}, \mathbf{s}) = \lim_{\Delta A \rightarrow 0} \frac{\Delta Q_\lambda}{\Delta A}$$

where ΔQ_λ represents the spectral directional radiant energy rate which passes an elemental area ΔA , per unit solid angle and per unit wavelength. This element is perpendicular to the ray direction \mathbf{s} and has its center at \mathbf{r} . In general, intensity varies in a finite solid angle $d\omega$, which lies in the direction \mathbf{s} , and the Radiative Transfer Equation (RTE) governs this variation.

Fig.1.1 depicts an elemental volume. The unit vector $\mathbf{s} = s_i \mathbf{e}_i$ (summation implied) is defined by the polar angle θ (measured from the z axis) and azimuthal angle ϕ (measured from the x axis), where \mathbf{e}_i are the unit vectors in the Cartesian coordinates (so $s_1 = \sin \theta \cos \phi$, $s_2 = \sin \theta \sin \phi$, and $s_3 = \cos \theta$). Writing a radiant energy balance for this control volume gives the RTE as [1]

$$\frac{dI_\lambda}{ds} = -K_\lambda I_\lambda - \sigma_\lambda^s I_\lambda + K_\lambda I_{b\lambda} + \sigma_\lambda^s \bar{I}_\lambda \quad (1.1)$$

where K_λ is the absorption coefficient, $I_{b\lambda}$ is the blackbody intensity, and σ_λ^s is the scattering coefficient. In this equation, the left-hand side is the rate of increase of intensity within the solid angle in the control volume. The first two terms in the right-hand side are attenuation through absorption and out-scattering, and the third term is augmentation due to emission. The fourth term, namely the in-scattering term, accounts for the increase of intensity because of diverted photons

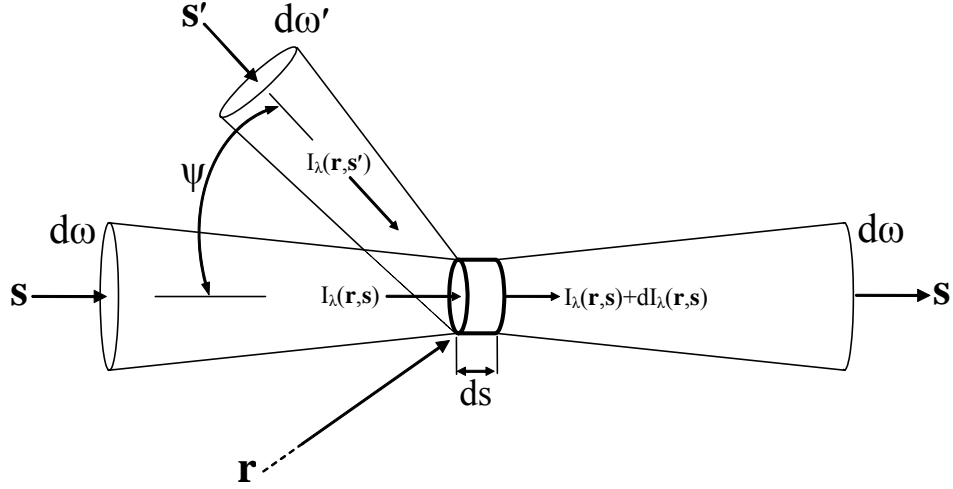


Figure 1.1: The control volume used to derive the RTE.

from the other solid angles into $d\omega$. This term is given by

$$\bar{I}_\lambda(\mathbf{r}, \mathbf{s}) = \frac{1}{4\pi} \int_{4\pi} I_\lambda(\mathbf{r}, \mathbf{s}') \Phi(\mathbf{s}', \mathbf{s}) d\omega' \quad (1.2)$$

where $I_\lambda(\mathbf{r}, \mathbf{s}')$ is the intensity at \mathbf{r} within $d\omega'$ (Fig.1.1) $\Phi(\mathbf{s}', \mathbf{s})$ is the phase function for scattering from the solid angle $d\omega'$ (in the \mathbf{s}' direction) to the solid angle $d\omega$ (in the \mathbf{s} direction). This equation clearly shows that the in-scattering term depends on radiation from all incoming directions.

Eq.(1.1) along with an appropriate boundary condition forms the governing equations of the radiation transport which are solved numerically to find the intensity field.

Radiation contributes to the internal energy equation through a source term, called the radiant source term q_r''' , as [1]

$$\rho c_p \frac{DT}{Dt} = \nabla \cdot (k \nabla T) + q_g''' - q_r''' + \beta T \frac{Dp}{Dt} + \mu \phi \quad (1.3)$$

where

$$q_r''' = \int_0^\infty \iint_{4\pi} K_\lambda (I_{\lambda b} - I_\lambda) d\omega d\lambda \quad (1.4)$$

and q_g''' accounts for the other volumetric energy generations. Eqs.(1.3) and (1.4) relate radiation to the other modes of heat transfer.

1.1.1 Review of Computational Radiation Methods

In spite of the complexities in radiative heat transfer and difficulties in modeling the phenomena, various computational methods have been developed during the last 60 years which were usually adopted from the neutron transport field and modified to fit the radiation heat transfer. Among these methods, there are very accurate but computationally expensive methods like the Monte Carlo method, and there are methods which have traded off the accuracy with the solution cost like the P_1 method.

Reviewing the existing radiation methods is beyond the scope of this study and detailed reviews can be found in Viskanta and Mengüç [2], Modest [3], Lewis and Miller [4], and Siegel and Howell [5]. However, a brief introduction to two of the most common methods, the discrete ordinates method (DOM) and the P_1 method, will be given here to highlight their advantages and disadvantages. Then the widely used finite volume method, which has been employed in this research, will be explained in the next section.

The P_1 Method

This method is a member of the general group of spherical harmonics method (P_N approximation). The general form, the P_N approximation, is obtained by representing the intensity distribution by a series of spherical harmonics. This converts the governing equations to relatively simple partial differential equations with an elliptic nature.

The simplest approximation, the P_1 method, is widely used because of its simplicity and low cost and is implemented in commercial codes like FLUENT and CFX. This method has been discussed in many books and papers for a wide range of applications. A very readable reference for the P_1 method is Modest [3]. Sazhin and coworkers [6] have demonstrated the advantages and limitations of the P_1 method for a real problem, coal combustion in an industrial furnace. In Appendix C of this thesis, the iterative solution of the P_1 method has been briefly discussed.

The major drawback of the P_1 method is that it is only accurate in media with near-isotropic intensity distribution, and the accuracy improves slowly for higher-order methods (like P_3), while the mathematical complexity increases extremely rapidly [3]. Generally, derivation of the spherical harmonics method, even for the P_1 method, is known to be very tedious, although in Chapter 2 of this thesis a very simple derivation will be introduced for the P_1 method. It is a common misconception that the P_1 method gives inaccurate results in optically thin media.

This conclusion is correct in many situations, but is invalid when emission from a hot medium is considered [3].

Another disadvantage of this method is that, because of the orthogonality of the spherical harmonics, the P_1 approximation is unable to treat non-linear scattering phase functions.

The Discrete Ordinates Method

The DOM was originally proposed by Chandrasekhar [7] and was applied to the astrophysical and atmospheric radiation. Carlson and Lathrop [8, 9] extended its application to the neutron transport field and Fiveland [10, 11, 12], and Truelove [13, 14] developed and implemented the method for the radiative heat transfer analysis. This method is available as an option in some commercial codes.

In this method, the directional distribution of the intensity is replaced by a set of discrete directions spanning the total solid angle range of 4π . Integrals over solid angles are approximated by numerical quadrature. Apparently, the accuracy of the method depends strongly on the quadrature scheme. Any of the known methods like the finite volume and the finite element may be used for the spatial discretization.

The DOM suffers from some serious drawbacks like false scattering and ray effect. The false scattering is caused by the spatial discretization error and results in smearing the intensity distribution and can be overcome by using a finer spatial mesh. The ray effect is a result of the angular discretization error and can be reduced by using a finer angular grid or coarser spatial mesh¹ [3]. The other disadvantage of the DOM is difficulties in extending the application of the method beyond Cartesian geometry.

The most serious disadvantage of the DOM is that this method does not ensure the conservation of radiant energy which is a result of using quadrature for the angular discretization. In the next section, the finite volume method will be reviewed which ensures the conservation of energy.

¹It is interesting to know that these two errors, false scattering and ray effect, may partially cancel each other which results in more accurate results (see [36])

1.2 The Finite Volume Radiation Method

Over the last three decades, the finite volume method (FVM) has been accepted as a popular fluid flow solution procedure, mainly because of its exact satisfaction of the conservation equations over the region (the finite volume). Therefore, it was naturally the next step in evolution of the computational radiation methods to apply the finite volume idea to direction as well as space. Replacement of the quadrature in the DOM with the *finite solid angles* in the FVM not only overcomes the problem of energy conservation, but also establishes a method which shares the same philosophy and the same computational grid with the fluid flow solvers.

The finite volume radiation method was first developed by Raithby and Chui [15] and then was extended and applied to various problems: Nonorthogonal meshes [16, 17], cylindrical enclosures [18, 19, 20, 21], pulverized fuel flame [22], unstructured meshes [23, 24, 25, 26, 27], periodic geometries [28], and irregular geometries [29, 30].

Chai *et al.* [31] and Raithby [32] reviewed some features of the method and several researchers [33, 34, 35] compared the DOM and the FVM for some test cases, which showed that the FVM has better accuracy and performance. Raithby [36] did a comprehensive study of the spatial and angular discretization errors. The FVM has been implemented in several commercial codes, such as FLUENT.

In the remainder of this section, the discrete equations for the FVM are derived for a gray medium (wavelength independent). The FVM is applicable to non-gray media but the gray approximation has been used in this study for the sake of simplicity and λ subscript is dropped.

1.2.1 The Discrete Equations

The RTE (Eq.(1.1)) expresses the conservation of radiant energy over an infinitesimal volume in the solid angle which lies in the direction \mathbf{s} (Fig.1.1). Integration of this equation over any specified volume V_P and solid angle ω^l gives a discrete equation which conserves energy in the finite volume and finite solid angle. Carrying out the integrations and using the Gauss divergence theorem, Eq.(1.1) becomes

$$\int_{\omega^l} \int_{A_s} I(\mathbf{s} \cdot \mathbf{n}) dA_s d\omega = \int_{\omega^l} \int_{V_P} [-(K + \sigma^s)I + KI_b + \sigma^s \bar{I}] dV d\omega \quad (1.5)$$

where A_s and V_P are the surface area and volume of the specified control volume and \mathbf{n} is the unit surface normal. K and σ^s are appropriate wavelength-averaged quantities because of the gray-medium approximation.

In the finite volume method, the spatial solution domain is subdivided into discrete nonoverlapping volumes, and a single node is located within each volume where location of this node in the control volume depends on the selected type of the grid (i.e. cell-centered or vertex-centered).

To be consistent with the spatial discretization, direction, which is also an independent variable, is subdivided into L discrete, nonoverlapping solid angles of size ω^l , $l = 1, 2, \dots, L$, which sum to 4π . The number of angles and their size distribution, like the spatial discretization, are chosen by the analyst.

By reasonably approximating all variables as constant over V_P and ω^l , the right-hand side of Eq.(1.5) is approximated as

$$\int_{\omega^l} \int_{V_P} [-(K + \sigma^s)I + KI_b + \sigma^s \bar{I}] dV d\omega \approx [-(K_P + \sigma_P^s)I_P^l + K_P I_{b,P} + \sigma_P^s \bar{I}_P] V_P \omega^l \quad (1.6)$$

where I_P^l is the intensity at node P and within the solid angle ω^l . \bar{I}_P is approximated as [18]

$$\bar{I}_P^l = \frac{1}{4\pi} \sum_{l'=1}^L I_P^{l'} \bar{\Phi}^{l'l} \quad (1.7)$$

where

$$\bar{\Phi}^{l'l} = \frac{\int_{\omega^l} \int_{\omega^{l'}} \Phi(l', l) d\omega' d\omega}{\omega^l}$$

To approximate the left-hand side of Eq.(1.5), the surface of the control volume is subdivided into N_{ip} surface panels of area $A_{s,ip}$ where an integration point is located at the center of each panel. Fig.1.2 shows 2D and 3D control volumes with some of their neighbors where integration points are indicated by “×”.

The radiative heat transfer rate through panel ip and within ω^l is

$$Q_{ip}^l = A_{s,ip} \int_{\omega^l} I_{ip}(\mathbf{s} \cdot \mathbf{n}_{ip}) d\omega \quad (1.8)$$

where the left-hand side of Eq.(1.5) is $\sum_{ip=1}^{N_{ip}} Q_{ip}^l$. Note that I_{ip} and \mathbf{n}_{ip} have been approximated by their values at the integration point ip . Using Eqs.(1.6) and (1.8), the approximation of Eq.(1.5) is

$$\sum_{ip=1}^{N_{ip}} Q_{ip}^l = \sum_{ip=1}^{N_{ip}} A_{s,ip} \int_{\omega^l} I_{ip}(\mathbf{s} \cdot \mathbf{n}_{ip}) d\omega = [-(K_P + \sigma_P^s)I_P^l + K_P I_{b,P} + \sigma_P^s \bar{I}_P] V_P \omega^l \quad (1.9)$$

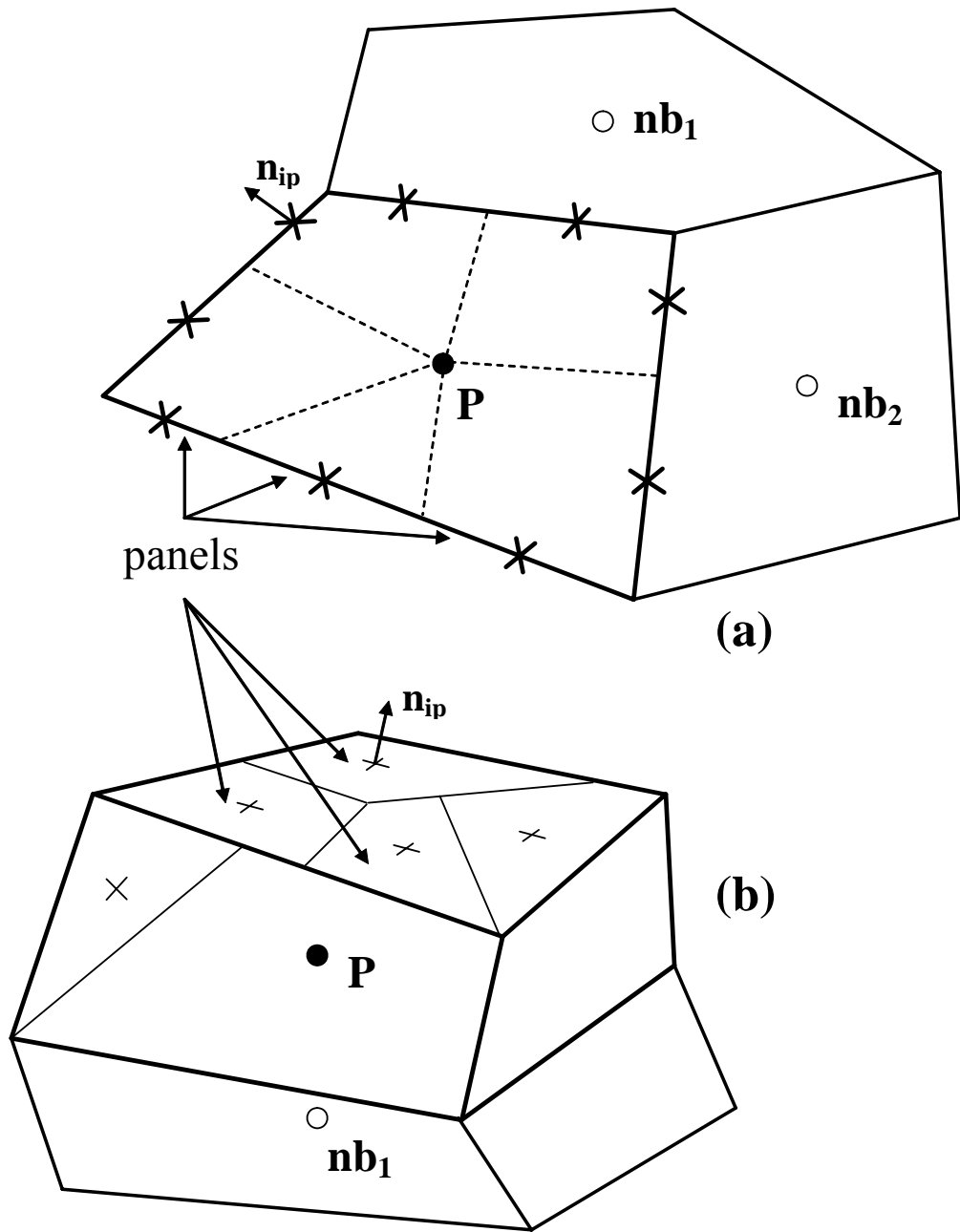


Figure 1.2: A control volume and its panels and integration points (a) 2D (b) 3D.

To complete the discretization, relations should be found between the I_{ip} values and nodal point values like I_P^l and I_{nb}^l , since intensity is only calculated at the computational nodes. Many differencing methods such as the diamond, step, and exponential schemes have been suggested to find I_{ip} . In this study, the simplest method, the step scheme, has been employed which is reviewed in the following section. In Chapter 5 of this thesis, a brief review of the available differencing schemes is presented and a new second-order scheme is proposed.

The Upwind Scheme

The upwind differencing scheme (UDS), also called the step scheme, is a first-order bounded scheme and is widely used in CFD. In this method, the I_{ip} values are approximated by the values at the upstream nodes which is consistent with the physical propagation of the RTE. This approximation means that for example in Fig.1.3, for direction \mathbf{s}_1

$$\begin{aligned} I_1^l = I_2^l = I_8^l = I_9^l &= I_P^l \\ I_3^l = I_4^l &= I_{nb_3}^l \\ I_5^l = I_6^l = I_7^l &= I_{nb_4}^l \end{aligned}$$

and for direction \mathbf{s}_2

$$\begin{aligned} I_3^l = I_4^l = I_5^l = I_6^l = I_7^l &= I_P^l \\ I_1^l = I_2^l &= I_{nb_1}^l \\ I_8^l = I_9^l &= I_{nb_2}^l \end{aligned}$$

The main advantages of the UDS are that this method is very simple and does not produce nonphysical results (e.g. negative intensities) since this scheme is bounded. However, this method is first order and is not accurate in strongly participating media where the intensity changes significantly between the upstream node and the integration point. Also this method produces false scattering.

Relating the I_{ip} values with the nodal values by a differencing scheme (like UDS), Eq.(1.9) becomes a set of discrete equations including only the nodal values which have the form of [15]

$$a_P^l I_P^l = \sum_{nb} a_{nb}^l I_{nb}^l + b_P^l \quad (1.10)$$

The numerical procedure for solving this equation is presented in Chapter 3.

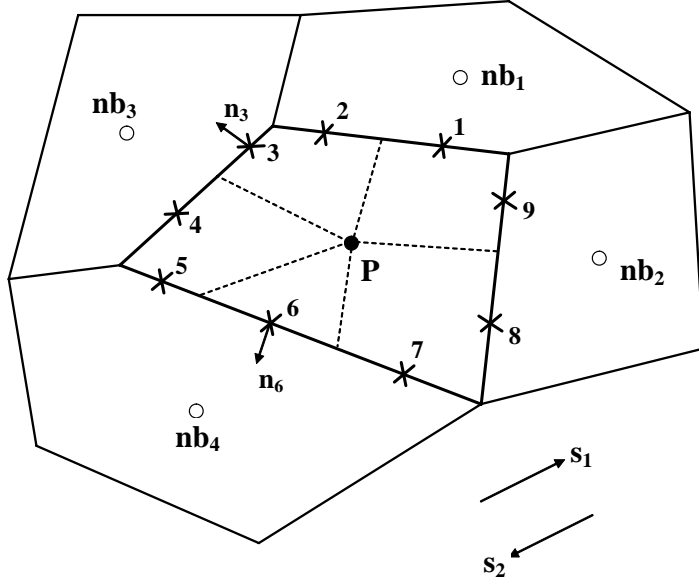


Figure 1.3: A control volume and its integration points to demonstrate the UDS.

Boundary Conditions

These equations still need a boundary condition to form a closed system of equations. For a gray-diffuse surface at temperature T_s , the boundary condition for the surface intensity I_s^l which leaves the surface toward the medium, $\mathbf{s}^l \cdot \mathbf{n} < 0$, is

$$\epsilon_s A_s \sigma T_s^4 + (1 - \epsilon_s) \sum_{\mathbf{s}^l \cdot \mathbf{n} > 0} Q'' = \sum_{\mathbf{s}^l \cdot \mathbf{n} < 0} Q_s^l = A_s \pi I_s^l \quad (1.11)$$

where \mathbf{s}^l is the unit direction vector in the center of the discrete solid angle ω^l , \mathbf{n} is the unit surface normal pointing from the medium towards the surface, ϵ_s is the surface emissivity, and Q^l is the radiative heat transfer rate (Eq.(1.8)). This equation shows that the intensity leaving the surface to the medium I_s^l is a combination of the emitted radiation from the surface (first term) and the reflected radiation from the surface (second term). The reflected radiation, $(1 - \epsilon_s) \sum_{\mathbf{s}^l \cdot \mathbf{n} > 0} Q''$, depends on the incident intensities on the surface. For a black surface, $\epsilon_s = 1$, the boundary condition reduces to

$$I_s^l = \frac{\sigma T_s^4}{\pi}$$

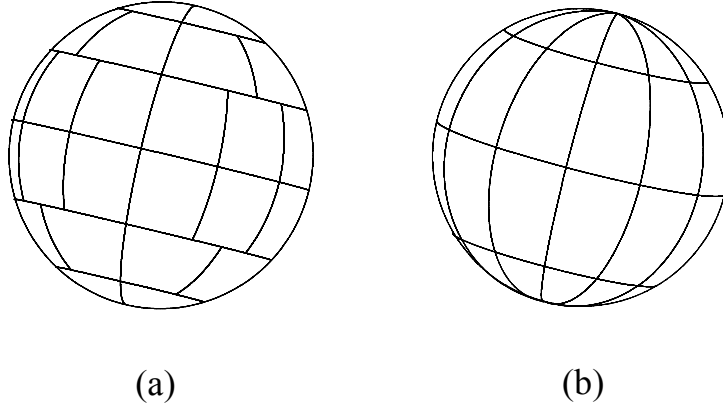


Figure 1.4: Two typical solid angle distributions for $L = 48$.

Angular Grid

Several researchers [23, 28, 32, 37, 38] have discussed the angular discretization error for the FVM especially for the case that the solid angle is bisected by the surface which means that the boundaries of the solid angle are not exactly aligned with the surface. The other issue addressed in these papers is the solid angle distribution over 4π . Fig.1.4 shows two different types of distribution. In (b), the solid angles do not have the same size (especially near the poles they are very small). In (a), they have been made about equal and with the aspect ratio of unity. In this study, only type (b) has been used, although uniform solid angles, type (a), are usually preferred.

1.2.2 Isotropic Scattering

Isotropic scattering is the simplest scattering model which assumes that the energy is scattered uniformly in all directions. In this case, $\Phi = 1$ and Eq.(1.7) becomes

$$\bar{I}_P^l = \frac{1}{4\pi} \sum_{l'=1}^L I_P^{l'} \omega^{l'}$$

where the right-hand side is the discrete form of average intensity I_a :

$$I_a(\mathbf{r}) = \frac{1}{4\pi} \int_{4\pi} I(\mathbf{r}, \mathbf{s}') d\omega'$$

Hence $\bar{I}_P^l = I_{a,P}$ for isotropic scattering.

1.2.3 Radiative Equilibrium

The increase in internal energy due to radiation crossing the boundaries of the control volume is obtained by integrating Eq.(1.5) over $\omega^l = 4\pi$:

$$\int_{4\pi} \int_{A_{s,P}} I(\mathbf{s} \cdot \mathbf{n}) d\omega dA_s = -4\pi \int_{V_P} K(I_a - I_b) dV \approx -4\pi K_P(I_{a,P} - I_{b,P}) V_P \quad (1.12)$$

which equals $q_r''' V_P$ according to Eq.(1.4). The scattering contribution drops out of this energy balance because scattering can change the directional distribution but does not affect the level of radiative energy.

In the radiative equilibrium condition, the temperature field adjusts to make the net surface heat transfer in Eq.(1.12) zero, which means $q_r''' = 0$ and

$$I_{b,P} = I_{a,P}$$

In this condition, the fluid temperature and the radiation fields are disconnected. This very simple condition allows the radiation method to be studied in isolation, without any need to solve the internal energy equation.

1.3 Iterative Solution

In the RTE, emission is a function of the temperature of the medium and in-scattering depends on the intensities from all incoming directions. Therefore, the radiant intensity in a given direction depends on both of the temperature and the complete radiation fields. To avoid solving the equations for all directions simultaneously by a direct solver, these equations are solved iteratively.

To obtain intensity in a given direction, the temperature field and intensities in all the other directions are assumed known from the previous iteration (i.e. they are “lagged”) and appear in the source term in the right-hand side. The newly obtained intensity is used to update the temperature field and the in-scattering terms. This cycle is repeated until convergence is achieved. Such an iterative solution method is referred to as *explicit* or *sequential*.

For optically thin media, the lagged terms are very small and the convergence rate is very fast. As the optical thickness increases, the angular coupling becomes stronger and the lagged terms dominate. At a given node, solving the RTE in each direction conserves the energy in that direction, but updating the temperature field and the in-scattering terms with the newly obtained intensity destroys the

conservation of energy in the previously solved directions. This can dramatically slow down the convergence.

The convergence can become so slow that the explicit method is practically useless. Raithby and Chui [15] observed this slow convergence for the finite volume method and Viskanta and Mengüç [2] reported similar slow convergence for the discrete ordinates method for large optical thicknesses for the explicit solution. In fact, any numerical radiation method that solves the RTE will experience this slow convergence behavior with large optical thicknesses if an explicit procedure is used. Therefore, an acceleration scheme is required to improve the convergence and reduce the solution cost.

1.4 Acceleration Schemes

During the past decades, several methods have been developed to accelerate the neutron transport equation; they are reviewed by Lewis and Miller [4]. Although these methods are also applicable to the RTE, they may not have the same performance since the neutron transport equation and the RTE are not completely identical (i.e. the RTE has a more complex boundary condition).

Raithby and Chui [15] proposed an implicit method to accelerate the finite volume radiation method and later they developed an implicit method based on multiplicative correction (Chui and Raithby [39] and Chui [40]). This method is referred to as the multiplicative acceleration scheme in this research. Fiveland and Jessee [41] studied three acceleration schemes for the RTE including the successive over relaxation, syntax acceleration, and mesh rebalance methods. They showed that the mesh rebalance acceleration scheme for the discrete ordinates method (equivalent to the multiplicative acceleration scheme for the finite volume method) is the most promising method among these available acceleration schemes. However, they also showed that the mesh rebalance method fails to produce convergence of the RTE for large optical thicknesses and fine grids. Raithby and Chui [42] confirmed this poor convergence for the multiplicative method. The breakdown of these acceleration methods makes them practically ineffective since fine meshes are required to obtain accurate solutions.

To overcome this problem, Fiveland and Jessee [41] suggested the coarse mesh rebalance (CMR) method. This method is identical to the basic mesh rebalance method except that a coarser mesh is used for the rebalance equation (the implicit equation) than for the RTE. In the CMR method, the rebalance mesh is obtained by regrouping the control volumes of the basic mesh into blocks (to form the coarse

grid) in a way that each block has a cell optical thickness around unity. The cell optical thickness is defined as the product of a characteristic length of the grid (e.g. spacing between nodes) and the extinction coefficient. They showed that the CMR method dramatically improves the convergence of the RTE for several simple benchmark problems on uniform grids. However, a general regrouping method has not been proposed and extending the method to complex geometries and unstructured grids is questionable. Studies in the neutron transport community have shown that the stability of CMR is conditional and the convergence becomes slower or unstable for certain conditions [43, 44, 45].

As another remedy, Raithby and Chui [42] showed that the poor convergence of the multiplicative method can be also improved by introducing underrelaxation to damp the interaction between the RTE and the implicit equations of the multiplicative method. However, these authors did not claim a recipe for obtaining the underrelaxation factors and these factors are problem and grid dependent. In Appendix A, the multiplicative method will be scrutinized to understand the reason for its breakdown.

Also recently Mathur and Murthy [46, 47] have developed a new method, named the coupled ordinates method (COMET), based on the multigrid idea, which solves the internal energy equation and the RTE together. In this method, at a given node, the intensities in all directions and the temperature are updated together. To reduce the computational cost, for the interior nodes, the average intensity is also included which results in a matrix that can be easily upper triangularized. This method has been shown to reduce the cost substantially. However, later studies implied that the complexity of this method increases sharply as the scattering phase function becomes more complicated (Mathur and Murthy [47]).

This review shows that a general and efficient computational method for thermal radiation is still required.

1.5 Objectives of this Study

The objectives of this work are summarized as

1. to develop and formulate a new efficient, robust and accurate computational radiation method, and
2. to evaluate the new method by applying it to several 1D and 2D benchmark problems.

1.6 Main Approximations

Some approximations are required to make the problems simple and to allow the results to be compared with the exact solutions. These simplifications do not suggest that these effects (e.g. gray medium or diffuse surface) are unimportant or uninteresting in engineering applications. Also these approximations do not mean that the new method is incapable of handling them. The main approximations in this work are:

1. The medium is assumed to be gray which neglects the spectral effects. All radiative properties, like the absorption and scattering coefficients, are approximated to be uniform, constant and known.
2. All surfaces are assumed isothermal, gray, and diffuse with constant and known emissivity and reflectivity.
3. The radiative equilibrium condition is assumed so that radiation can be studied in isolation.

1.7 Outline of the Thesis

Chapter 2 of this thesis describes the basis of the Q_L method and presents the formulation of this new method. To explore its performance, the Q_L method is applied to several 1D and 2D benchmark problems where Chapter 3 explains the numerical procedure, grid, and iterative solver used to solve these problems. In Chapter 4, results of these test cases are presented, and the accuracy, efficiency and robustness of the Q_L method is studied.

In Chapter 5, a new differencing method based on the Q_L idea is formulated and results for several 2D test cases are presented. Chapter 6 contains summary, conclusions and suggestions for future work. In Appendix A, the multiplicative acceleration scheme has been studied to demonstrate its performance and understand the reason of its breakdown. Appendix B presents the complete discretization of the Q_L equations for a 2D Cartesian grid as a supplement to Chapter 2. Appendix C studies two solvers to accelerate the convergence rate of the P_1 method.

Chapter 2

The Q_L Method

It was concluded in the first chapter that an accurate, efficient, and robust computational method capable of resolving the complexities in thermal radiation is still required. In this chapter, fundamentals of a newly proposed computational method, named the Q_L method, are presented¹. The method has been formulated for the general case and the solution procedure is described. At the end of this chapter, the expected accuracy and efficiency of this method are discussed.

2.1 Mathematical Formulation

Methods like the FVM and DOM solve the RTE to conserve the radiant energy in each discrete direction for each control volume. In contrast, a method like the P_1 has been formulated to conserve the radiant energy in all directions in each control volume. While the former are accurate but costly, the latter is inaccurate but inexpensive. The idea of the Q_L method is to conserve radiant energy in a control volume in all directions but include the directional effects in the solution by using the phase weight concept.

2.1.1 The Radiation Energy Equation

The RTE was introduced in Chapter 1 as

$$\frac{dI}{ds} = -(K + \sigma^s)I(\mathbf{r}, \mathbf{s}) + KI_b(\mathbf{r}) + \frac{\sigma^s}{4\pi} \int_{4\pi} I(\mathbf{r}, \mathbf{s}')\Phi(\mathbf{s}', \mathbf{s})d\omega' \quad (2.1)$$

¹This method is originally proposed and formulated by G. D. Raithby in 1996 but was never tested or published. The name of the method was also suggested by him.

Integrating Eq.(2.1) over the volume V_P and over a solid angle of 4π results in the Radiation Energy Equation (REE). Recognizing that $dI/ds = \nabla I \cdot \mathbf{s} = \nabla \cdot (I\mathbf{s})$, integrating the left-hand side of Eq.(2.1) and using the Gauss divergence theorem gives

$$\int_{4\pi} \int_{V_P} \frac{dI}{ds} dV d\omega = \int_{4\pi} \int_{V_P} \nabla \cdot (I\mathbf{s}) dV d\omega = \int_{A_{s,P}} \left[\int_{4\pi} I \mathbf{s} d\omega \right] \cdot \mathbf{n} dA_s \quad (2.2)$$

The local *radiant heat flux* vector is, by the definition of intensity,

$$\mathbf{q}(\mathbf{r}) = \int_{4\pi} I(\mathbf{r}, \mathbf{s}) \mathbf{s} d\omega \quad (2.3)$$

Substituting this into Eq.(2.2) yields

$$\int_{4\pi} \int_{V_P} \frac{dI}{ds} dV d\omega = \int_{A_{s,P}} \mathbf{q} \cdot \mathbf{n} dA_s$$

which is the radiative heat flow leaving through the surface $A_{s,P}$.

In the integration of the right-hand side of Eq.(2.1), the integrals of the out-scattering and in-scattering terms cancel exactly (as they must because scattering only redistributes the energy over directions but does not change the energy level). Using the definition of average intensity, $\int_{4\pi} I d\omega = 4\pi I_a$, the REE is

$$\int_{A_{s,P}} \mathbf{q} \cdot \mathbf{n} dA_s = -4\pi \int_{V_P} K (I_a - I_b) dV \quad (2.4)$$

This equation was derived before (Eq.(1.12)) by integrating Eq.(1.5) over $\omega^l = 4\pi$. The only difference in the procedures is that here the local radiant heat flux vector \mathbf{q} has been used in the left-hand side.

2.1.2 The Equation for $\mathbf{q}(\mathbf{r})$

The directional intensity I is required in Eq.(2.3) to obtain $\mathbf{q}(\mathbf{r})$ for Eq.(2.4). This directional intensity is obtained here by re-arranging the RTE as follows:

$$I(\mathbf{r}, \mathbf{s}) = \frac{-1}{\kappa} \frac{dI}{ds} + (1 - \Omega) I_b(\mathbf{r}) + \Omega \left\{ \frac{1}{4\pi} \int_{4\pi} I(\mathbf{r}, \mathbf{s}') \Phi(\mathbf{s}', \mathbf{s}) d\omega' \right\} \quad (2.5)$$

where $\kappa = K + \sigma^s$ is the *extinction coefficient* and $\Omega = \sigma^s / \kappa$ is the *single scattering albedo*. It is important to mention that using the RTE in this way becomes inappropriate in the limit of vanishing medium participation (for example, $(dI/ds)/\kappa$ becomes indeterminate since $dI/ds \rightarrow 0$ as $\kappa \rightarrow 0$).

Substituting this equation for I into Eq.(2.3), the integral of the I_b term vanishes since $\int_{4\pi} \mathbf{s} d\omega = 0$. Using $dI/ds = \nabla I \cdot \mathbf{s} = \frac{\partial I}{\partial x_j} s_j$ in Eq.(2.5), and $\mathbf{s} = s_i \mathbf{e}_i$ in Eq.(2.3), the equation for $\mathbf{q}(\mathbf{r})$ becomes

$$\mathbf{q}(\mathbf{r}) = -\frac{1}{\kappa} \mathbf{I}_t + \Omega \mathbf{I}_s \quad (2.6)$$

where \mathbf{I}_t , the transport integral, and \mathbf{I}_s , the scattering integral, are defined as

$$\mathbf{I}_t = \left\{ \int_{4\pi} \frac{\partial I}{\partial x_j} s_j s_i d\omega \right\} \mathbf{e}_i \quad (2.7)$$

$$\mathbf{I}_s = \left\{ \int_{4\pi} \left\{ \frac{1}{4\pi} \int_{4\pi} I(\mathbf{r}, \mathbf{s}') \Phi(\mathbf{s}', \mathbf{s}) d\omega' \right\} s_i d\omega \right\} \mathbf{e}_i \quad (2.8)$$

In the following section, these integrals are evaluated for the general case and for several special cases like uniform intensity and isotropic scattering.

Evaluation of the Transport Integral, \mathbf{I}_t

Uniform Intensity Distribution For uniform distribution, $I = I_a$, the \mathbf{I}_t integral in Eq.(2.7) becomes

$$\mathbf{I}_t = \left\{ \int_{4\pi} \frac{\partial I_a}{\partial x_j} s_j s_i d\omega \right\} \mathbf{e}_i = \frac{\partial I_a}{\partial x_j} \left\{ \int_{4\pi} s_j s_i d\omega \right\} \mathbf{e}_i = \frac{4\pi}{3} \nabla I_a \quad (2.9)$$

since

$$\begin{aligned} \int_{4\pi} s_i s_j d\omega &= \frac{4\pi}{3} && \text{for } i = j \\ &= 0 && \text{for } i \neq j \end{aligned} \quad (2.10)$$

General Equation for \mathbf{I}_t The phase weight α^l is defined as

$$\alpha^l = \frac{I^l}{I_a} \quad (2.11)$$

which gives the relative intensity for each ω^l . Re-arranging this equation gives $I^l = \alpha^l I_a$. If it is assumed that the values of α^l are known, the general equation for

\mathbf{I}_t is

$$\begin{aligned}
\mathbf{I}_t &= \left\{ \int_{4\pi} \frac{\partial I}{\partial x_j} s_j s_i d\omega \right\} \mathbf{e}_i = \frac{\partial}{\partial x_j} \left\{ \int_{4\pi} I s_i s_j d\omega \right\} \mathbf{e}_i \\
&= \frac{\partial}{\partial x_j} \left\{ I_a \sum_{l=1}^L \alpha^l \left[\int_{\omega^l} s_i s_j d\omega \right] \right\} \mathbf{e}_i \\
&= \frac{\partial}{\partial x_j} \left\{ I_a \sum_{l=1}^L \alpha^l D_{ij}^l \right\} \mathbf{e}_i
\end{aligned} \tag{2.12}$$

\mathbf{D}^l has 9 components² for each direction l ($D_{ij}^l = \int_{\omega^l} s_i s_j d\omega$), but is independent of spatial location. Values of D_{ij}^l are calculated by exact integration, or precise numerical integration, and stored. $\sum_L D_{ij}^l = \int_{4\pi} s_i s_j d\omega$ should agree with the results of exact integration in Eq.(2.10). Appendix B presents the D_{ij}^l components with exact integration.

Evaluation of the Scattering Integral, \mathbf{I}_s

Isotropic Scattering For $\Phi = 1$, the scattering integral is

$$\mathbf{I}_s = \int_{4\pi} \left\{ \frac{1}{4\pi} \int_{4\pi} I(\mathbf{r}, \mathbf{s}') d\omega' \right\} \mathbf{s} d\omega = I_a(\mathbf{r}) \int_{4\pi} \mathbf{s} d\omega = 0 \tag{2.13}$$

This means that for isotropic scattering, scattering makes no contribution to the net radiant flux through the control volume faces.

Linear Anisotropic Scattering $\Phi(\mathbf{s}', \mathbf{s}) = 1 + a_1(\mathbf{s} \cdot \mathbf{s}')$: The uniform part of the $\Phi(\mathbf{s}', \mathbf{s})$ does not contribute to the scattering integral, so that

$$\begin{aligned}
\mathbf{I}_s &= \frac{a_1}{4\pi} \int_{4\pi} \left\{ \int_{4\pi} I(\mathbf{r}, \mathbf{s}') \mathbf{s} \cdot \mathbf{s}' d\omega' \right\} \mathbf{s} d\omega \\
&= \frac{a_1}{4\pi} \left\{ \int_{4\pi} I(\mathbf{r}, \mathbf{s}') \left[\int_{4\pi} s_i s_j d\omega \right] s'_j d\omega' \right\} \mathbf{e}_i
\end{aligned} \tag{2.14}$$

Using Eq.(2.10) gives

$$\mathbf{I}_s = \frac{a_1}{3} \int_{4\pi} I(\mathbf{r}, \mathbf{s}') \mathbf{s}' d\omega' = \frac{a_1}{3} \mathbf{q}(\mathbf{r}) \tag{2.15}$$

²Only 6 of these components are independent since $D_{ij}^l = D_{ji}^l$.

General Equation for \mathbf{I}_s Introducing the phase weight from Eq.(2.11), the \mathbf{I}_s integral in Eq.(2.8) for any $\Phi(\mathbf{s}', \mathbf{s})$ can be written as

$$\begin{aligned}
\mathbf{I}_s &= \int_{4\pi} \left\{ \frac{1}{4\pi} \int_{4\pi} I(\mathbf{r}, \mathbf{s}') \Phi(\mathbf{s}', \mathbf{s}) d\omega' \right\} \mathbf{s} d\omega \\
&= I_a(\mathbf{r}) \sum_{l'=1}^L \alpha^{l'} \left\{ \int_{\omega^{l'}} \left\{ \frac{1}{4\pi} \int_{4\pi} \Phi(\mathbf{s}', \mathbf{s}) \mathbf{s} d\omega \right\} d\omega' \right\} \\
&= I_a(\mathbf{r}) \sum_{l'=1}^L \alpha^{l'} \mathbf{F}^{l'} \tag{2.16}
\end{aligned}$$

where the vector $\mathbf{F}^{l'}$ has 3 components $F_i^{l'}$ for every solid angle $\omega^{l'}$. The values of $F_i^{l'}$ are calculated by exact integration, or precise numerical integration, and stored (Appendix B).

2.1.3 Approximate Equations for $\mathbf{q}(\mathbf{r})$ in the Interior

Knowing \mathbf{I}_t and \mathbf{I}_s for the general and special cases, \mathbf{q} is evaluated from Eq.(2.6).

Approximately Uniform I

If the intensity is exactly uniform, the heat flow, by Eq.(2.3) is exactly zero. However, if $I(\mathbf{r}, \mathbf{s})$ is approximately uniform, substituting Eq.(2.13) for isotropic scattering and Eq.(2.9) for uniform distribution into Eq.(2.6) yields the following equation for the radiant heat flux:

$$\mathbf{q}(\mathbf{r}) = -\frac{4\pi}{3\kappa} \nabla I_a \tag{2.17}$$

For linear anisotropic scattering, and nearly uniform I , substituting Eqs.(2.15) and (2.9) into Eq.(2.6) leads to

$$\mathbf{q}(\mathbf{r}) = \frac{-4\pi}{3(\kappa - a_1\sigma^s/3)} \nabla I_a \tag{2.18}$$

Eqs.(2.17) and (2.18) agree with the P_1 approximation [3], but the derivation here is both simpler and independent of the spherical harmonics.

General Case

Substituting the General Equation for \mathbf{I}_t , Eq.(2.12), and \mathbf{I}_s , Eq.(2.16), the equation of \mathbf{q} , Eq.(2.6), yields

$$\mathbf{q}(\mathbf{r}) = \left[-\frac{1}{\kappa} \frac{\partial}{\partial x_j} \left(I_a \sum_{l=1}^L \alpha^l D_{ij}^l \right) + \Omega \left(I_a \sum_{l'=1}^L \alpha^{l'} F_i^{l'} \right) \right] \mathbf{e}_i \quad (2.19)$$

where defining

$$T_{ij} = \sum_{l=1}^L \alpha^l D_{ij}^l \quad (2.20)$$

and

$$S_i = \sum_{l'=1}^L \alpha^{l'} F_i^{l'} \quad (2.21)$$

simplifies Eq.(2.19) to

$$\mathbf{q}(\mathbf{r}) = \left[-\frac{1}{\kappa} \frac{\partial}{\partial x_j} (I_a T_{ij}) + \Omega (I_a S_i) \right] \mathbf{e}_i \quad (2.22)$$

For the special case of linear anisotropic scattering, using Eq.(2.15) for \mathbf{I}_s reduces the final equation into

$$\mathbf{q}(\mathbf{r}) = \left[\frac{-1}{(\kappa - a_1 \sigma^s / 3)} \frac{\partial}{\partial x_j} (I_a T_{ij}) \right] \mathbf{e}_i \quad (2.23)$$

2.1.4 Equation for \mathbf{q}_{ip} at Boundary Integration Points

For integration points that lie on the boundary of a gray-diffuse surface,

$$\begin{aligned} \mathbf{q}_{ip} \cdot \mathbf{n}_{ip} &= q_{ip} = \underbrace{\int_{\omega^-} I \mathbf{s} \cdot \mathbf{n}_{ip} d\omega}_{\text{flux out of the medium}} + \epsilon_s \frac{\sigma T_s^4}{\pi} \underbrace{\int_{\omega^+} \mathbf{s} \cdot \mathbf{n}_{ip} d\omega - \rho_s \int_{\omega^-} I \mathbf{s} \cdot \mathbf{n}_{ip} d\omega}_{\text{flux towards the medium}} \\ &= (1 - \rho_s) \int_{\omega^-} I \mathbf{s} \cdot \mathbf{n}_{ip} d\omega - \epsilon_s \sigma T_s^4 \end{aligned} \quad (2.24)$$

where ω^+ is the range of solid angles carrying radiation into the medium from the surface, and ω^- is the range carrying radiation out of the medium towards the surface. ρ_s is the surface reflectivity which is related to the surface emissivity by $\rho_s = 1 - \epsilon_s$. Notice that $\int_{\omega^+=2\pi} \mathbf{s} \cdot \mathbf{n}_{ip} d\omega = -\pi$.

2.2 The Discrete Equation

Eqs.(2.22) and (2.24) give the radiant heat flux required by the REE (Eq.(2.4)). Using the finite volume method, the REE is discretized to form a set of linear algebraic equations for the nodal I_a values.

Using the same approximations as Chapter 1, for a specified control volume (Fig.1.2), the discrete form of the REE is

$$\sum_{ip} \mathbf{q}_{ip} \cdot \mathbf{n}_{ip} A_{s,ip} = -4\pi K_P V_P (I_{a,P} - I_{b,P}) \quad (2.25)$$

where \mathbf{q}_{ip} is the radiant heat flux evaluated at an integration point ip , \mathbf{n}_{ip} is the unit normal to the panel at the integration point, $A_{s,ip}$ is the surface area of the panel, K_P is the absorption coefficient at node P , V_P is the volume of the control volume and $I_{a,P}$ and $I_{b,P}$ are the average intensity and blackbody intensity at node P , respectively.

At the interior integration points ($ip = 1, 2, \dots, 7$ in Fig.2.1), \mathbf{q}_{ip} is calculated from Eq.(2.22) using a linear profile approximation based on the nodal I_a values (see Appendix B for details).

For the boundary integration points ($ip = 8$ and 9 in Fig.2.1), Eq.(2.24) is used to find the \mathbf{q}_{ip} values in Eq.(2.25). In the discrete form, Eq.(2.24) becomes

$$q_{ip} = \epsilon_s I_{a,p} \sum_{\mathbf{N}^l \cdot \mathbf{n}_{ip} > 0} \alpha_P^l \mathbf{N}^l \cdot \mathbf{n}_{ip} - \epsilon_s \sigma T_s^4 \quad (2.26)$$

where \mathbf{N}^l is a vector with 3 components ($N_i^l = \int_{\omega^l} s_i d\omega$) and is calculated and stored for every l . Calculating N_i^l and q_{ip} is explained in Appendix B.

Substituting the \mathbf{q}_{ip} equations at the interior and boundary integration points into Eq.(2.25) results in a linear algebraic equation, called the Q_L equation, for I_a at each node P with the form of

$$a_P I_{a,P} = \sum_{nb} a_{nb} I_{a,nb} + b_P \quad (2.27)$$

where the coefficients and the source term depend, for the general case, on the α^l . The source term also depends on the local temperature through the I_b term. The complete discretization of the equations for a 2D Cartesian grid is presented in Appendix B.

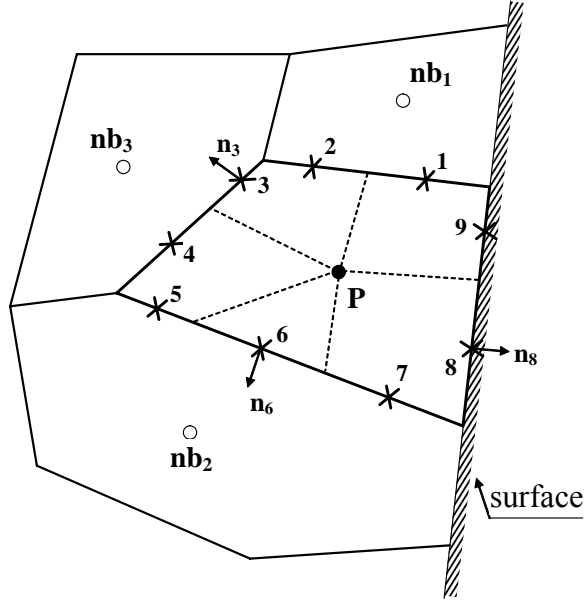


Figure 2.1: A 2D boundary control volume and its interior and boundary integration points.

2.3 Solution Procedure

Eq.(2.27) is the final form of the discretized equations for the Q_L method which are solved to find the I_a field. Both of the coefficients and the source term in that equation depend on the α^l distribution through T_{ij} and S_i . In the general case, the α^l distribution is not known and consequently, the Q_L method should be accompanied by one of the methods which solve the RTE to find the directional intensities. In this research, the FVM method with UDS has been adopted to obtain the directional intensity distribution. The main reason of using the UDS is its boundedness and simplicity.

The I_a field is calculated by the Q_L method and is inserted in the FVM to find the directional intensity distribution. Knowing the directional intensities, the α^l distribution is calculated as

$$\alpha^l = \frac{I^l}{\frac{1}{4\pi} \sum_{l=1}^L I^l \omega^l} \quad (2.28)$$

which is then used in the Q_L method.

For the general case where the radiation and temperature fields are linked through the q_r''' and I_b terms, the Q_L equations and other governing equations

(like the momentum and internal energy equations) should be solved together. In this case, the Q_L method solution procedure requires the following steps assuming that the radiation and internal energy equations are solved segregated:

1. N_i^l , D_{ij}^l , and F_i^l ($i, j = 1, 2, 3$) are calculated and stored.
2. Uniform intensity distribution is used as the initial guess which means $\alpha^l = 1$ for all nodes and all directions. q_r''' is guessed (e.g. $q_r''' = 0$).
3. Knowing α^l , T_{ij} (Eq.(2.20)) and S_i (Eq.(2.21)) are calculated.
4. Since q_r''' is known, all the other governing equations are solved to find the temperature field.
5. The coefficients and the source term in Eq.(2.27) are updated by information obtained in Steps 3 and 4.
6. Eq.(2.27) is solved by an iterative solver like multigrid and residuals are reduced below the specified target to obtain I_a in all nodes.
7. The radiant source term q_r''' is updated.
8. After each specific number of cycles³ (e.g. 5 or 10), these parts are also accomplished:
 - Knowing the temperature and I_a fields, the I_b and \bar{I} terms⁴ in the discrete RTE (Eq.(1.10)) are updated.
 - The FVM is used to solve the RTE and find the directional intensities and the α^l distribution (Eq.(2.28)).
9. Steps 3 to 9 (one cycle) are repeated until the convergence to the fluid flow and heat transfer problem is achieved.

It is important to mention that Step 4 may be very complicated *per se* and usually includes solving the continuity, momentum, internal energy, turbulence model, particulate transport, and chemical reaction equations.

³One cycle is defined as Steps 3 to 9 of this solution procedure.

⁴In fact, the Q_L method calculates the I_a field and another expression is required to relate \bar{I} to I_a (for this expression, see Appendix B).

Step 8 is accomplished occasionally after each specific number of cycles. This specified number is at discretion of the analyst and depends on the problem and required accuracy.

Also it should be pointed out that the Q_L method can be used when the radiation and the fluid flow and heat transfer equations are solved coupled. In the coupled solution, Steps 4, 5, 6, and 7 in the above procedure are replaced by solving a system of equations including continuity, momentum, internal energy, ... and the Q_L equations for u, v, w, p, T, \dots and I_a .

If the temperature field and radiation are disconnected (e.g. radiative equilibrium), the solution procedure reduces to:

1. Steps 1 and 2 as before.
2. Based on the initial guess, T_{ij} and S_i are calculated and then the coefficients and the source term in Eq.(2.27) are computed.
3. Eq.(2.27) is solved and residuals are reduced below the specified target to obtain I_a in all nodes.
4. Knowing the I_a distribution, the I_b and \bar{I} terms in the discrete RTE are updated.
5. The FVM is used to solve the RTE and find the directional intensities and the α^l distribution (Eq.(2.28)).
6. T_{ij} and S_i are updated and then the coefficients and the source term in Eq.(2.27) are calculated.
7. Steps 3 to 7 (one cycle) are repeated until a preset convergence criterion is satisfied.

This solution procedure is shown by a flowchart in Chapter 3 (Fig.3.5) after the convergence criteria for Step 3 and Step 7 (for the cycle) are defined.

2.4 Accuracy and Efficiency

2.4.1 Accuracy

There are two issues concerning the accuracy of the Q_L method that should be considered separately: the modeling error and the discretization error.

Using the phase weights in evaluating \mathbf{q} for the REE includes the effect of the directional intensity distribution in the REE. This gives the Q_L method a great advantage to solve for I_a while including the directional effects. Therefore, the Q_L method is expected to be accurate even when the intensity distribution is not isotropic.

The linear profile approximation which is used to discretize the REE is a second-order discretization scheme; however, the accuracy of the imported α^l distribution can affect the accuracy. When the UDS, which is a first-order scheme, is used in the FVM, the Q_L method is also expected to be first-order, although the discretization in this method is second-order.

In summary, since the error is only due to discretization, the Q_L method converges to the exact solution of the RTE as the spatial and angular grids are refined.

2.4.2 Computational Cost

As stated before, the conventional FVM or DOM (without acceleration) have slow convergence rates for the strongly participating media since the radiant energy in each control volume is not conserved during the iterative solution. The Q_L method formulation gives an equation which has been integrated over all solid angles and consequently conserves the radiant energy in each control volume. This has been observed to lead to a rapid convergence.

The other advantage of the Q_L method is that when this method is used to compute radiation in a fluid flow and heat transfer problem, only one equation is required for each control volume (for I_a). For example, for N control volumes, there are N equations. But when the FVM with L solid angles is used, $N \times L$ equations for intensity must be formed in each cycle where under several conditions (e.g. strongly participating medium), many cycles are required to obtain the convergence .

An example demonstrates the significant difference between these two approaches for a fluid flow and heat transfer problem. For a problem of modest size, the intensity may be calculated at $N = 10^5$ spatial nodes. In the FVM with $L = 48$ directions, this requires that $N \times L = 4.8$ million equations for intensity be formed and solved. For strong medium participation, the number of cycles M can often exceed 10. Therefore, for this modest problem, the formation and solution of $N \times L \times M = 48$ million equations are required. This enormous computational effort may be repeated every time step until convergence to the fluid flow and heat transfer problem is achieved. In the Q_L method, only N equations are required and

M is usually smaller because of the better convergence rate. In this method, solving the $N \times L$ equations for directional intensities is required only once in several number of cycles.

2.5 Concluding Remarks

The Q_L method was introduced and formulated in this chapter. The main idea of this method is using the phase weight concept to relate the directional and average intensities, and re-arranging the RTE to find a new expression for the radiant heat flux. This derivation procedure gives an equation for I_a which also includes the directional effects through the phase weights. The spectral and non-uniform radiative properties can be easily incorporated and the method can be implemented in the non-orthogonal and unstructured grids.

The resulting equations, which are elliptic, can be discretized by a linear profile approximation which results in a set of linear algebraic equations for I_a . Then this set of equations can be solved by the efficient linear equations solvers like multigrid.

Also the strategy to include the Q_L method in solving a fluid flow and heat transfer problem was described in this chapter and it was discussed that this method can substantially reduce the computational cost for thermal radiation by reducing both the number of cycles and the cost of each cycle.

To verify the accuracy and robustness, and to measure the efficiency of the Q_L method, several benchmark problems have been solved. The numerical procedure, description of the problems and results are presented in the next two chapters.

Chapter 3

The Numerical Solution

The Q_L method was described and the equations were derived in Chapter 2. To study the performance of this new method, several benchmark problems have been solved and their results are presented in Chapter 4. In this chapter, the geometry of these problems, and the computational grid, convergence criteria and solver used are explained.

3.1 Geometry

The geometry of all of the benchmark problems solved in this research is a 2D rectangular enclosure with isothermal, diffuse, gray surfaces enclosing a gray medium at temperature T_G , with known and constant absorption coefficient K , and scattering coefficient σ^s . Also the temperature and emissivities of all of the four surfaces are specified.

Fig.3.1 shows the rectangular enclosure, its dimensions, and the origin which is located at the bottom-left corner of the enclosure. In this enclosure, the aspect ratio AR is defined as

$$AR = \frac{L_y}{L_x}$$

3.2 Computational Grid

The grid generation starts by dividing the solution domain to a specified number of rectangular elements. As shown in Fig.3.2 (a), the computational nodes are

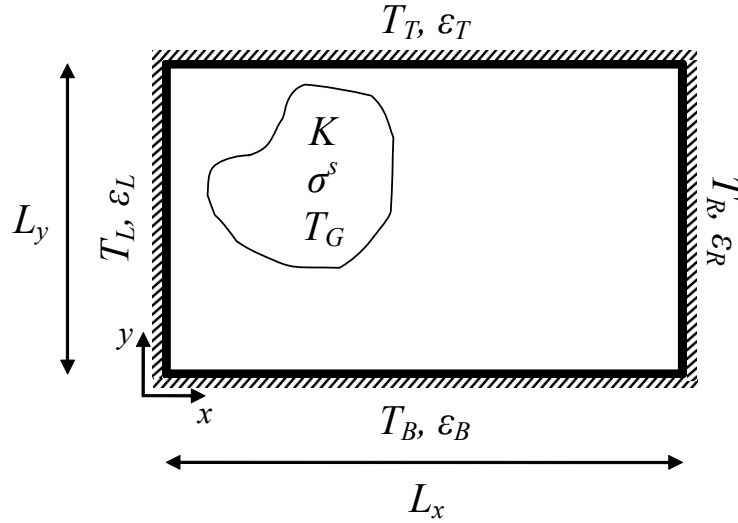


Figure 3.1: The geometry: a 2D rectangular enclosure.

located at the corners of these elements and four panels are created inside each element where an integration point is located at the center of each panel.

In the interior, each four neighbor elements create a control volume around their shared corner. Such a grid is called vertex-centered. Fig.3.2 (b) shows 4 neighbor elements and a control volume in this kind of grid.

In a 2D rectangular enclosure, for a specified number of elements in the x and y directions (n_x and n_y), a uniform grid is generated by dividing the enclosure into $n_x \times n_y$ equal rectangular elements with the size of $\Delta x \times \Delta y \times 1$ where

$$\Delta x = \frac{L_x}{n_x}$$

$$\Delta y = \frac{L_y}{n_y}$$

This results in $N_x \times N_y = (n_x + 1) \times (n_y + 1)$ control volumes and nodes where the interior control volumes have the same size ($\Delta x \times \Delta y \times 1$) and the boundary control volumes are a half or a quarter of the interior ones. Fig.3.3 depicts a 4×5 grid for a rectangular enclosure where the control volumes are defined by the dashed lines.

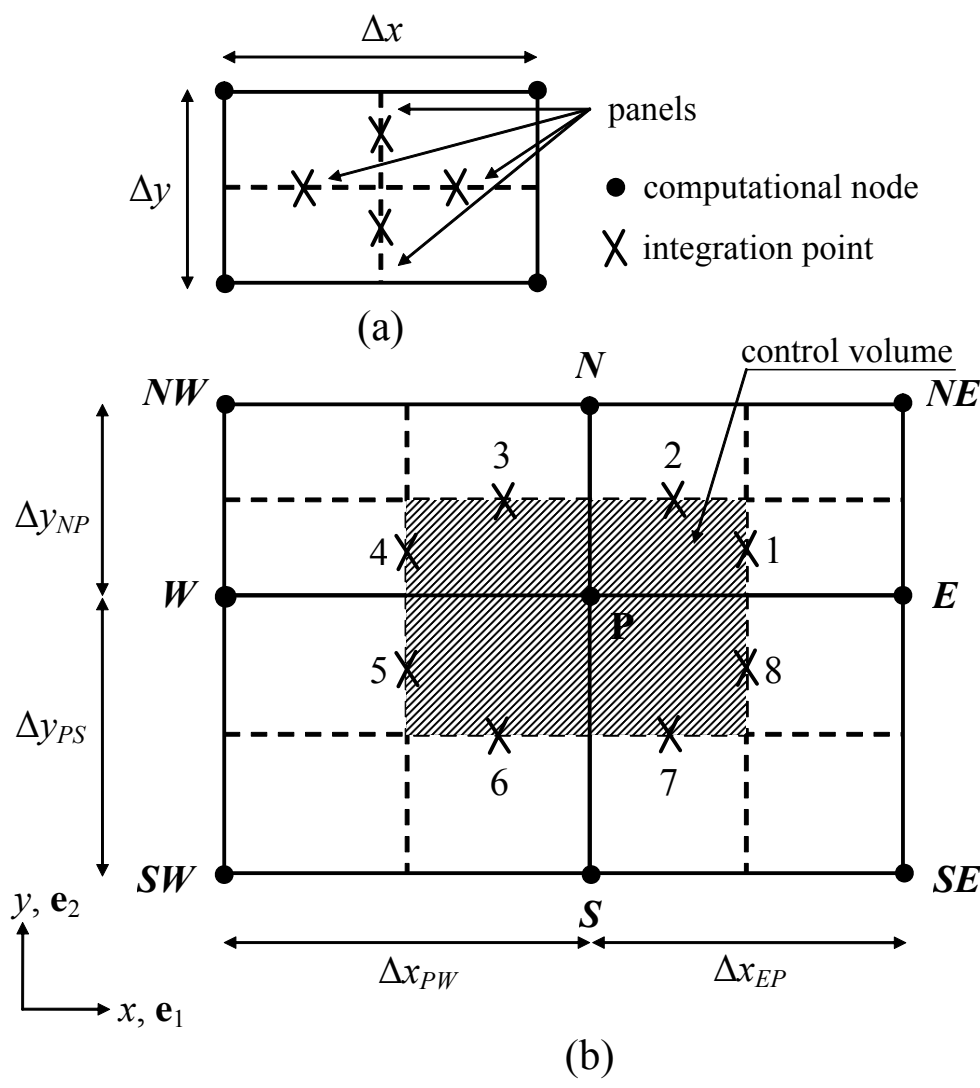


Figure 3.2: An element and a control volume in a 2D Cartesian grid.

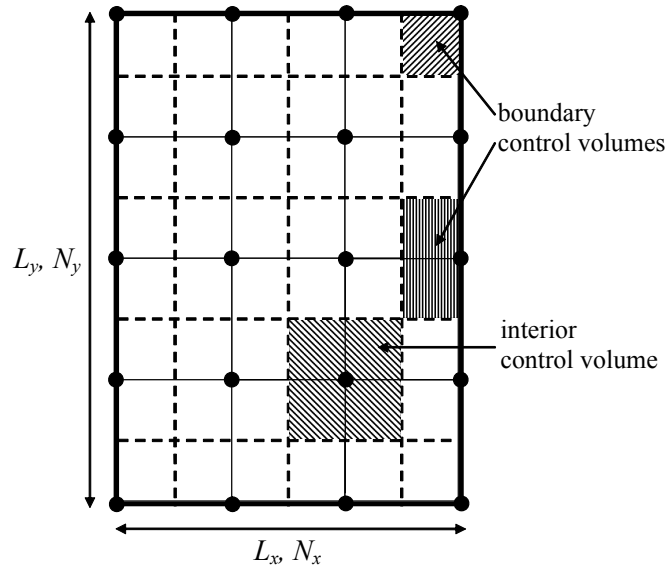


Figure 3.3: A 4×5 grid for a rectangular enclosure.

3.3 Solver

As stated in Chapter 2, to solve a radiation problem with the Q_L method, the α^l distribution should be obtained from a method like the FVM or DOM. In this research, the FVM has been used which was explained before in the first chapter.

The Q_L equations for a 2D Cartesian grid are completely derived in Appendix B and the solution procedure was explained in Chapter 2. In all of the problems solved in this research, the temperature field is known or not connected to radiation; the “solution procedure”, therefore, refers to the second solution procedure in Chapter 2. In this section, the solver and convergence criteria for solving the FVM and Q_L equations are described.

3.3.1 The Q_L Equations

After updating the coefficients and the source term in Eq.(2.27) for each node with the new α^l distribution obtained from the FVM (or in the first cycle, from the initial guess), the resulting set of linear algebraic equations are solved to find the I_a field. These equations are elliptic in nature and an iterative solver is required. This is the third step in the solution procedure.

To solve the Q_L equations efficiently, an additive correction multigrid solver [48] has been used. The additive correction multigrid solver is widely used in CFD and has been shown to accelerate the iterative solution substantially especially when the matrix of coefficients is not diagonally dominant.

A fixed “V” cycle with the point Gauss-Seidel as the smoother has been used in the additive correction multigrid solver. In both prolongation and restriction, the smoother sweeps each level once from the bottom-left corner to the top-right corner of the enclosure. Each control volume in the coarse grid consists of $MN_x \times MN_y$ control volumes of the finer grid and in most of the cases, the coarsest grid has only one control volume: the entire solution domain.

The iterative solution is started by an initial guess, the I_a field from the previous cycle or $I_a = 10^{-5} \text{ W m}^{-2}$ in the first cycle, and the iterative solution is terminated when the convergence criterion is satisfied. One iteration in this iterative solution is defined as accomplishing one fixed “V” cycle.

The convergence criterion for stopping the iterative solution of Eq.(2.27) is to reduce the scaled maximum residual below a specified target E_i . The residual of Eq.(2.27) for each control volume is defined as

$$r_P = \left| \frac{\sum_{nb} a_{nb} I_{a,nb} + b_P - a_P I_{a,P}}{a_P \times Rng} \right| \quad (3.1)$$

which is calculated at the end of each iteration. Rng is the range of I_a in the solution domain and can be approximated by $\sigma (T_{\max}^4 - T_{\min}^4) / \pi$ where T_{\max} and T_{\min} are the maximum and minimum temperatures of the enclosure surfaces.

The maximum residual in each iteration is $r_{\max} = (r_P)_{\max}$ and the r_{\max} on the first iteration is r_{\max}^o . The iterative solution is terminated when

$$r_{\max} / r_{\max}^o \leq E_i = 10^{-5} \quad (3.2)$$

This iterative solution gives the I_a field which is then inserted in the FVM equations.

3.3.2 The FVM Equations

Using the UDS in the FVM results in a parabolic-type set of linear algebraic equations which can be solved by marching (Step 5 of the solution procedure). This means that once the \bar{I} and I_b are known (from the Q_L method¹ and the temperature

¹See Appendix B (Eq.(B.7)) for the expression relating \bar{I} to I_a .

field²), the solution starts from the bottom and left surfaces and marches through all nodes into the top-right of the enclosure in directions included in the quadrant indicated in Fig.3.4 (a). This sweep gives the directional intensities in the solid angles which lie in those directions.

Since now the incoming radiation to the top and right surfaces are known, the intensities leaving these surfaces can be calculated from Eq.(1.11). Then a sweep can be started from the bottom and right surfaces through all nodes and this time, towards the top-left of the enclosure which gives the directional intensities in the solid angles which lie in directions included in the quadrant indicated in Fig.3.4 (b). Now the intensities leaving the top and left surfaces can be updated and then another sweep is started. Four sweeps should be done to determine directional intensities in all directions. The order of doing these sweeps is arbitrary.

Fig.3.4 shows the P control volume and its neighbors and indicates the four sweeping patterns schematically. This figure also specifies the computational nodes participating in calculating the directional intensities in node P in each sweep by solid circles. These nodes are always in upstream. Note that when the UDS is used, two panels in each side of the control volume can be combined to one with a single integration point located at its center (center of that side).

For black surfaces, intensities which satisfy Eq.(1.10) are obtained by the first 4 sweeps. However, these intensities may not be the final answer since \bar{I} values which came from the Q_L equations may not be correct because the Q_L equations had used the α^l distribution from the previous cycle. For reflecting surfaces, these intensities may not even satisfy Eq.(1.10) since the intensities leaving surfaces may be incorrect. For both black and non-black surfaces, only the first 4 sweeps are done and the new α^l distribution is calculated. Then the coefficients and the source term in Eq.(2.27) for each node are updated with the newly obtained α^l distribution. Before solving the I_a equations again with the updated coefficients and source term, the convergence criterion of the cycle should be checked.

3.4 Convergence Criterion for Cycle

When the directional intensities are updated, the coefficients in the Q_L equations change so that these equations are no longer satisfied by the most recent values of I_a . The procedure of calculating I_a , I^l (and therefore α^l), and the coefficients of the I_a equations is therefore repeated until a cycle convergence criterion is met.

²In radiative equilibrium, I_b is obtained from $I_b = I_a$.

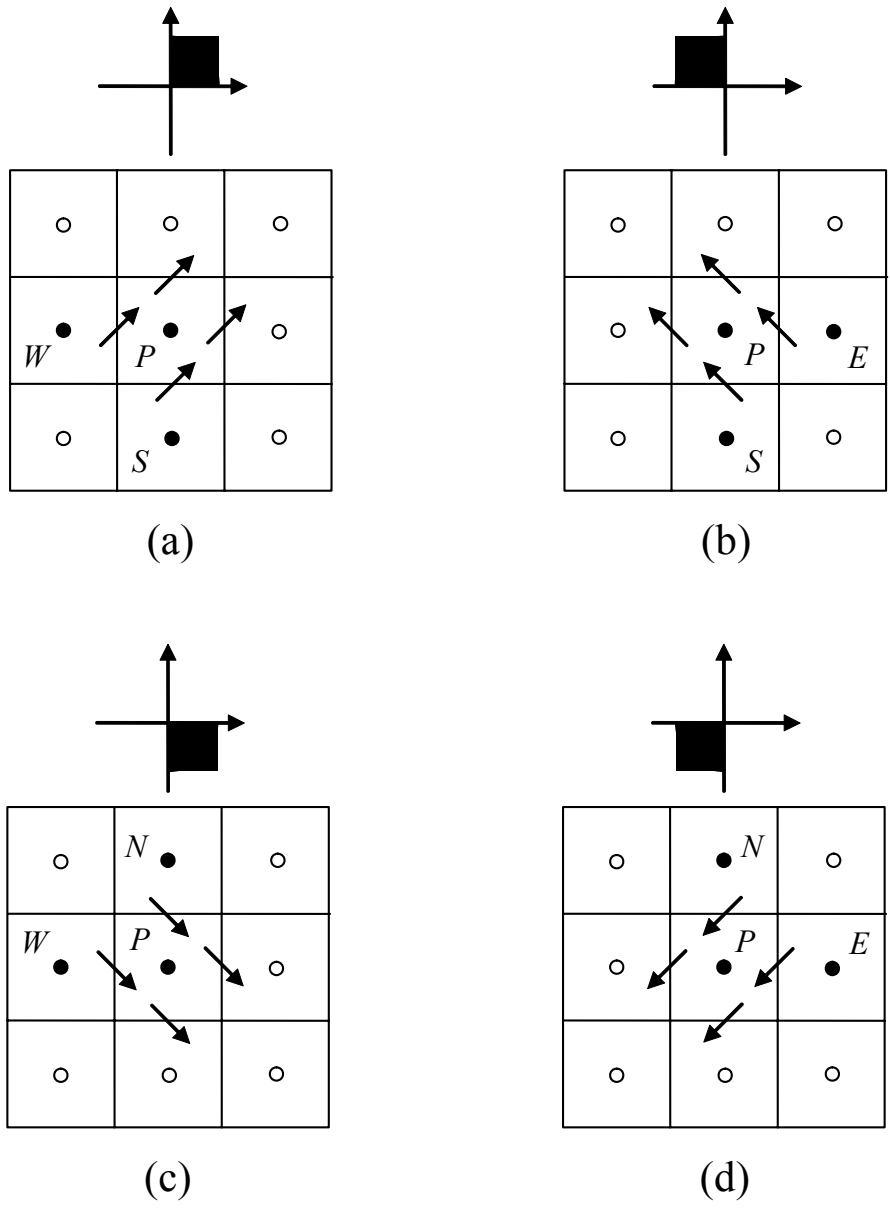


Figure 3.4: Four sweeping patterns for a rectangular enclosure.

The convergence criterion for cycle is

$$R_{\max}/R_{\max}^o \leq E_o = 10^{-5}$$

which is checked at the end of each cycle where E_o is a specified target and $R_{\max} = (R_P)_{\max}$. R_P is calculated in the same way as r_P (Eq.(3.1)), except that the coefficients have been updated by the newly obtained α^l distribution. R_{\max}^o is the maximum residual on the first cycle.

Fig.3.5 shows the complete solution procedure by a flowchart.

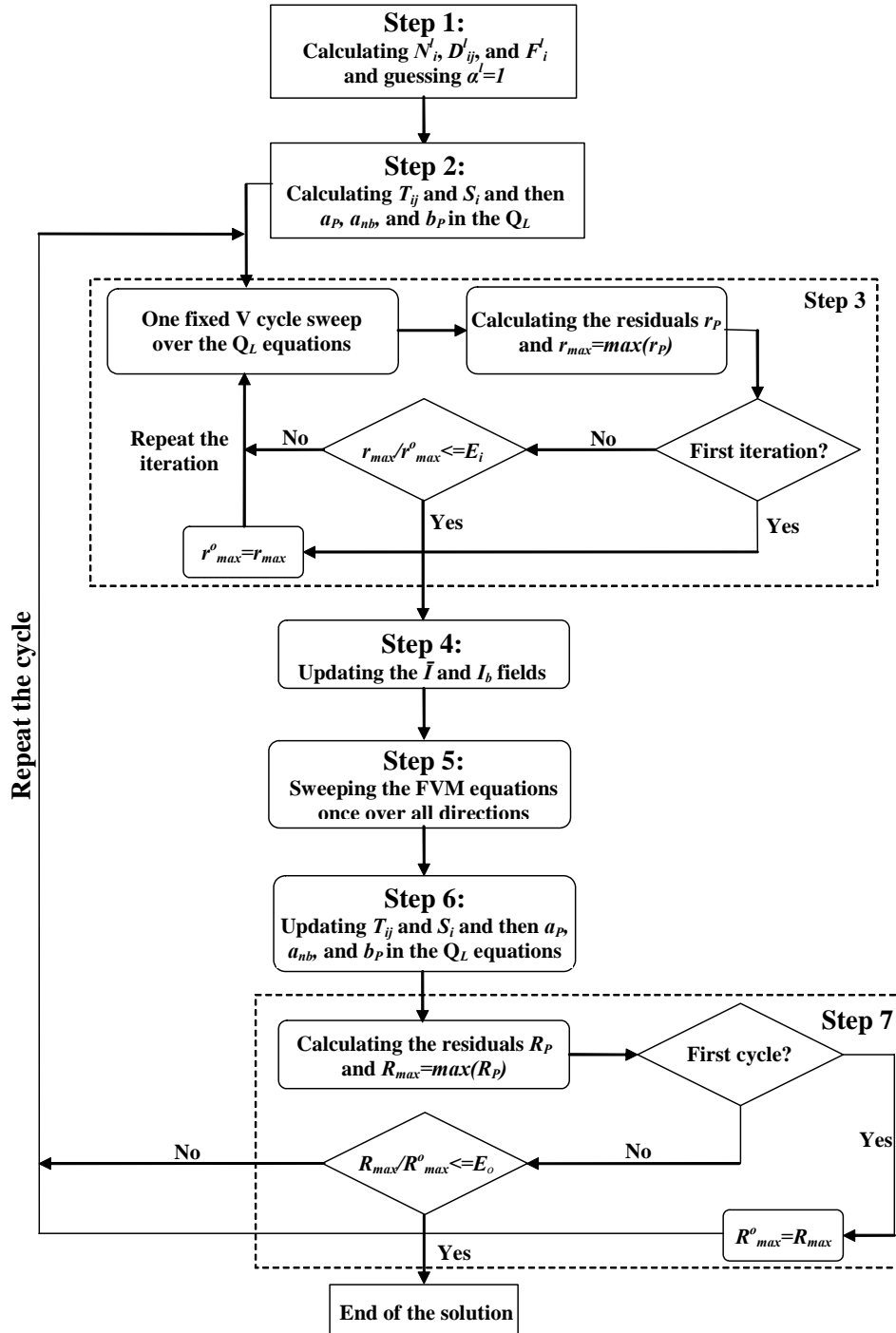


Figure 3.5: The complete solution procedure of the Q_L method.

Chapter 4

Results

In this chapter, the Q_L method is applied to several 1D and 2D benchmark problems and results are compared with the exact solutions, and the results of the FVM¹ and P_1 method to study the accuracy of the Q_L method.

To illustrate the efficiency of the Q_L method, the number of cycles and work units (WU) required to solve these problems have been reported and compared with the cost of the FVM with explicit update. Another important issue is robustness which has been studied at the end of this chapter.

The formulation of the Q_L method and numerical procedure were completely described in Chapters 2 and 3. Before presenting the results, the dimensionless parameters used in this chapter need to be introduced:

- Nondimensional distance: $x^* = x/L_x$ and $y^* = y/L_y$.
- Optical thickness: $\kappa^* = \kappa L_y$.
- Nondimensional heat transfer on the hot bottom surface: $q^* = q/\sigma (T_h^4 - T_c^4)$ where q is the surface heat flux on the bottom surface and T_h and T_c are the temperatures of the hot and cold surfaces, respectively. The surface heat flux is defined as [1]:

$$q = \epsilon_B \sigma T_B^4 - \underbrace{(1 - \rho_B)}_{\epsilon_B} \iint_{\omega^-} I \mathbf{s} \cdot \mathbf{n} d\omega$$

¹As stated before, the UDS has been used in the FVM to solve these test cases. The convergence criterion for the FVM solution is reducing the scaled residual of Eq.(1.10) (calculated in the same way as Eqs.(3.1) and (3.2)), in all control volumes and solid angles, below 10^{-5} .

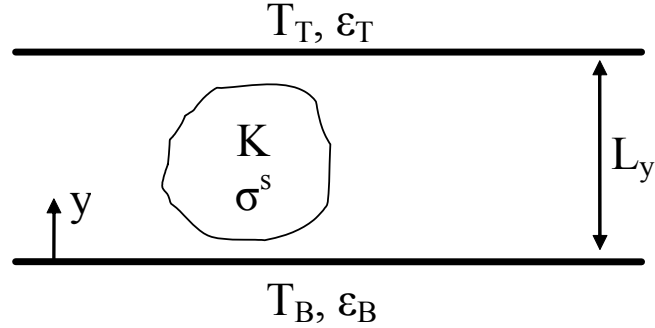


Figure 4.1: Geometry of the 1D problems.

where ϵ_B is the surface emissivity, T_B is the temperature of the bottom surface, and ω^- is the range of solid angles carrying energy out of the medium to the bottom surface. q^* is reported along the first half of the bottom surface ($0 \leq x^* \leq 0.5$ and $y^* = 0$).

- Reflectance : $q_R^* = q_R / \sigma T_B^4$ where q_R is the incident radiant heat flux on the hot bottom surface:

$$q_R = \iint_{\omega^-} I \mathbf{s} \cdot \mathbf{n} d\omega$$

- Nondimensional temperature: $T^* = (T^4 - T_c^4) / (T_h^4 - T_c^4)$. T^* is reported along the centerline of the enclosure ($x^* = 0.5$ and $0 \leq y^* \leq 1$).

4.1 One-Dimensional Problems

The geometry of the 1D problems is an enclosure with a very small aspect ratio which approaches a plane medium enclosed between two parallel isothermal, gray, diffuse plates. The top surface is cold $T_T = T_c = 0$ K and the bottom surface is hot $T_B = T_h = 100$ K. Fig.4.1 shows the geometry of the 1D problems.

To obtain the solution of the 1D problems, the 2D code has been used with $AR = 1/3000$, $N_x \times N_y = 5 \times 8$ control volumes, and $N_\theta \times N_\phi = 1 \times 16$ solid angles. The mesh of type “b” in Fig.1.4 is used for the angular grid, and $N_\theta = 1$ means that each solid angle covers the complete range of the polar angle ($0 \leq \theta \leq \pi$). Four levels are used in the multigrid solver, and each coarse-mesh block consists of

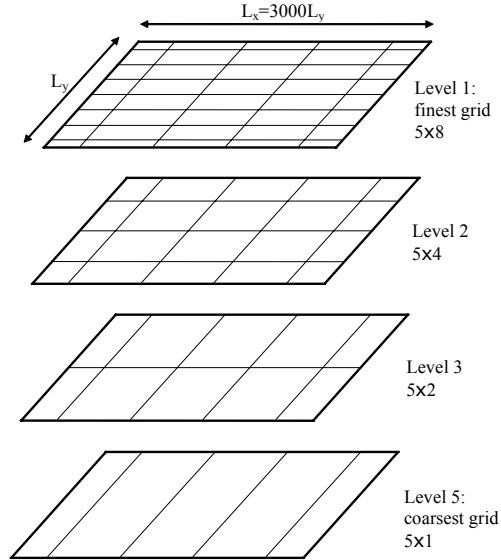


Figure 4.2: Four levels of the spatial mesh used in the multigrid solver in the 1D problems.

1 control volume in the x direction and 2 control volumes in the y direction of the finer mesh ($MN_x \times MN_y = 1 \times 2$) (Fig.4.2). Note that in the 1D problems, the coarsest grid is made up of 5 blocks where each of them spans the domain in the y direction².

Five 1D benchmark problems are solved in this research and q^* or q_R^* is reported at the center of the bottom surface:

- Case 1. Purely isotropically scattering medium between parallel black plates.
- Case 2. Purely isotropically scattering medium between parallel partially reflecting plates.
- Case 3. Purely anisotropically scattering medium, with a linear phase function, between parallel black plates.
- Case 4. Purely anisotropically scattering medium, with a non-linear phase function, between parallel black plates.

²In the 1D problems, the coarsest mesh does not consist of only one control volume (the solution domain) because of the very small aspect ratios of the blocks which may adversely affect the performance of the multigrid solver.

Case 5. Isothermal absorbing-emitting medium between parallel black plates.

Note that the medium in Cases 1 and 2 is the same as an absorbing-emitting medium in radiative equilibrium.

4.1.1 Isotropic Scattering

Case 1: Black Surfaces

The first problem is to find the radiative heat transfer in a purely isotropically scattering medium ($\Omega = 1, \Phi = 1$) contained between two black surfaces. Heaslet and Warming [49] have presented a very precise (“exact”) solution for this problem.

Accuracy Fig.4.3 compares the q^* values predicted by the Q_L method with the exact solution and results of the P_1 and finite volume methods for a wide range of optical thicknesses ($10^{-2} \leq (\kappa^* = \sigma^s L_y) \leq 10^3$).

This comparison shows that the FVM accurately predicts the radiative heat transfer in the optically thin media, but the accuracy of the solution degrades as the optical thickness increases. The fact that the convergence rate is very slow in the optically thick limit (see Fig.4.5) may raise a doubt that this inaccuracy is a result of an unconverged solution. This doubt is false and it has been ensured that the solutions are fully converged. In fact, this deterioration is a result of using the UDS which is not accurate when the medium is strongly participating. In this condition, the intensity changes significantly between the upstream node and the integration point whereas this variation is not accounted in the UDS.

Fig.4.4 shows this explanation schematically. The directional intensity distributions at two computational nodes, A and B , in a strongly participating medium are presented as nearly isotropic. When the UDS is used, the I^l distribution at the integration point ip is approximated from the upstream nodes (A in the “+” direction and B in the “-” direction), which results in the dashed-line distribution. The actual I^l distribution at ip is presented by the solid line, which shows the enormous error in the UDS approximation that results in an incorrect radiant heat flux at the face of the control volume. Because of this incorrect radiant heat flux, the I^l and I_a values at the downstream nodes are not accurate and the error is propagated downstream and accumulated. As addressed before, the reason of the difference between the actual and approximated distributions is that the UDS

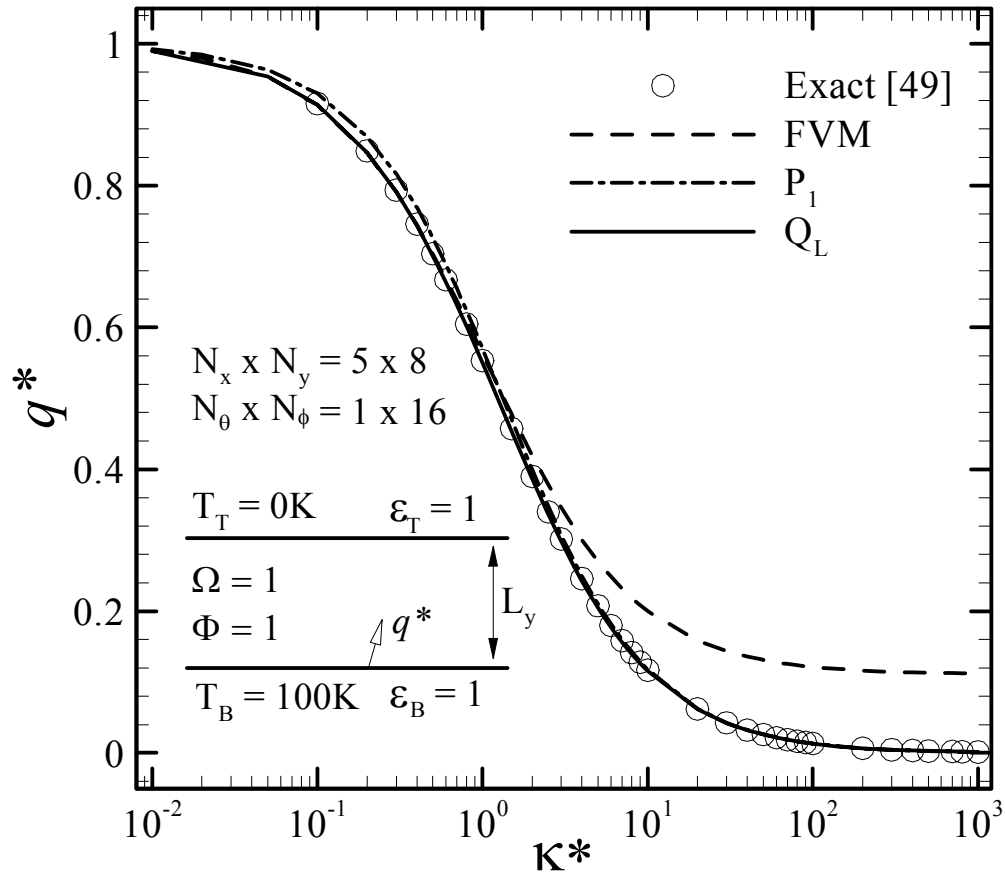


Figure 4.3: Nondimensional heat transfer on the hot bottom surface for a purely isotropically scattering plane medium enclosed between two parallel black surfaces (Case 1).

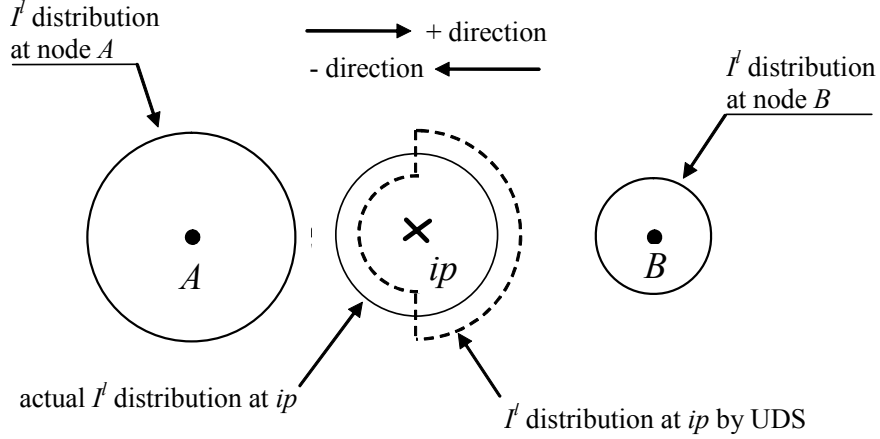


Figure 4.4: The UDS approximation in a strongly participating medium.

does not account for the attenuation between the upstream node and the integration point. Grid refinement overcomes this problem by decreasing the attenuation strength via decreasing the distance between the upstream node and the integration point. Therefore, the FVM solution approaches the exact results with grid refinement³.

The P₁ method performs surprisingly well in this 1D problem (the maximum error is about 3%), a behavior which has been observed before [50, 51]. The reason is the semi-isotropic intensity distribution in this 1D problem [51].

The Q_L method gives a very accurate solution for these coarse spatial and angular grids where the maximum error is around 1.5%. It is worthwhile mentioning that although the FVM has a poor accuracy in the optically thick limit, the Q_L method, which obtains the α^l distribution from the FVM, gives very precise results in the strongly participating media.

The reason for this very good performance is that, although the FVM is not able to predict the I^l and I_a distributions accurately for the large optical thicknesses, the α^l distribution is not affected severely by this error and the FVM gives a nearly isotropic intensity distribution ($I^l \approx I_a$) in each node since the source term is strongly dominant over the directional terms in the discretized RTE. Therefore, $\alpha^l = I^l/I_a \approx 1$ is calculated which is the correct α^l distribution in the strongly

³It is clear that this inaccuracy is a result of using the first order discretization scheme (UDS). Applying the higher-order methods results in very accurate results for any optical thickness on the coarse grids.

participating medium. Consequently, the correct α^l distribution is fed into the Q_L equations.

The Q_L method calculates the radiant heat flux at the integration points from the gradient of I_a and its value at ip (Eq.(2.22)) by a second-order linear approximation and does not need the I^l distribution at ip . Therefore, with an accurate α^l distribution which is provided by the FVM, the Q_L method is able to accurately calculate the radiative heat transfer in the strongly participating medium.

Convergence Rate Fig.4.5 shows the number of cycles required to achieve convergence for the FVM and Q_L method. It is observed that the number of cycles in the FVM increases sharply for $\kappa^* \geq 1$ because of the strong directional coupling between intensities as a result of the scattering.

The Q_L method converges in a few cycles for the whole range of optical thicknesses where the maximum number of cycles is 10 in the worst case ($\kappa^* = 4$ and 5). In the optically thin limit, the correct results are obtained by a few cycles since the directional coupling is weak and the FVM gives the correct α^l distribution after a small number of cycles. In the optically thick limit, the Q_L equations establish the correct I_a distribution after a few cycles and the FVM gives the correct α^l distribution for this I_a field since the source term is dominant. Therefore, the solution converges in a few cycles in this limit as well. Consequently, the maximum number of cycles occurs for the intermediate optical thicknesses where the directional and source terms are in balance. However, even for the intermediate optical thicknesses, the Q_L method converges rapidly.

Note that based on the definition of cycle in Chapter 2, the P_1 method converges in one cycle. It should be pointed out that since the computational cost of each cycle is different in these three methods, the number of cycles is not an appropriate indicator of the cost of each method. The actual cost can be measured in work unit which is reported for 2D problems. However, Fig.4.5 depicts that the Q_L method, in contrast to the FVM, has a very good convergence rate for both of the optically thin and thick media.

Case 2: Partially Reflecting Surfaces

This test case is the same as the first one except that here both surfaces are partially reflecting, $\epsilon_B = \epsilon_T = 0.1$. Fig.4.6 compares the q^* values predicted by the Q_L , P_1 , and finite volume methods with the exact solution, and Fig.4.7 shows the number of cycles required to achieve convergence in this problem.

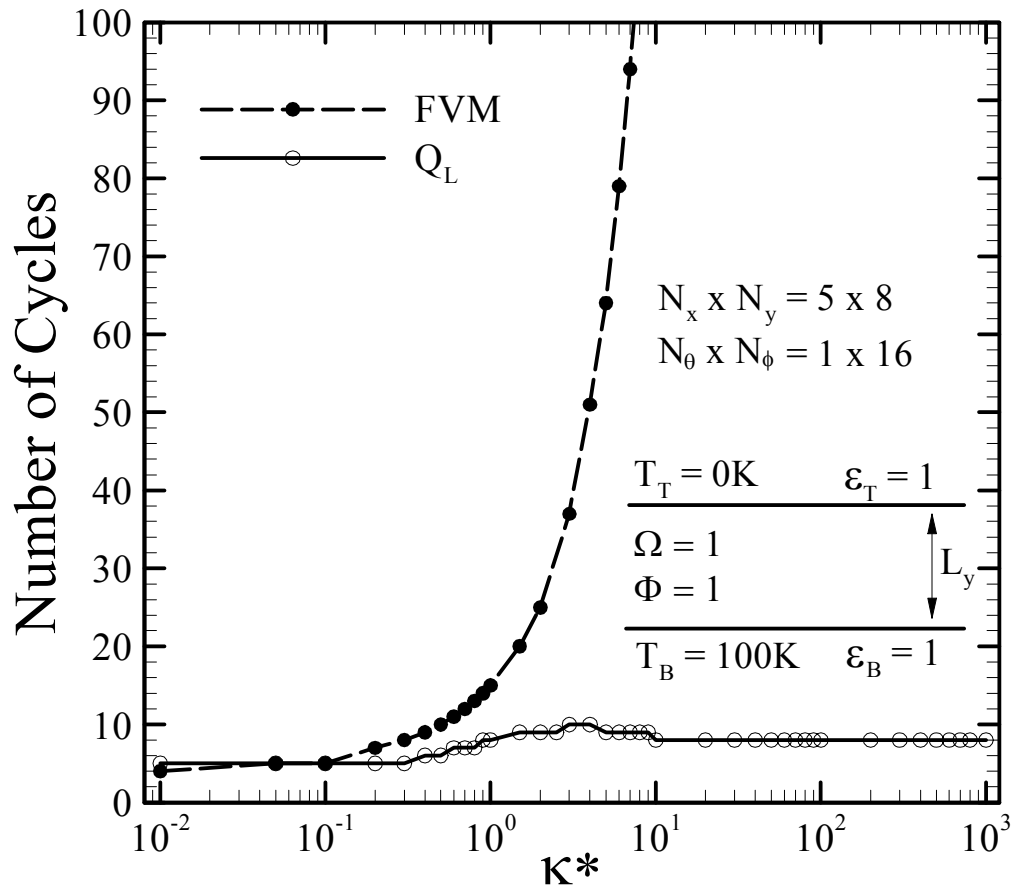


Figure 4.5: Number of cycles required to achieve convergence for a purely isotropically scattering plane medium enclosed between two parallel black surfaces (Case 1).

Results in both figures have the same trends as Figs.4.3 and 4.5 for Case 1. However, the number of cycles for the FVM is much larger in Case 2 because of the strong coupling between the intensities leaving a reflecting surface and the incident intensities on that surface. The Q_L method is found to have a very good convergence rate except for very small optical thicknesses.

4.1.2 Anisotropic Scattering

Cases 1 and 2 dealt with the isotropic scattering and showed the good performance of the Q_L method in predicting the radiative heat transfer in 1D problems for the simplest scattering phase function. In Cases 3 and 4, the Q_L method is applied to problems with linear and non-linear anisotropic scattering to study the behavior of this method for complex phase functions. A relatively fine angular grid has been used for Cases 3 and 4: $(N_x \times N_y) \times (N_\theta \times N_\phi) = (5 \times 16) \times (4 \times 24)$.

Case 3: Linear Phase Function

The medium in this test case is purely scattering ($\Omega = 1$) with a linear scattering phase function ($\Phi(\mathbf{s}', \mathbf{s}) = 1 + a_1 \cos \Psi$) where Ψ is the angle between \mathbf{s} and \mathbf{s}' (Fig.1.1). Both of the top and bottom surfaces are black.

Fig.4.8 compares the reflectance on the bottom surface calculated by the Q_L method with the exact results for $a_1 = 0, 0.5$, and 1 in the range of $1 \leq \sigma^s L_y \leq 10$. The exact solution has been obtained from Busbridge and Orchard [52].

The Q_L method results are in excellent agreement with the exact solution for this set of grids (maximum error is 1%) and the number of cycles required for convergence is smaller than 11.

Case 4: Non-Linear Phase Function

The Q_L method has been applied to a problem where a purely scattering medium ($\Omega = 1$) with a non-linear scattering phase function ($\Phi(\mathbf{s}', \mathbf{s}) = 1 + a_1 \cos \Psi + a_2(3 \cos^2 \Psi - 1)$). The medium is enclosed between two parallel black surfaces.

Fig.4.9 shows the calculated reflectance on the bottom surface for $a_1 = 0, 1$, and 1.5, $a_2 = 0.25$, and $1 \leq \sigma^s L_y \leq 10$. Orchard [53] has presented the exact solution for this problem.

The Q_L solution is found to be in a good agreement with the exact solution where the maximum error for $a_1 = 0$ and 1 is 1% for this set of grids. For $a_1 = 1.5$,

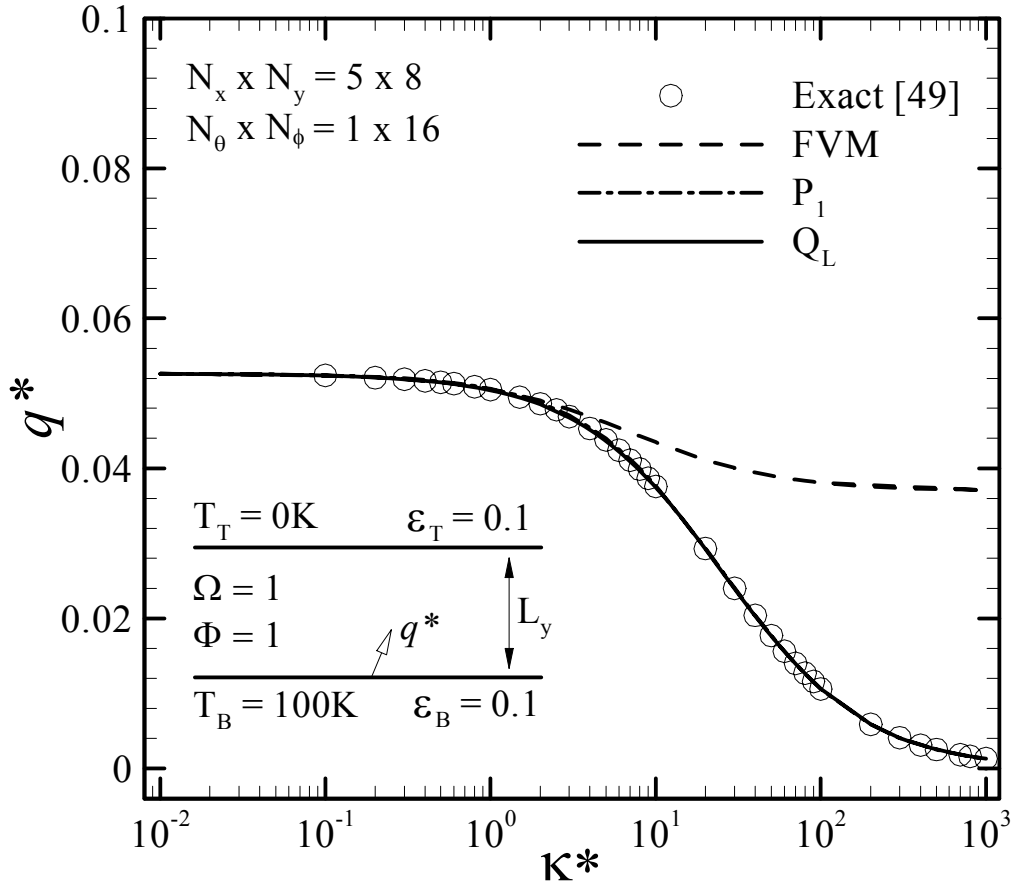


Figure 4.6: Nondimensional heat transfer on the hot bottom surface for a purely isotropically scattering plane medium enclosed between two parallel partially reflecting surfaces (Case 2).

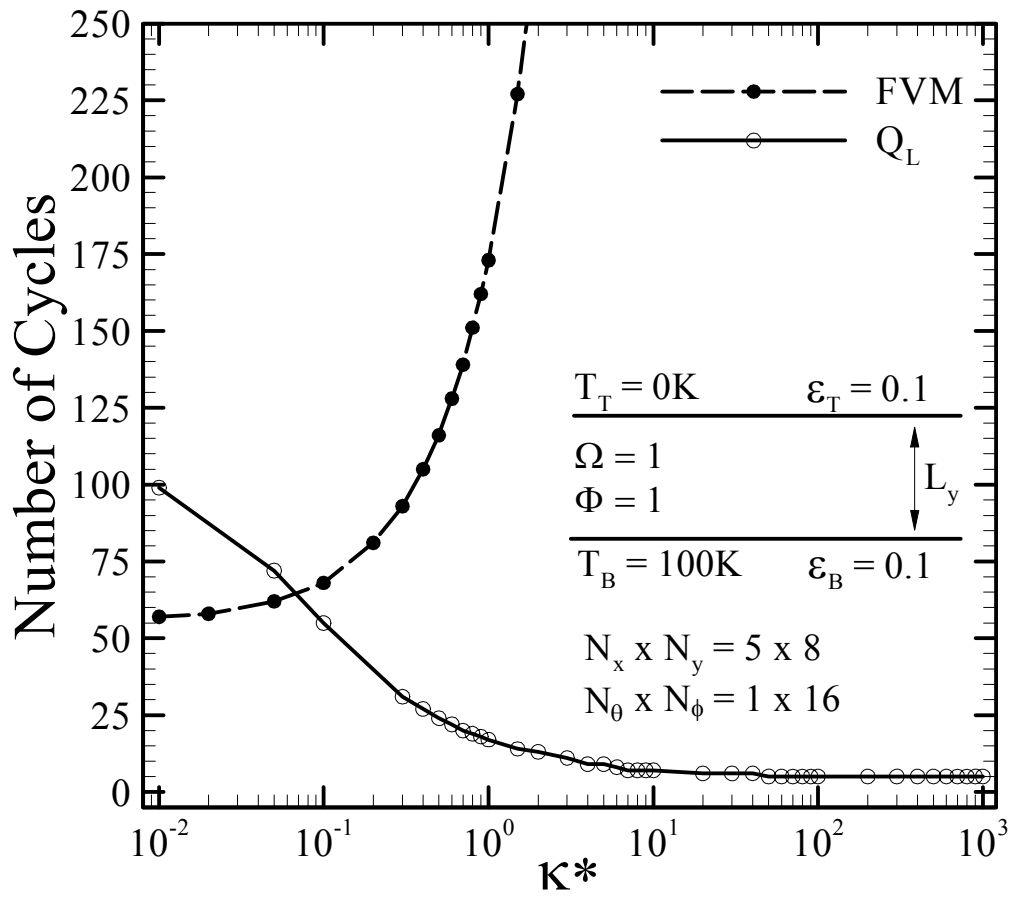


Figure 4.7: Number of cycles required to achieve convergence for a purely isotropically scattering plane medium enclosed between two parallel partially reflecting surfaces (Case 2).

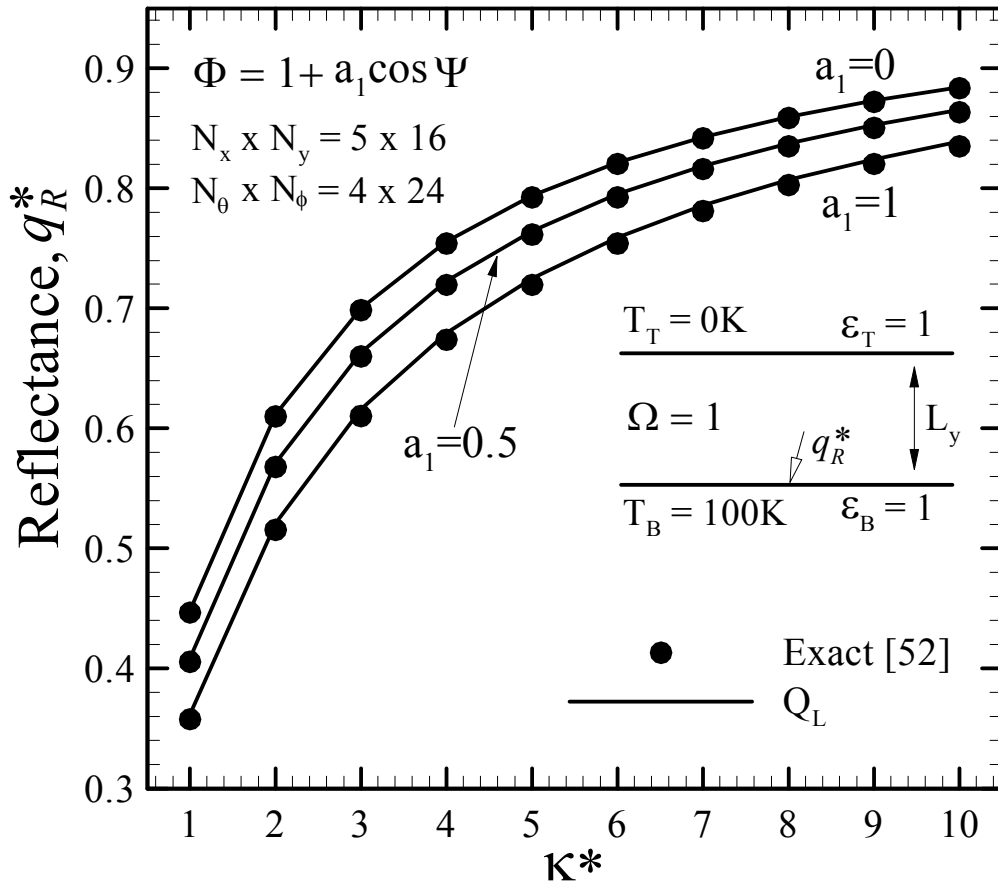


Figure 4.8: Reflectance on the hot bottom surface for a purely scattering plane medium, with a linear phase function, enclosed between two parallel black surfaces (Case 3).

the error is around 1.8% for $\kappa^* = 1$, but decreases rapidly with increasing κ^* and is around 1% for $\kappa^* \geq 5$. The Q_L solution for this problem converges within 12 cycles in the worst case.

4.1.3 Isothermal Slab

The fifth test case is radiative heat transfer in an emitting-absorbing isothermal slab ($\Omega = 0$) which is contained between two parallel black surfaces. The medium is maintained at $T_G = 50$ K and the top and bottom surfaces are at the same temperature $T_T = T_B = 100$ K. In this case, q^* is defined as $q^* = q / (\sigma T_B^4 - \sigma T_G^4)$.

A relatively fine spatial grid $N_x \times N_y = 5 \times 16$ has been used for this problem to capture the sharp variations near the surfaces.

Fig.4.10 compares the results of the Q_L , P_1 , and finite volume methods with the exact solution. These results show that all of the three methods predict the radiative heat transfer accurately for the optically thin media but the accuracy of the P_1 method degrades rapidly as the absorption coefficient increases. The reason for the inaccuracy in the P_1 results is the intensity discontinuity which exists at the surface as a result of the temperature jump [3]. The maximum error in the Q_L and finite volume predictions is about 4% while the P_1 method has a maximum error of 15%.

Solving this problem is very inexpensive for any optical thickness since the intensities in different directions are decoupled. In fact, the FVM converges within 2 cycles and the Q_L method requires only 4 cycles to converge.

4.2 Two-Dimensional Problems

In this section, the method is extended to 2D test cases and its performance is examined for more complex problems. As mentioned earlier, to measure the actual cost of the solution, a work unit (WU) should be defined and used. In this research, one WU for a specific set of spatial and angular grids is defined as the computational effort required to do 10 explicit updates in the FVM on that grid (i.e. 10 cycles of the FVM). Hence, the work unit is found by dividing the CPU time for the solution by the CPU time for accomplishing 10 FVM cycles. With this definition of the WU, the actual cost of the FVM and Q_L method can be measured and compared.

Six 2D test cases have been solved in this section:

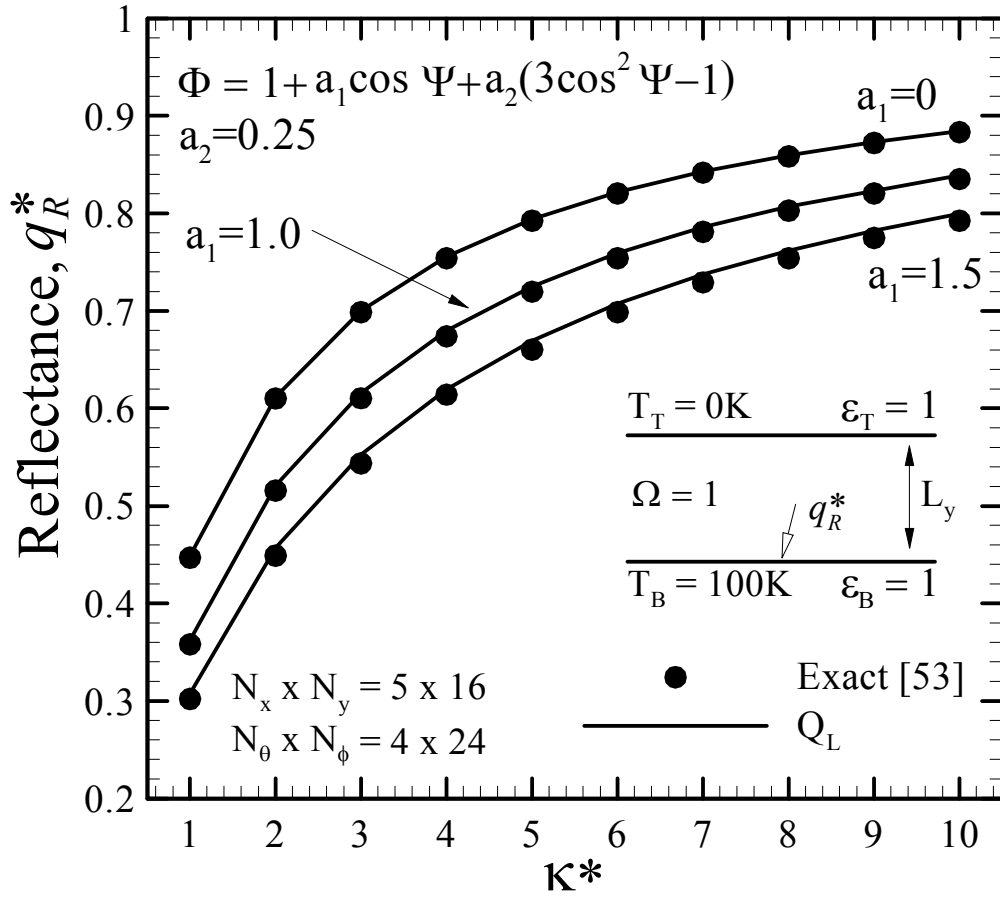


Figure 4.9: Reflectance on the hot bottom surface for a purely scattering medium, with a non-linear phase function, enclosed between two parallel black surfaces (Case 4).

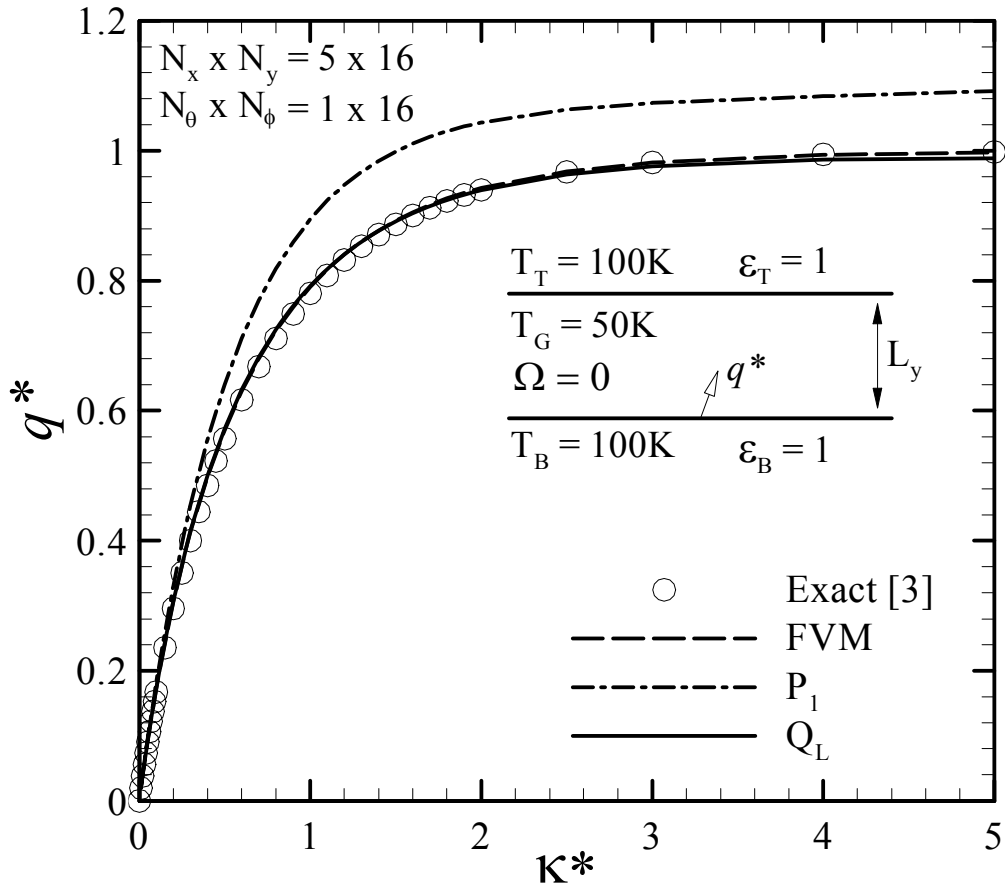


Figure 4.10: Nondimensional heat transfer on the bottom surface of an isothermal slab (Case 5).

- Case 6. Purely isotropically scattering in square enclosures with black and partially reflecting surfaces.
- Case 7. Purely isotropically scattering in wide and tall enclosures with black surfaces.
- Case 8. Absorbing-isotropically scattering medium in square enclosures with black surfaces.
- Case 9. Absorbing-anisotropically scattering medium in square enclosures with black surfaces.
- Case 10. Purely anisotropically scattering, with the linear, non-linear and Delta-Eddington phase functions, in square enclosures with black surfaces.
- Case 11. Isothermal absorbing-emitting medium in square enclosures with black surfaces.

4.2.1 Pure Isotropic Scattering

Case 6: Square Enclosure

The first 2D benchmark problem is a purely isotropically scattering medium ($\Omega = 1, \Phi = 1$) enclosed in a square enclosure where the bottom surface is hot $T_B = T_h = 100$ K and the other three surfaces are cold $T_c = 0$ K. The exact solution of this problem has been presented by Crosbie and Schrenker [54].

The spatial grid is $N_x \times N_y = 27 \times 27$ with 4 levels in the multigrid solver ($MN_x \times MN_y = 3 \times 3$). $N_\theta \times N_\phi = 1 \times 24$ solid angles have been used for the angular discretization.

Accuracy Fig.4.11 compares the q^* along the bottom surface predicted by the Q_L method with the exact solution and results of the FVM and P_1 method for three optical thicknesses $\kappa^* = 0.25, 1, \text{ and } 10$. Figs.4.12, 4.13, and 4.14 show the nondimensional temperature T^* along the centerline for these three optical thicknesses. The temperature distribution has been obtained from $I_b = I_a$ as a result of the radiative equilibrium.

These comparisons show the poor performance of the P_1 method except in the optically thick medium, which was expected. This method overpredicts the heat transfer for $\kappa^* = 0.25$ and 1 especially near the corner where a discontinuity in the

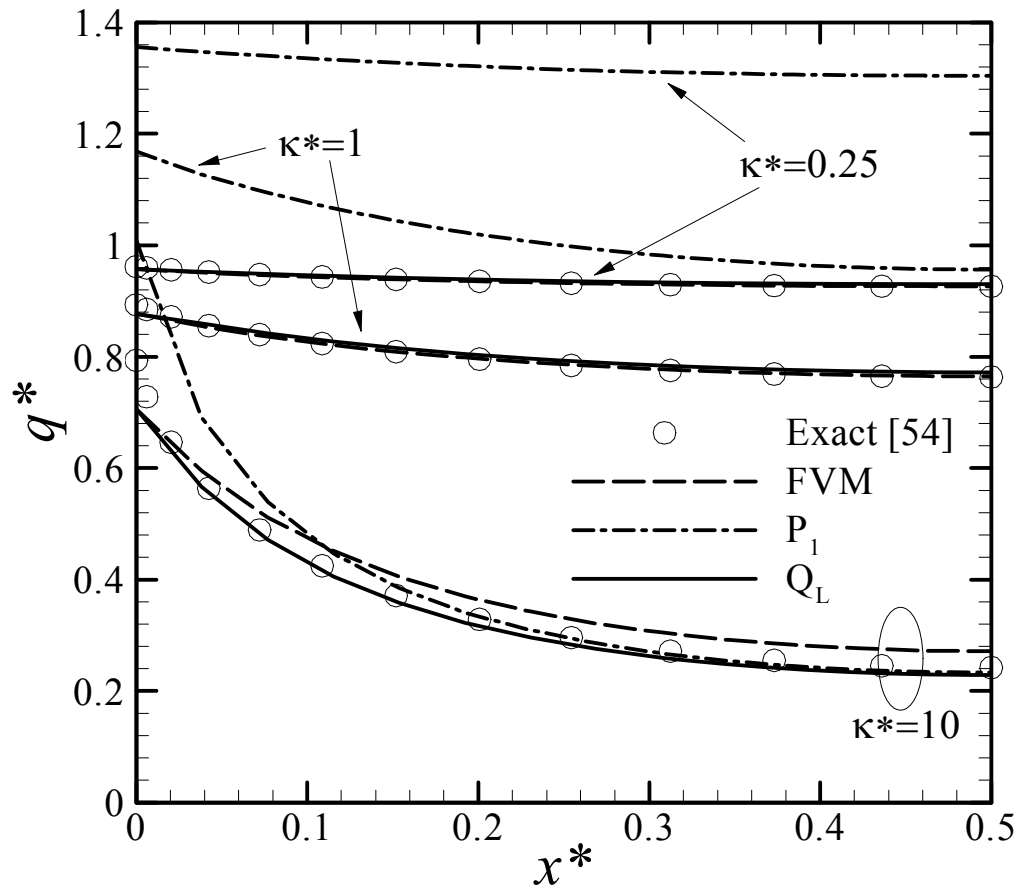


Figure 4.11: Nondimensional heat transfer on the hot bottom surface for a purely isotropically scattering medium enclosed in a square enclosure with black surfaces (Case 6).

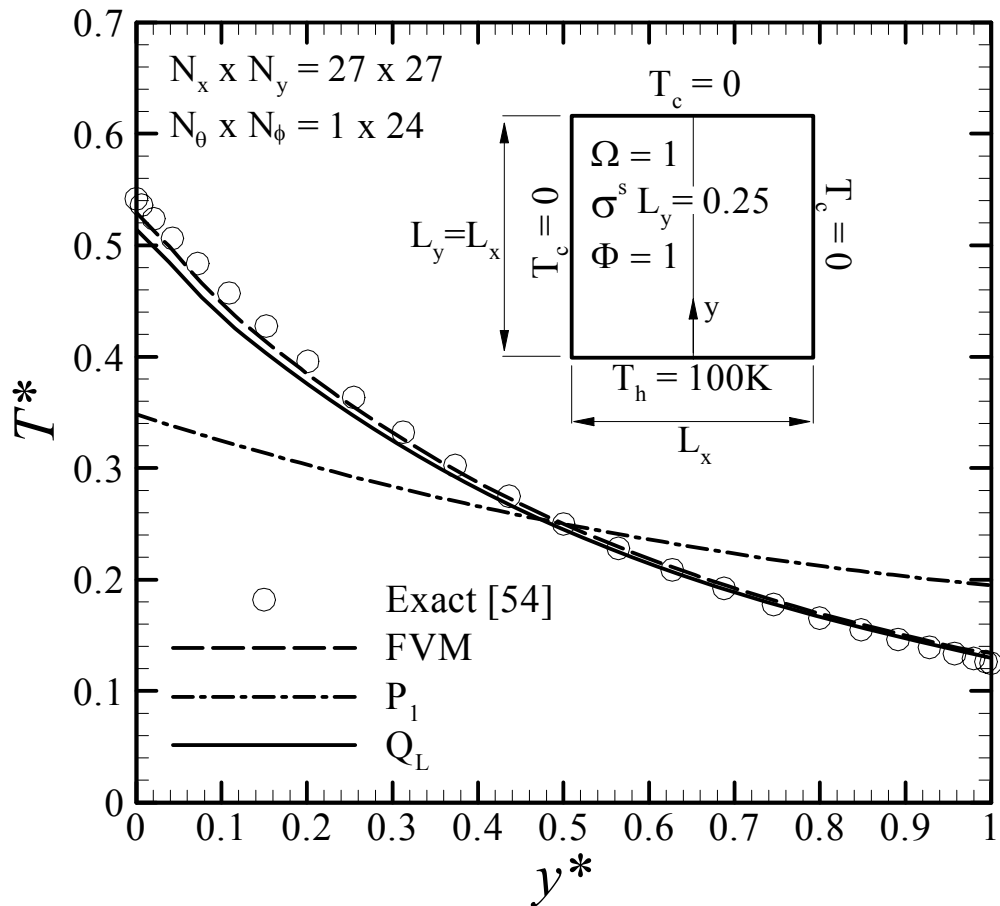


Figure 4.12: Nondimensional temperature along the centerline for a purely isotropically scattering medium enclosed in a square enclosure with black surfaces for $\kappa^* = 0.25$ (Case 6).

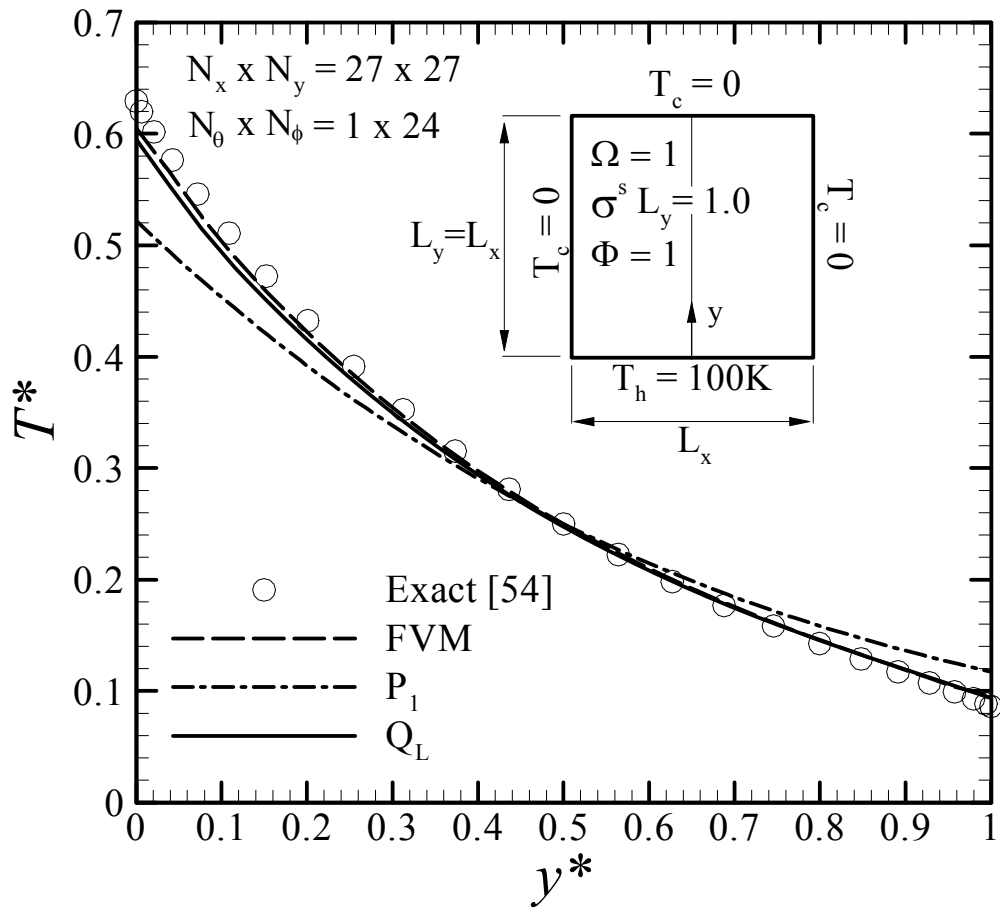


Figure 4.13: Nondimensional temperature along the centerline for a purely isotropically scattering medium enclosed in a square enclosure with black surfaces for $\kappa^* = 1.0$ (Case 6).

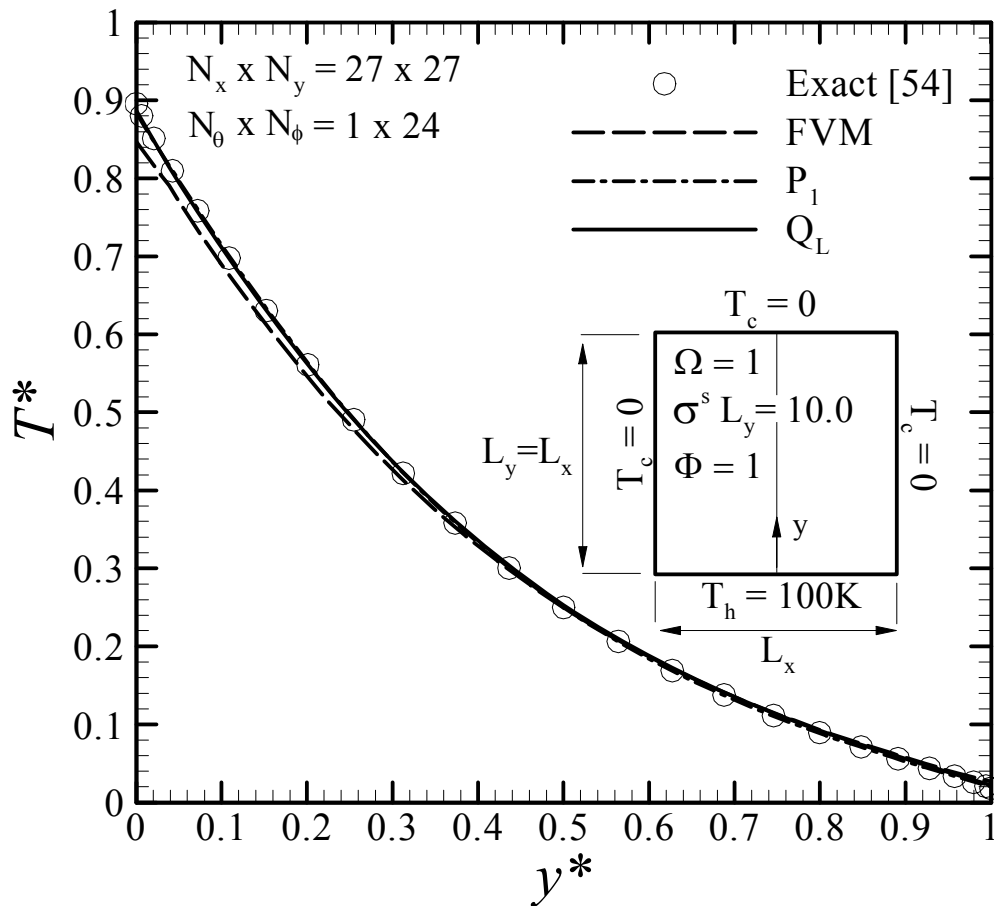


Figure 4.14: Nondimensional temperature along the centerline for a purely isotropically scattering medium enclosed in a square enclosure with black surfaces for $\kappa^* = 10.0$ (Case 6).

surface emissive power exists. This discontinuity severely affects the accuracy of the P_1 predictions even for $\kappa^* = 10$.

The FVM accurately predicts the radiative heat transfer except for the optically thick medium as a result of the UDS. The reason of this inaccuracy was explained for the 1D problems and as mentioned, the FVM results approach the exact solution with spatial grid refinement at the expense of more cost and memory (or with a higher-order scheme which increases the complexity). The Q_L method yields very accurate q^* and T^* distributions for all of these three small, medium, and large optical thicknesses for this set of coarse grids.

Fig.4.15 quantifies the error in the solution of the finite volume, P_1 , and Q_L methods for a wide range of optical thicknesses. Results are reported for $(N_x \times N_y) \times (N_\theta \times N_\phi) = (27 \times 27) \times (1 \times 24)$, with 4 levels in the multigrid solver ($MN_x \times MN_y = 3 \times 3$).

The error in the predicted q^* at the center of the bottom surface has been calculated as

$$\text{error percentage} = \frac{|q_{exact}^* - q_{predicted}^*|}{q_{exact}^*} \times 100$$

where q_{exact}^* is obtained by extrapolating the results from three spatial grids: 27×27 , 81×81 , and 243×243 .

Fig.4.15 shows that the error of the Q_L method is always less than 1% while the P_1 and finite volume methods have this accuracy for $\kappa^* \geq 10$ and $\kappa^* \leq 1$, respectively. Again it should be pointed out that the FVM suffers from the inaccuracy of the UDS in the strongly participating medium. In fact, the UDS is not able to recover the diffusion approximation for the optically thick limit. The reason for the poor performance of the P_1 method in the optically thin media is that the intensity distribution is strongly directional-dependent in this limit.

Cost Figs.4.16 and 4.17 compare the solution cost and number of cycles respectively for the finite volume and Q_L methods for a wide range of optical thicknesses, and black and partially reflecting surfaces. Results are reported for a set of fine spatial and angular grids $(N_x \times N_y) \times (N_\theta \times N_\phi) = (81 \times 81) \times (1 \times 48)$ with 5 levels in the multigrid solver ($MN_x \times MN_y = 3 \times 3$).

These figures show that when the surfaces are black, the Q_L solution converges in less than 10 cycles and the cost is around 1WU (10 cycles in the FVM) for the whole range of the medium participation. The FVM has a better convergence rate for the optically thin limit since the directional coupling is very weak in this limit and the solution converges rapidly. The cost and number of cycles of the FVM rises

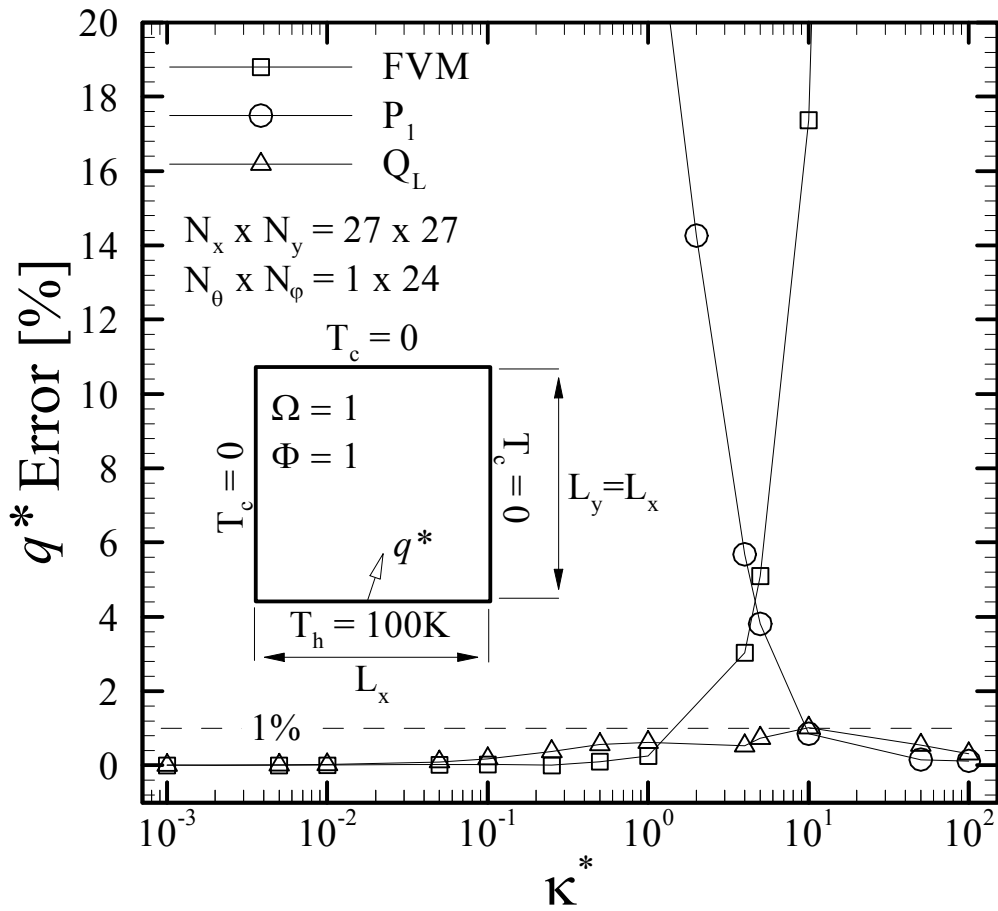


Figure 4.15: Error percentage in the predicted heat transfer at the center of the bottom surface in a purely isotropically scattering medium enclosed in a square enclosure with black surfaces (Case 6).

sharply for $\kappa^* \geq 1$ because of the strong directional coupling and the FVM with the explicit update is practically useless in this limit. It is observed that the Q_L method performs better than the FVM for $\kappa^* > 1$.

The same trends are observed for both methods for partially reflecting surfaces; however, the solution is more expensive and needs more cycles, because of the dependence of the intensities leaving surfaces on the incident intensities due to the reflecting boundaries. Again the Q_L method needs more computational effort for the optically thin media but outperforms the FVM for $\kappa^* > 0.1$.

For both of the black and partially reflecting surfaces, there is a penalty in the performance (cost) of the Q_L method in the optically thin limit, but the solution cost for this limit is small.

To demonstrate the performance of the Q_L method more clearly, Table 4.1 shows the results of Figs.4.16 and 4.17 for some selected optical thicknesses and also for a highly reflective boundary with $\epsilon = 0.1$. The percentage in the parenthesis is the portion of the computational effort (WU) spent to form and solve the Q_L equations. This portion decreases with increasing optical thickness, since for large κ^* , the Q_L equations are more strongly diagonally dominant and therefore, the multigrid solver is more efficient in solving those equations.

Gain is defined as the ratio of the computational cost of the FVM to the computational cost of the Q_L method. Table 4.1 illustrates the very good performance of the Q_L method, and it is observed that the solution cost is almost constant and does not change with κ^* .

The efficacy of the Q_L method is noticeable for the strongly participating media and strongly reflecting boundaries; although as mentioned before, there is a small cost penalty for small κ^* when the surfaces have small reflectivity. However, the computational cost in these cases is small and the largest penalty is 0.4WU, which is equal to only 4 cycles of the FVM according to the definition of the work unit.

Non-Participating Media Before leaving this test case, it should be recalled that the Q_L method does not work for $\kappa^* = 0$, since re-arranging the RTE used to derive the equation for \mathbf{q} gives an indeterminate expression for $\kappa^* = 0$. This issue should be studied carefully since even if $\kappa^* = 0$ happens locally in a region of the solution domain, the Q_L method will diverge. This problem can be overcome by replacing $\kappa^* = 0$ with a very small value that gives accurate results and ensures convergence.

As an example, in this test case for $(N_x \times N_y) \times (N_\theta \times N_\phi) = (27 \times 27) \times (1 \times 24)$, using $\sigma^s = 10^{-6} \text{ m}^{-1}$ ($\kappa^* = 10^{-6}$) in the Q_L method gives exactly the correct q^*

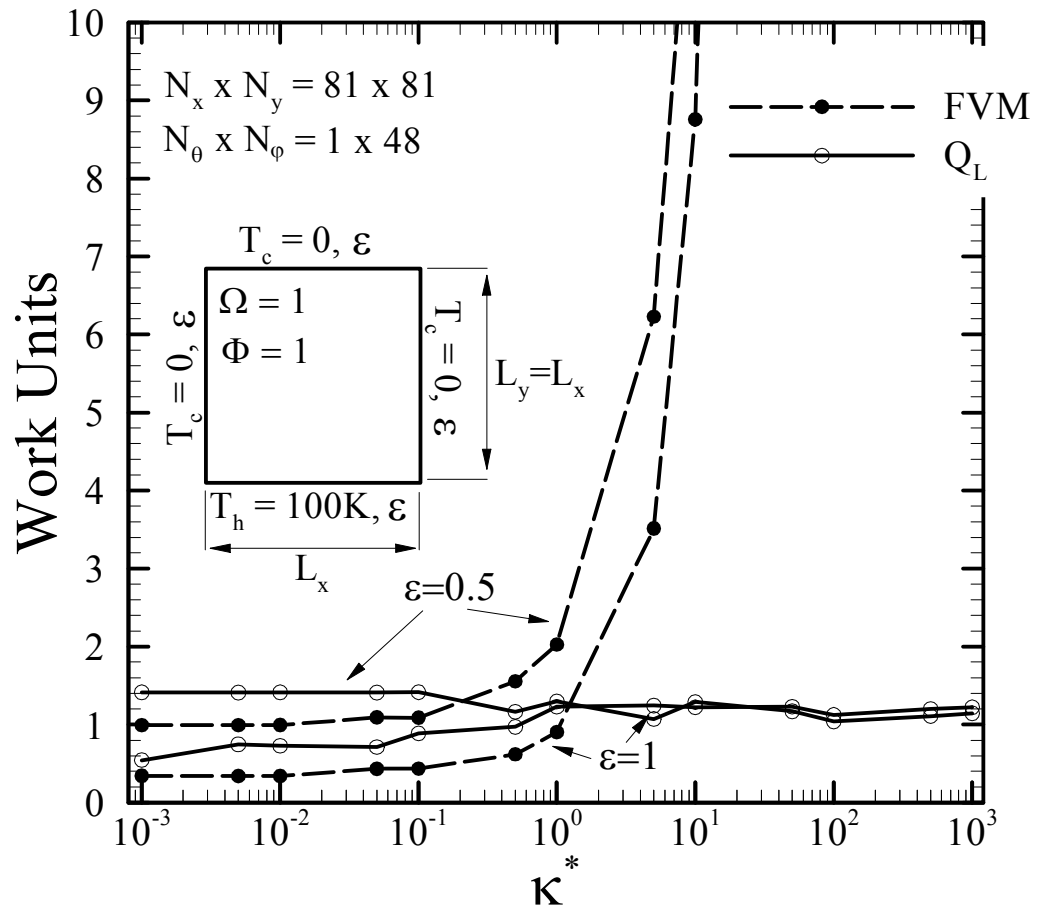


Figure 4.16: Comparison of the solution cost of the FVM and Q_L method applied to a square enclosure with a purely isotropically scattering medium (Case 6).

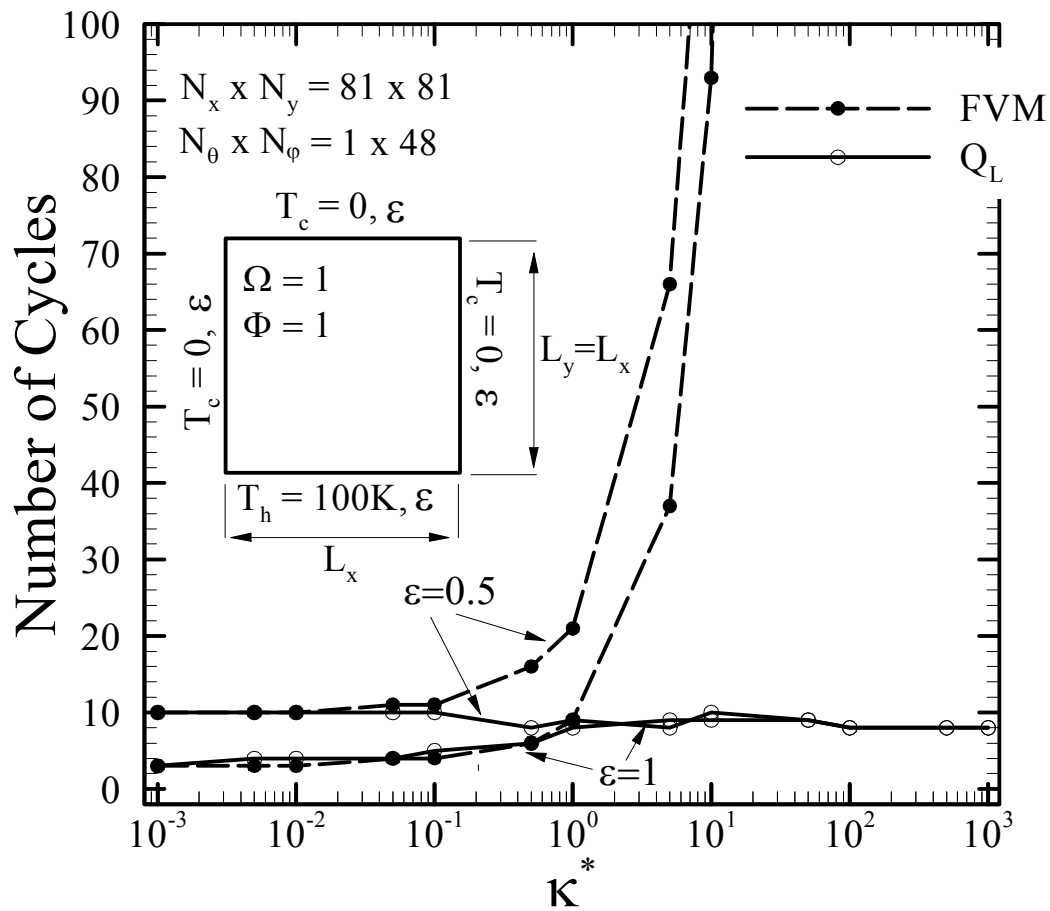


Figure 4.17: Comparison of the number of cycles required to achieve convergence for the FVM and Q_L method applied to a square enclosure with a purely isotropically scattering medium (Case 6).

Table 4.1: Comparison of the solution cost between the Q_L method and FVM applied to a square enclosure with a purely isotropically scattering medium (Case 6).

		FVM		Q_L		Gain
ϵ	κ^*	WU	cycle	WU	cycle	$\frac{\text{WU (FVM)}}{\text{WU (}Q_L\text{)}}$
1.0	0.1	0.5	4	0.9(38%)	5	0.6
	0.5	0.6	6	1.0(32%)	6	0.6
	1.0	0.9	9	1.2(29%)	8	0.8
	5.0	3.5	37	1.2(22%)	9	2.9
	10.0	8.8	93	1.2(20%)	9	7.3
0.5	0.1	1.1	11	1.4(28%)	10	0.8
	0.5	1.6	16	1.2(30%)	8	1.3
	1.0	2.0	21	1.3(29%)	9	1.5
	5.0	6.2	66	1.1(24%)	8	5.6
	10.0	12.9	137	1.3(22%)	10	9.9
0.1	0.1	5.9	62	2.3(25%)	17	2.6
	0.5	8.1	85	2.0(24%)	15	3.9
	1.0	10.7	113	1.8(26%)	13	6.0
	5.0	30.2	320	1.6(24%)	12	18.9
	10	54.0	571	1.5(23%)	11	36.0

along the bottom surface for $\kappa^* = 0$ ($q_{exact}^* = 1$) where the solution converges within 4 cycles and the solution cost is 0.8WU. 53% of the solution cost is spent on the Q_L equations. The FVM solves this problem for $\kappa^* = 0$ with 0.2WU in 2 cycles.

It seems that this remedy, using a very small value instead of 0, is practical and accurate results can be obtained with a reasonable solution cost. However, its application to real problems should be explored.

Case 7: Rectangular Enclosure

In this case, the radiative heat transfer in a tall enclosure ($AR = 10$)⁴ and a wide enclosure ($AR = 1/5$) has been found by the Q_L method and the results are compared with the FVM and exact solutions. All surfaces are black and the purely isotropically scattering medium is gray and in radiative equilibrium. In both cases the optical thickness is unity ($\sigma^s L_y = 1$).

For the enclosure with $AR = 10$, $N_x \times N_y = 9 \times 25$ control volumes with 3 levels in the multigrid solver ($MN_x \times MN_y = 3 \times 5$) have been used for the spatial grid. $N_x \times N_y = 25 \times 9$ control volumes with 3 levels in the multigrid solver ($MN_x \times MN_y = 5 \times 3$) have been employed for the spatial grid in the case that $AR = 1/5$. In both cases, $N_\theta \times N_\phi = 1 \times 24$ solid angles are used for the angular discretization.

Accuracy Figs.4.18 and 4.19 compare q^* on the bottom surface and T^* along the centerline obtained by the Q_L and finite volume methods with the exact solution of Crosbie and Schrenker [54]. For this set of coarse grids, both methods are found to have a very good accuracy for the tall enclosure ($AR = 10$) where the error in the predicted q^* at the center of the bottom surface is 0.3% and 0.7% for the FVM and Q_L method, respectively. In this case, the optical thickness in both of the x and y directions are small ($\kappa_x^* = \sigma^s L_x = \kappa_y^*/10 = 0.1$) so the UDS is accurate. Notice that both methods slightly underestimate T^* near the bottom surface (hot surface) which can be improved by using a finer grid (especially in the y direction).

For the wide enclosure ($AR = 1/5$), the FVM suffers from the inaccuracy of the UDS since in this case, $\kappa_x^* = 5\kappa_y^* = 5$ and the medium is optically dense in the x direction. The maximum error in the prediction of the FVM for q^* at the center of the surface is around 3%. The Q_L method gives very accurate results for this case too, with a maximum error of 0.1%.

⁴Aspect ratio is defined as $AR = L_y/L_x$.

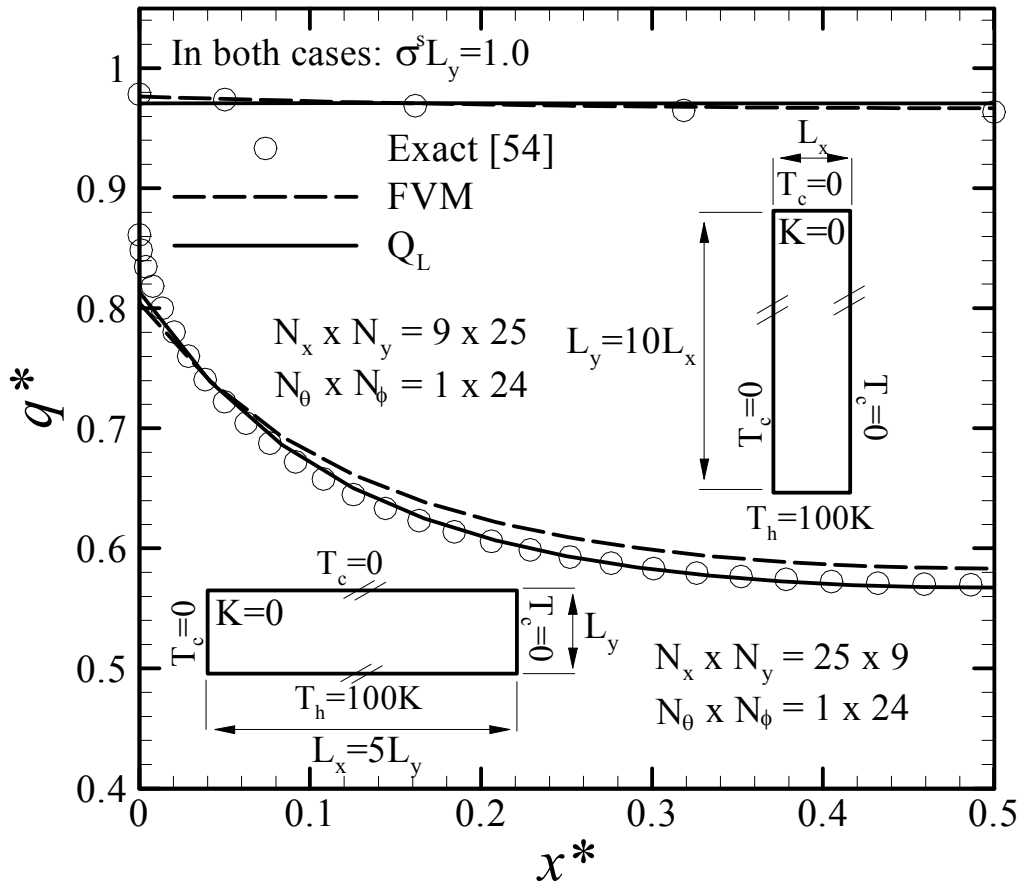


Figure 4.18: Nondimensional heat transfer on the hot bottom surface for a purely isotropically scattering medium with unit optical thickness in rectangular enclosures with black surfaces (Case 7).

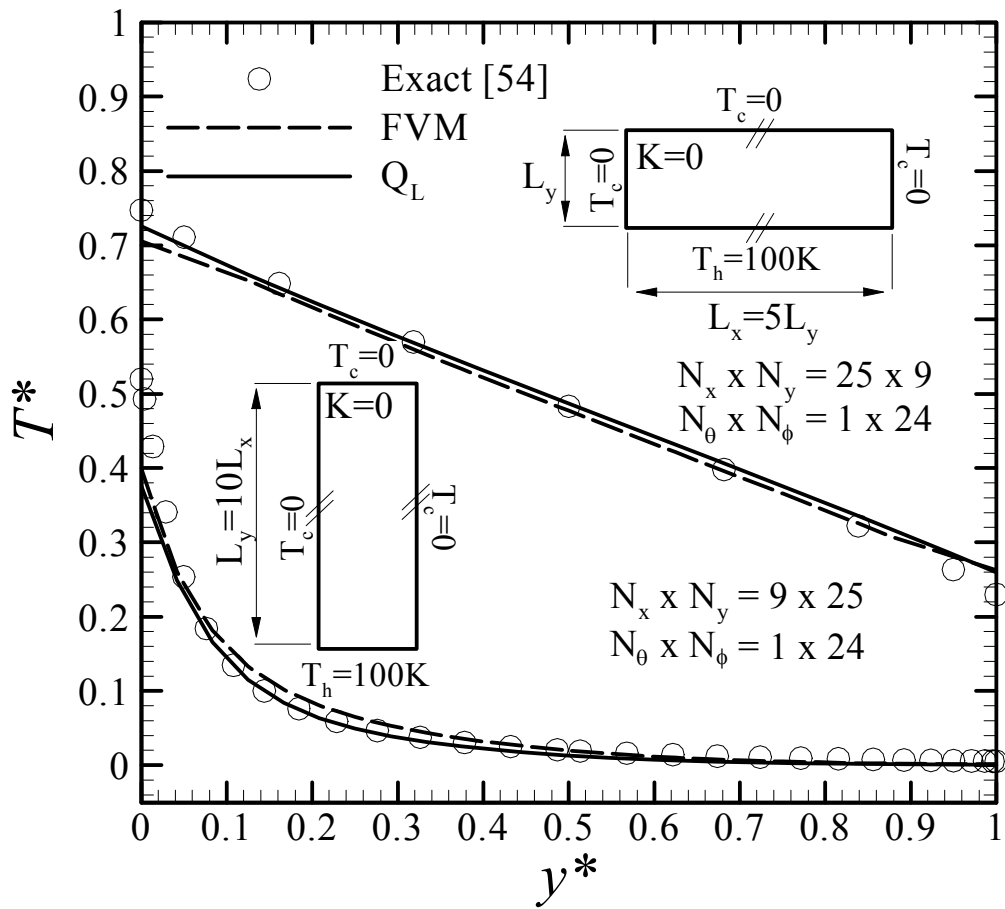


Figure 4.19: Nondimensional temperature along the centerline for a purely isotropically scattering medium with unit optical thickness in rectangular enclosures with black surfaces (Case 7).

Table 4.2: Comparison of the solution cost between the Q_L method and FVM applied to a wide enclosure with a purely isotropically scattering medium (Case 7).

κ^*	FVM		Q_L		Gain
	WU	cycle	WU	cycle	$\frac{\text{WU (FVM)}}{\text{WU (}Q_L\text{)}}$
0.1	0.5	5	1.2(48%)	6	0.4
0.5	0.9	9	1.0(35%)	6	0.9
1.0	1.3	13	1.2(28%)	8	1.1
5.0	6.2	65	1.6(26%)	11	3.9
10.0	15.4	163	1.3(21%)	10	11.8

Cost To study the efficiency of the Q_L method in the rectangular enclosures, the radiative heat transfer in a wide enclosure with $AR = 1/10$ has been solved by the Q_L method and FVM, and the work units and number of cycles have been reported in Table 4.2. This aspect ratio has been chosen since its convergence rate is worse than the problems with $AR = 10$ or $1/5$. A set of fine grids $(N_x \times N_y) \times (N_\theta \times N_\phi) = (125 \times 27) \times (1 \times 48)$ has been used for the spatial and angular grids with 4 levels in the multigrid solver ($MN_x \times MN_y = 5 \times 3$).

These results show the advantage of the Q_L method over the FVM and the enormous reduction in the solution cost for the optically thick limit. The cost penalty in the optically thin limit is a little larger than before (0.7WU), mainly because of the larger portion of the cost spent on solving the I_a equations with the multigrid solver ($\approx 48\%$). This is probably caused by the small aspect ratios of the coarse-mesh blocks.

4.2.2 Absorbing-Scattering Medium

In this case, the radiative heat transfer in an absorbing-scattering but not emitting medium, enclosed in a square enclosure with black surfaces has been solved by the Q_L method for the isotropic and anisotropic scattering. The bottom surface is hot $T_h = 100$ K and the other surfaces are cold $T_c = 0$ K.

Case 8: Absorbing-Isotropically Scattering Medium

Fig.4.20 shows the nondimensional heat transfer on the hot bottom surface predicted by the Q_L and finite volume methods and compares it with the exact solution for $\Omega = 0.5$ and 0.9 where $\kappa^* = 1$. The spatial grid is $N_x \times N_y = 27 \times 27$

Table 4.3: Comparison of the solution cost between the Q_L method and FVM applied to a square enclosure with black surfaces containing an absorbing-isotropically scattering medium with $\Omega = 0.5$ (Case 8).

κ^*	FVM		Q_L		Gain
	WU	cycle	WU	cycle	$\frac{\text{WU (FVM)}}{\text{WU (}Q_L\text{)}}$
0.1	0.4	4	0.7(37%)	4	0.6
0.5	0.5	5	1.0(33%)	6	0.5
1.0	0.6	6	0.8(29%)	5	0.7
5.0	0.8	8	0.8(20%)	6	1
10.0	0.8	8	0.7(18%)	5	1.1

with 4 levels in the multigrid solver ($MN_x \times MN_y = 3 \times 3$). The angular grid is $N_\theta \times N_\phi = 1 \times 24$.

Accuracy Both methods give very accurate results for the given grid. The error in the prediction of q^* at the center of the bottom surface for $\Omega = 0.5$ is 0.06% and 0.2% for the FVM and Q_L method, respectively. This error for $\Omega = 0.9$ is around 0.1% and 0.8% for the FVM and Q_L method, respectively. In this case, the FVM has a very good accuracy since the optical thickness is not large so the UDS is accurate.

Cost Table 4.3 presents the number of cycles and work units required to solve this problem for $\Omega = 0.5$ and $0.1 \leq \kappa^* \leq 10$. The spatial and angular grids are $N_x \times N_y = 81 \times 81$ and $N_\theta \times N_\phi = 1 \times 48$ respectively, where 5 levels have been used in the multigrid solver ($MN_x \times MN_y = 3 \times 3$).

Trends in these results are nearly similar to the previous ones; for $\kappa^* > 5$, the Q_L method needs less computational effort and there is a negligible cost penalty for the small optical thicknesses. However, the solution in this case, even with the explicit update in the FVM, is inexpensive because of the existence of absorption, and the FVM converges within a small number of cycles even for the large optical thicknesses and therefore, the gain is around 1.

Case 9: Absorbing-Anisotropically Scattering Medium

The problem and the spatial grid in this case are the same as Case 8 except that here the scattering is anisotropic with a linear phase function and the angular grid

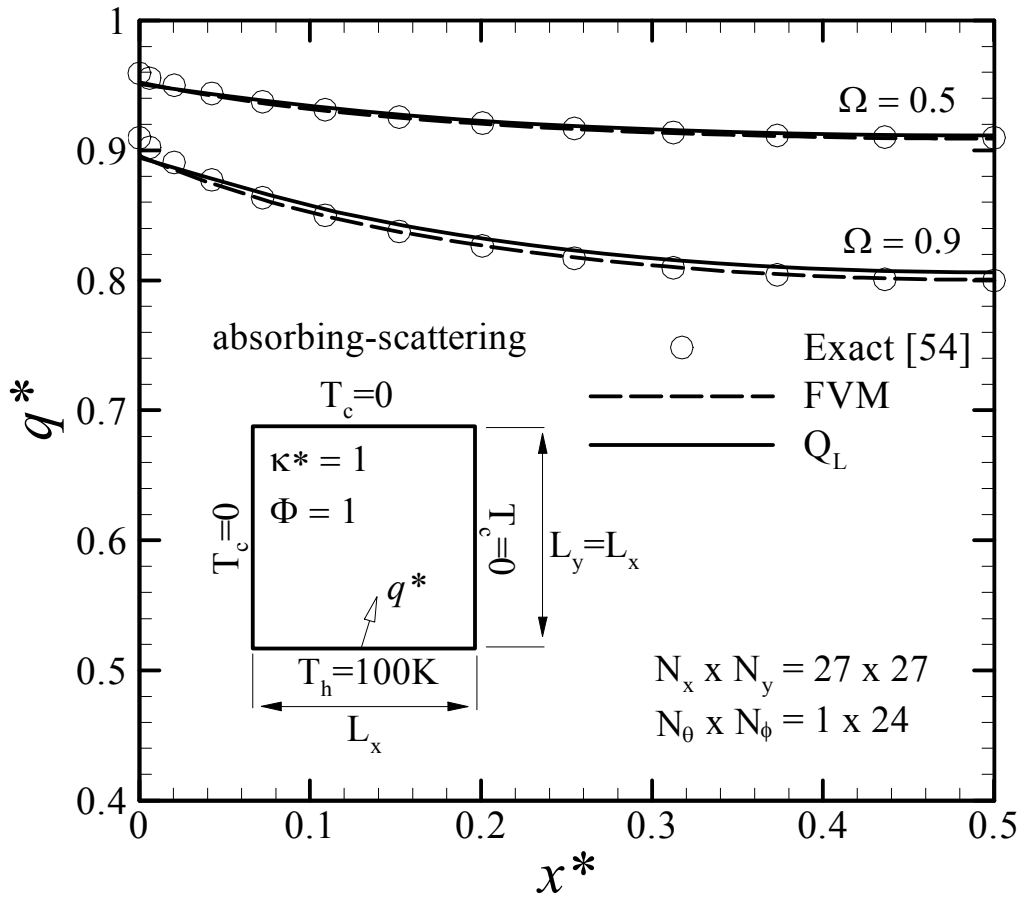


Figure 4.20: Nondimensional heat transfer on the hot bottom surface for an absorbing-isotropically scattering medium enclosed in a square enclosure with black surfaces (Case 8).

is relatively finer ($N_\theta \times N_\phi = 4 \times 24$). The exact solution is obtained from [55].

Fig.4.21 depicts the q^* distribution predicted by the Q_L method and FVM, and compares them with the exact solution. It is seen that for this set of coarse grids, both of the Q_L and FVM results are in an acceptable agreement with the exact solution, the maximum error for q^* at the center of the surface in the worst case is less than 1%; however, a finer spatial and angular grids is required to obtain more accurate results, especially for strong scattering ($\Omega = 0.95$).

4.2.3 Pure Anisotropic Scattering

The accuracy of the Q_L method in predicting the radiative heat transfer for anisotropic scattering was studied before (Cases 3, 4, and 9) where the results were in a very good agreement with the exact solutions for the tested coarse grids. In this section, the attention is focused on the solution cost and convergence rate of the Q_L method for complex phase functions.

Table 4.4 compares the computational cost and number of cycles required by the Q_L method and FVM applied to a square enclosure with black surfaces enclosing a medium which scatters anisotropically with a linear phase function: $\Phi = 1 - \cos(\Psi)$. The medium does not absorb or emit.

$N_x \times N_y = 81 \times 81$ control volumes and $N_\theta \times N_\phi = 2 \times 48$ solid angles have been used to solve this problem with 5 levels in the multigrid solver ($MN_x \times MN_y = 3 \times 3$).

This table shows the advantage of the Q_L method for $\kappa^* > 1$ where the gain in the computational cost rises sharply with increasing the participation of the medium. For $\kappa^* = 10$, the difference in work units required by the Q_L and finite volume methods is around 8WU, which is equal to 80 cycles in the FVM.

Case 10: Complex Phase Functions

To further study the performance of the Q_L method, the method is applied to solve problems with more complex phase functions for a wide range of optical thicknesses. The selected phase functions are the non-linear and Delta-Eddington scattering phase functions.

The non-linear phase function is

$$\Phi(\mathbf{s}', \mathbf{s}) = 1 + a_1 \cos(\Psi) + a_2(3 \cos^2(\Psi) - 1)$$

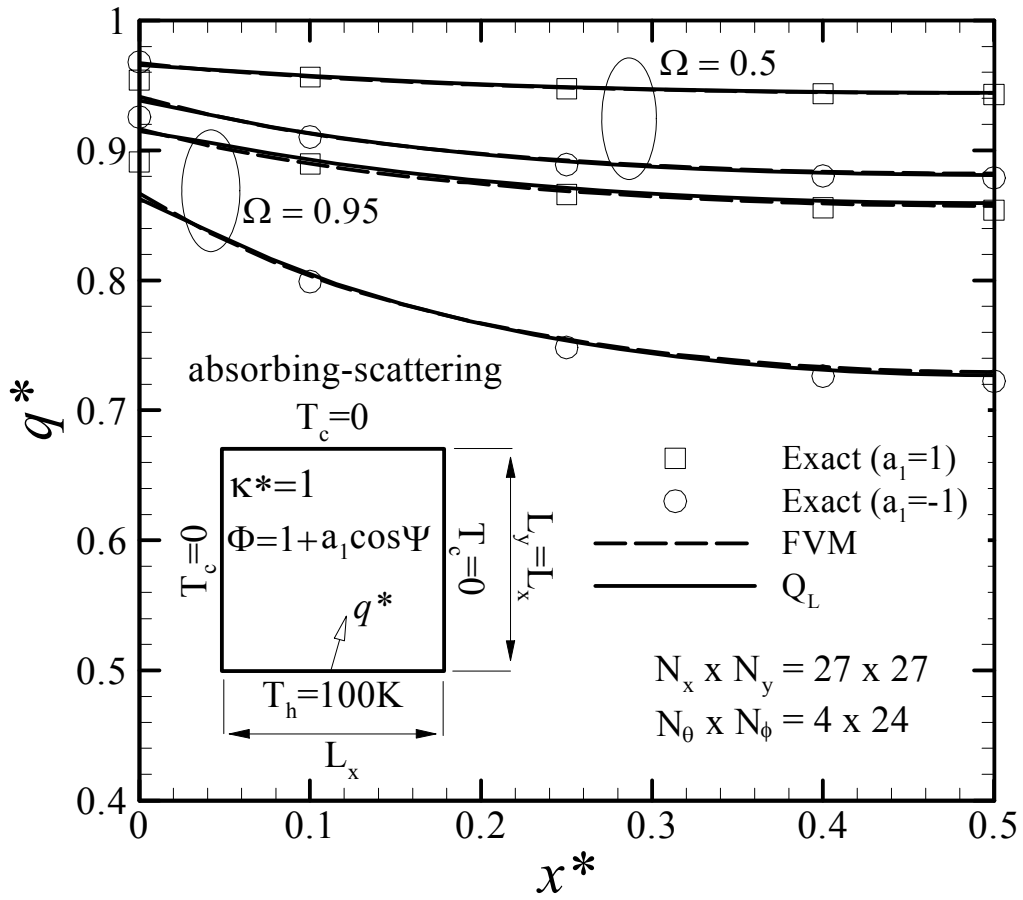


Figure 4.21: Nondimensional heat transfer on the hot bottom surface for an absorbing-anisotropically scattering medium enclosed in a square enclosure with black surfaces (Case 9).

Table 4.4: Comparison of the solution cost between the Q_L method and FVM applied to a square enclosure enclosing an anisotropically scattering medium with a linear phase function $\Phi = 1 - \cos(\Psi)$.

κ^*	FVM		Q_L		Gain
	WU	cycle	WU	cycle	$\frac{\text{WU (FVM)}}{\text{WU (}Q_L\text{)}}$
0.1	0.4	4	0.7(16%)	5	0.6
0.5	0.6	6	1.0(13%)	8	0.6
1.0	0.9	9	1.3(12%)	10	0.7
5.0	3.9	41	1.6(11%)	13	2.4
10.0	10.1	107	1.7(10%)	14	6.0

and the Delta-Eddington phase function is

$$\Phi(\mathbf{s}', \mathbf{s}) = 2f\delta(1 - \cos(\Psi)) + (1 - f)(1 + 3g \cos(\Psi))$$

where $a_1 = 1.5$, $a_2 = 0.25$, $f = 0.5$, and $g = 0.3$ have been used in this research.

The purely anisotropically scattering medium is enclosed in a square enclosure with black surfaces. The spatial grid is $N_x \times N_y = 81 \times 81$ with 5 levels in the multigrid solver ($MN_x \times MN_y = 3 \times 3$), and the angular grid is $N_\theta \times N_\phi = 2 \times 48$.

Figs.4.22 and 4.23 compare the solution cost and number of cycles for the Q_L method and FVM for these two phase functions. As before, there is a small penalty in solution cost for the small optical thicknesses and then the Q_L method surpasses the FVM which is very expensive for the optically thick media.

Comparing these figures with Figs.4.16 and 4.17 shows that there is a difference between the trends in the optically thick media. Whereas the number of cycles and cost in Case 1 (isotropic scattering) do not change significantly in the optically thick limit and are almost constant, the number of cycles and cost rise with increasing κ^* when the scattering is anisotropic.

This behavior was observed and discussed before by Chui and Raithby [39] for the multiplicative acceleration scheme. Since the Q_L method and the multiplicative scheme are common in solving for I_a and using the phase weight concept, this behavior was expected for the Q_L method too. The reason of this behavior is that the isotropic scattering does not contribute to the net radiant flux through the control volume faces and therefore, drops out of the Q_L equation (see Eq.(2.13)). But the anisotropic scattering participates in the Q_L equations (through Eq.(2.16)) and causes a strong directional dependence in the coefficients of the Q_L method which deteriorates the convergence rate.

Even though the effectiveness of the Q_L method is affected adversely by the anisotropic scattering, the Q_L method is still much more efficient than the FVM which is completely useless for the strongly participating media.

4.2.4 Isothermal Absorbing-Emitting Medium

The radiative heat transfer in an isothermal slab was solved in Case 5 and it was mentioned that solving this problem is very inexpensive since intensities in different directions are decoupled. However, obtaining accurate results for this problem, especially in 2D, is difficult because of the ray effect, the exponential variation of intensity near the surfaces, and the discontinuity in the intensity field at the surfaces. In fact, there is a very sharp variation of intensities with an exponential nature near the surfaces for large optical thicknesses which is difficult to capture.

In Case 11, the Q_L method has been applied to a 2D isothermal absorbing-emitting medium enclosed in a square enclosure with cold black surfaces. The medium is kept at $T_G = 100$ K and q^* for this problem is defined as $q^* = q/\sigma T_G^4$.

$N_x \times N_y = 27 \times 27$ control volumes and $N_\theta \times N_\phi = 1 \times 24$ solid angles have been used to solve this problem with 4 levels in the multigrid solver ($MN_x \times MN_y = 3 \times 3$).

The exact heat flux on each point of the bottom surface is obtained by integrating the RTE analytically from the upstream surface to the desired point for a given direction and then numerically integrating the intensities in that point over all directions to find the flux.

Nondimensional heat transfer onto the bottom surface for the weakly and strongly emitting media ($K = 0.1$ and 10) is presented in Fig.4.24. The results for the weakly emitting media ($K = 0.1$) are in a very good agreement with the exact solution and the maximum error is about 1.5% for this set of coarse grids. In the strongly emitting medium, the Q_L method has a very poor accuracy and the error is around 7%. The reason of this inaccuracy is the sharp variation of intensities with an exponential nature near the surfaces which can not be resolved by the current spatial grid.

To overcome this problem, the grid should be clustered near the surfaces to have a finer mesh in the region of sharp variations. To cluster the grid near the top and bottom surfaces, an exponential expression has been used [56]:

$$y = L_y \frac{(1 + \beta) \left(\frac{\beta+1}{\beta-1} \right)^{2\eta-1} + (1 - \beta)}{2 \left[\left(\frac{\beta+1}{\beta-1} \right)^{2\eta-1} + 1 \right]}$$

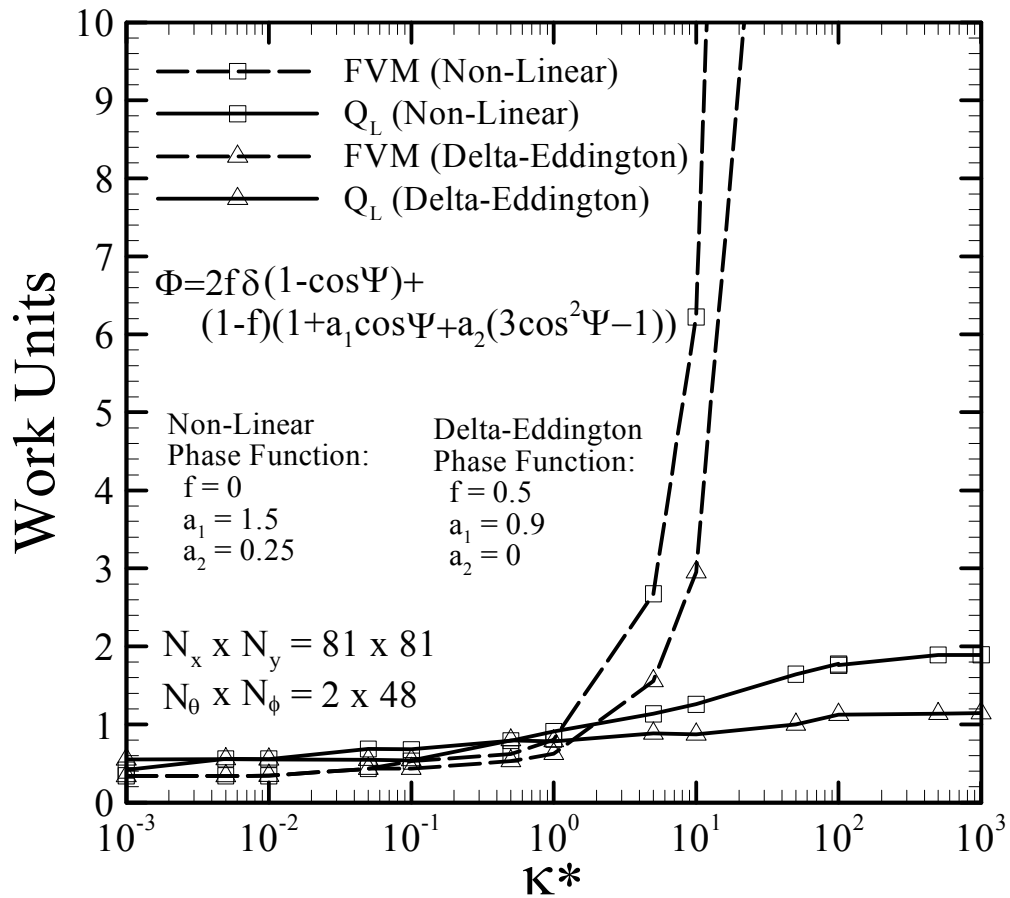


Figure 4.22: Comparison of the solution cost of the FVM and Q_L method applied to a purely anisotropically scattering medium enclosed in a square enclosure with black surfaces (Case 10).

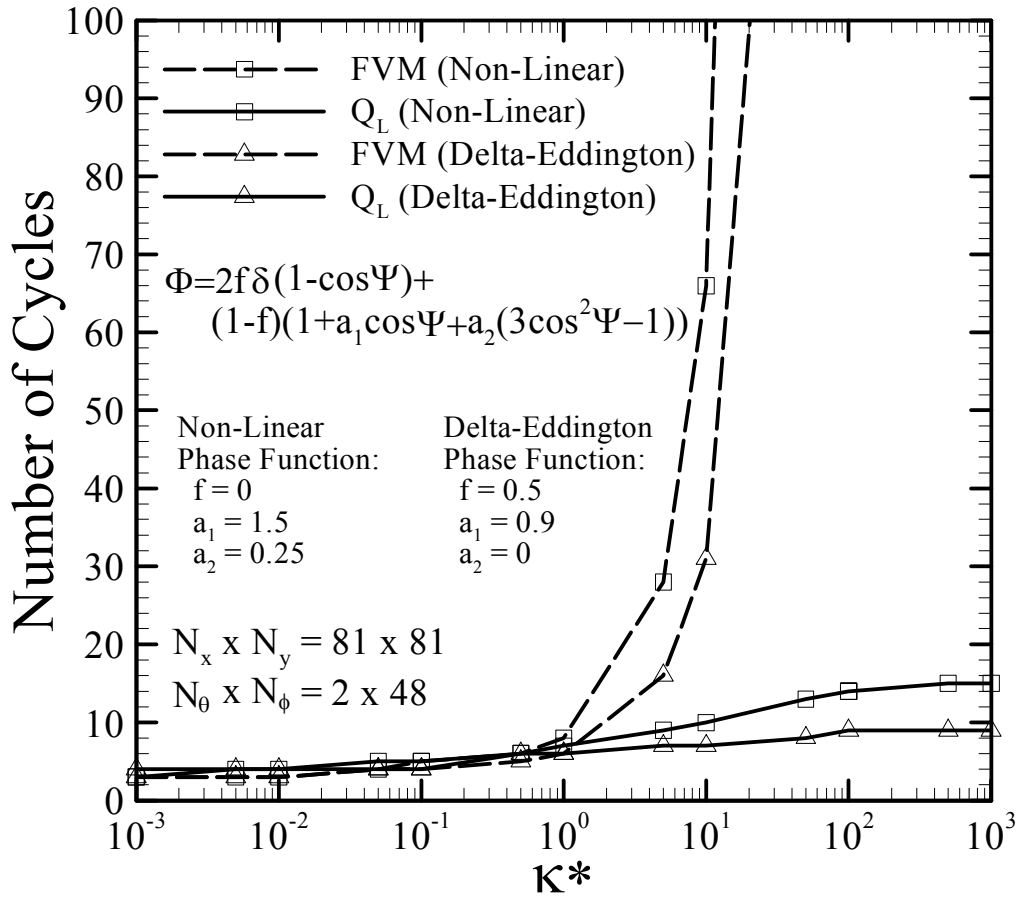


Figure 4.23: Comparison of the number of cycles required to achieve convergence for the FVM and Q_L method applied to an purely anisotropically scattering medium enclosed in a square enclosure with black surfaces (Case 10).

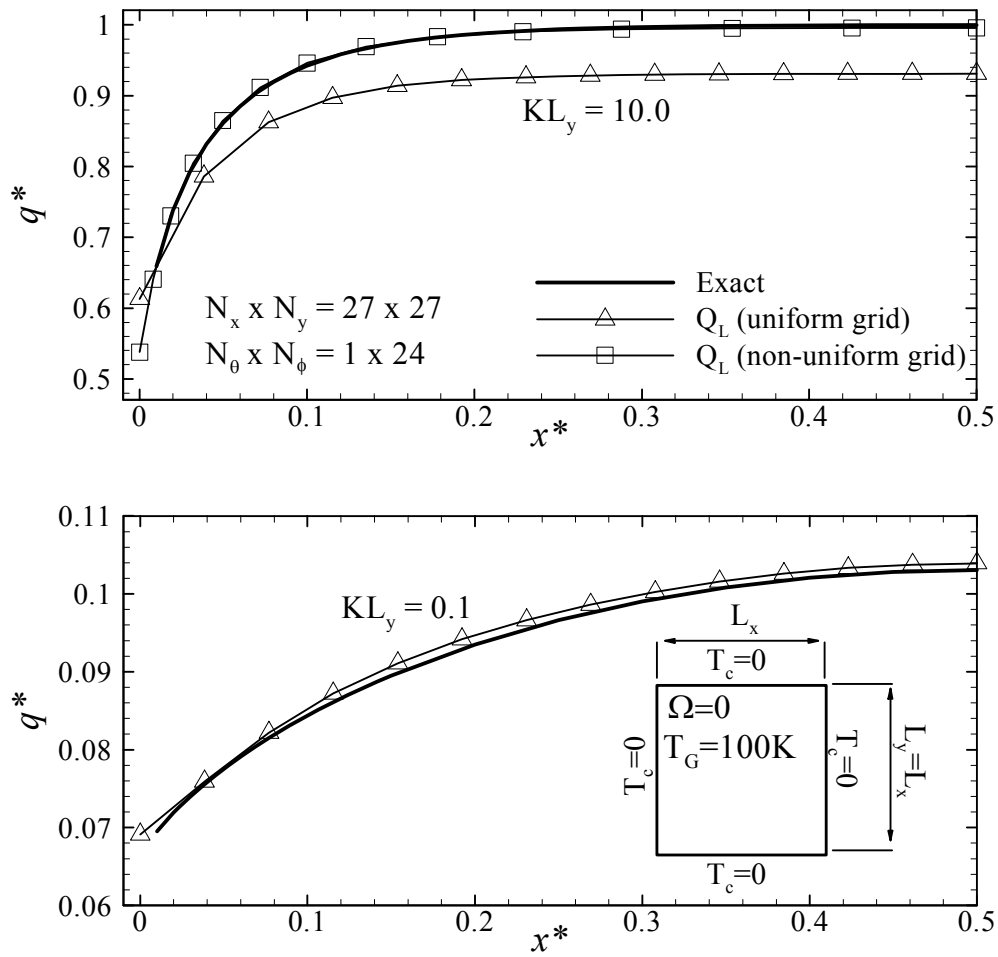


Figure 4.24: Nondimensional heat transfer on the bottom surface of a square enclosure with cold black surfaces enclosing an isothermal absorbing-emitting medium (Case 11).

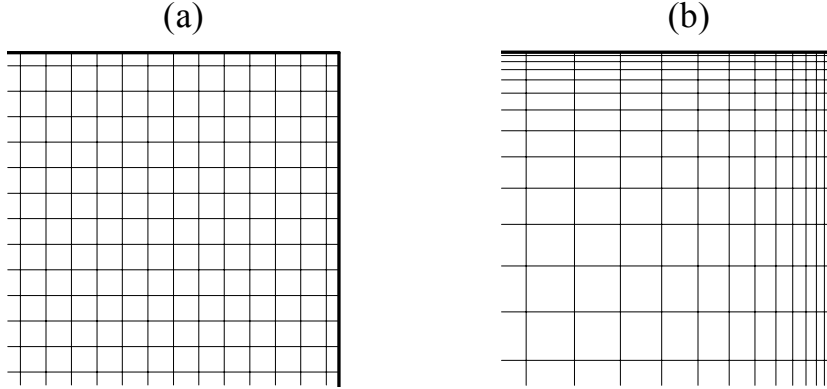


Figure 4.25: Control volumes in uniform (a) and non-uniform (b) grids in a square enclosure.

where $1 < \beta < \infty$ is a control parameter and as β gets closer to 1, the grid becomes finer near the top and bottom surfaces. $\beta = 1.05$ is used in this research. η is defined as $\eta = (j - 1)/(N_y - 1)$ where $1 \leq j \leq N_y$ is the computational node index in the y direction. The same expression has been used to cluster the grid near the left and right surfaces. Fig.4.25 shows the top-right quarter of the square enclosure with the uniform and non-uniform ($\beta = 1.05$) grids.

The non-uniform mesh with the same number of control volumes and solid angles as before has been used to solve this problem for the strongly emitting medium again. Fig.4.24 depicts that using a finer grid near the surfaces can resolve the sharp variations in this region and improve the accuracy dramatically.

4.2.5 Robustness

Up to this point, it has been shown that the Q_L method is able to efficiently predict the radiative heat transfer in different kind of problems with a very good accuracy for the tested coarse grids. Another issue that should be considered is robustness.

To study the robustness of the Q_L method, the methodology used in the literature [41, 42] for the multiplicative method (the mesh rebalance method) is employed here and the Q_L method is applied to a wide range of grid sizes and cell optical thicknesses. The cell optical thickness is defined as $\kappa\Delta$ where Δ is a length scale of the grid where here $\Delta = L_x/(N_x - 1)$ (width of the interior control volumes) is used.

Table 4.5: The solution cost and number of cycles required by the Q_L method applied to a square enclosure with black surfaces enclosing a purely isotropically scattering medium to study the robustness of the Q_L method.

$\sigma^s \Delta$	$N_x \times N_y$				
	4×4	8×8	32×32	64×64	128×128
0.001	3 [0.4](0%)	3 [0.4](19%)	4 [0.6](28%)	4 [0.7](33%)	5 [1.0](43%)
0.01	4 [0.5](0%)	4 [0.6](27%)	5 [0.7](25%)	6 [1.0](30%)	8 [1.2](32%)
0.05	5 [0.5](0%)	5 [0.6](24%)	8 [1.1](21%)	8 [1.1](22%)	9 [1.3](24%)
0.1	5 [0.6](0%)	7 [1.0](27%)	9 [1.2](21%)	9 [1.2](21%)	10 [1.4](23%)
0.5	7 [0.8](0%)	9 [1.1](21%)	10 [1.4](20%)	10 [1.4](20%)	10 [1.4](23%)
1	8 [1.0](0%)	8 [1.1](24%)	9 [1.2](20%)	9 [1.2](21%)	9 [1.3](26%)
5	7 [0.9](0%)	7 [1.0](23%)	8 [1.1](18%)	8 [1.2](24%)	8 [1.2](31%)
10	7 [0.9](0%)	8 [1.0](18%)	8 [1.1](19%)	8 [1.2](24%)	8 [1.3](32%)
100	7 [0.6](0%)	8 [1.0](14%)	8 [1.1](21%)	8 [1.2](26%)	8 [1.3](35%)

The solved problem is the same as Case 6. The medium is purely isotropically scattering ($\kappa = \sigma^s$) and the enclosure is square and the surfaces are black. The bottom surface is hot $T_B = T_h = 100$ K and the other three surfaces are cold $T_c = 0$ K. $N_\theta \times N_\phi = 1 \times 48$ solid angles have been used in the angular grid. Coarse-mesh blocks are $MN_x \times MN_y = 2 \times 2$.

Table 4.5 presents the number of cycles, work units (in the square brackets), and the portion of the solution cost spent to form and solve the Q_L equations (in the parenthesis). These results illustrate the stability of the Q_L method for the range of very coarse to very fine grids and for a wide range of cell optical thicknesses (and optical thicknesses). The computational cost which is added because of solving the Q_L equations is around 20% – 25% except for very small optical thicknesses where solving the I_a equations is costly due to the lack of diagonal dominance.

Chapter 5

A New Differencing Scheme

A new differencing scheme for the RTE, which calculates the radiant heat flux at the integration points in the same way as the Q_L method, is introduced in this chapter. This scheme is second-order accurate and gives elliptic-type equations for the directional intensities.

This new scheme is applied to the FVM and the equations are derived in this chapter. Then several 2D benchmark problems are solved to study its performance.

5.1 Review of the Existing Differencing Schemes

During the past decades, many researchers have attempted to develop an appropriate spatial differencing scheme to discretize the RTE. The spatial discretization error takes the form of numerical smearing and dispersion. The numerical smearing (false scattering) is a result of the truncation error and is caused by low-order schemes like the first-order UDS, or schemes where the interpolation line and the centerline of the solid angle are not aligned [57]. The numerical dispersion causes nonphysical under- and over-shoots and results from unbounded discretization methods. Since intensity is a positive quantity by definition, these under-shoots may result in negative intensities which are physically unrealistic and can cause numerical instabilities. Researchers have tried to prevent negative intensities by various ways including the negative intensity fix-up procedure [9], positive scheme [58], variable weight scheme [59], and positive intensities criteria [60].

Eliminating both of the numerical smearing and dispersion errors simultaneously is difficult since they are inversely related; to reduce the smearing, a higher-order

scheme or a finer spatial mesh is required where the former usually introduces dispersion and the latter increases the computational cost and memory. The dispersion can be diminished by using a lower-order scheme which produces numerical smearing.

Chai *et al.* [61] studied a number of common differencing schemes including the positive scheme [58], step scheme (UDS) [62], and diamond scheme [62], and concluded that a more accurate scheme is still required. Raithby and Chui [15] and Chai *et al.* [63] modified the exponential scheme, and Jessee and Fiveland [57] considered four bounded high-resolution differencing schemes: MINMOD, MUSCL, CLAM, and SMART.

Along with these attempts to propose more accurate and stable differencing schemes for the RTE, several researchers [64, 34, 65] have tried to formulate the RTE in the even parity form. The even parity form of the RTE is derived by considering opposite directions \mathbf{s} and $-\mathbf{s}$, and by defining the following quantities:

$$\begin{aligned} F(\mathbf{r}, \mathbf{s}) &= \frac{1}{2} [I(\mathbf{r}, \mathbf{s}) + I(\mathbf{r}, -\mathbf{s})] \\ G(\mathbf{r}, \mathbf{s}) &= \frac{1}{2} [I(\mathbf{r}, \mathbf{s}) - I(\mathbf{r}, -\mathbf{s})] \end{aligned}$$

Adding and subtracting the RTE written for \mathbf{s} and $-\mathbf{s}$ results in two equations for $F(\mathbf{r}, \mathbf{s})$ and $G(\mathbf{r}, \mathbf{s})$ where eliminating $G(\mathbf{r}, \mathbf{s})$ from these two equations gives a second-order form of the RTE. This second-order form is called the even parity equation [4].

The even parity equation has the advantages of second-order accuracy and being positive definite and self-adjoint [66]. Also since the second-order even parity equation does not have the one-way characteristics of the first-order conventional RTE, the standard spatial discretization schemes (e.g the central differencing scheme) and efficient linear equations solvers (e.g. the multigrid solver) can be applied to solve the equations.

However, studies showed that the accuracy of the even parity equation degrades with increasing optical thickness and the surface emissivity. Also solving the even parity equation is more expensive than solving the conventional RTE. Therefore, the even parity formulation has been abandoned in favor of the conventional RTE.

In the following section, a new second-order differencing scheme is proposed, based on re-arranging the RTE in the same way as the Q_L equations were derived in Chapter 2.

5.2 Mathematical Formulation

The RTE was discretized in Chapter 1 with the finite volume method which finally resulted in (Eq.(1.9))

$$\sum_{ip=1}^{N_{ip}} Q_{ip}^l = [-(K_P + \sigma_P^s)I_P^l + K_P I_{b,P} + \sigma^s \bar{I}_P^l] V_P \omega^l \quad (5.1)$$

for the control volume V_P with N_{ip} panels (Fig.1.2) where

$$Q_{ip}^l = A_{s,ip} \int_{\omega^l} I_{ip}(\mathbf{s} \cdot \mathbf{n}_{ip}) d\omega = A_{s,ip} \mathbf{q}_{ip}^l \cdot \mathbf{n}_{ip} \quad (5.2)$$

is the radiative heat transfer rate through panel ip within ω^l .

As discussed in the first chapter, I_{ip} should be approximated in terms of the nodal values through a differencing scheme. Noticing that \mathbf{q}_{ip}^l in Eq.(5.2) and \mathbf{q}_{ip} in Eq.(2.3) are simply related,

$$\mathbf{q}_{ip} = \sum_L \mathbf{q}_{ip}^l d\omega$$

the same approach used to calculate \mathbf{q}_{ip} can be applied to find \mathbf{q}_{ip}^l .

The I_{ip} intensity in Eq.(5.2) can be calculated by re-arranging the RTE as

$$I(\mathbf{r}, \mathbf{s}) = \frac{-1}{\kappa} \frac{dI}{ds} + (1 - \Omega) I_b(\mathbf{r}) + \Omega \left\{ \frac{1}{4\pi} \int_{4\pi} I(\mathbf{r}, \mathbf{s}') \Phi(\mathbf{s}', \mathbf{s}) d\omega' \right\}$$

Substituting this equation for I into

$$\mathbf{q}_{ip}^l = \int_{\omega^l} I_{ip} \mathbf{s} d\omega$$

and using $dI/ds = \nabla I \cdot \mathbf{s} = \frac{\partial I}{\partial x_j} s_j$ and $\mathbf{s} = s_i \mathbf{e}_i$ yields

$$\mathbf{q}_{ip}^l = -\frac{1}{\kappa} \mathbf{I}_t^l + (1 - \Omega) \mathbf{I}_b^l + \Omega \mathbf{I}_s^l \quad (5.3)$$

where \mathbf{I}_t^l , the directional transport integral, \mathbf{I}_b^l , the directional emitting integral and \mathbf{I}_s^l , the directional scattering integral, are defined as

$$\begin{aligned} \mathbf{I}_t^l &= \left\{ \int_{\omega^l} \frac{\partial I}{\partial x_j} s_j s_i d\omega \right\} \mathbf{e}_i = \frac{\partial I}{\partial x_j} \left\{ \int_{\omega^l} s_j s_i d\omega \right\} \mathbf{e}_i \\ \mathbf{I}_b^l &= I_b \left\{ \int_{\omega^l} s_i d\omega \right\} \mathbf{e}_i \\ \mathbf{I}_s^l &= \left\{ \int_{\omega^l} \left\{ \frac{1}{4\pi} \int_{4\pi} I(\mathbf{r}, \mathbf{s}') \Phi(\mathbf{s}', \mathbf{s}) d\omega' \right\} s_i d\omega \right\} \mathbf{e}_i \end{aligned}$$

For $\omega^l = 4\pi$, $\mathbf{I}_b^l = 0$ and \mathbf{I}_t^l and \mathbf{I}_s^l become the transport and scattering integrals in Eqs.(2.7) and (2.8). Using \mathbf{D}^l and \mathbf{N}^l defined in Chapter 2, the first two integrals are simplified as

$$\begin{aligned}\mathbf{I}_t^l &= \frac{\partial I}{\partial x_j} D_{ij}^l \mathbf{e}_i \\ \mathbf{I}_b^l &= I_b N_i^l \mathbf{e}_i\end{aligned}$$

The scattering integral can be approximated as

$$\mathbf{I}_s^l = \frac{1}{4\pi} \int_{4\pi} I(\mathbf{r}, \mathbf{s}') \left\{ \int_{\omega^l} \Phi(\mathbf{s}', \mathbf{s}) \mathbf{s} d\omega \right\} d\omega' = \left\{ \frac{1}{4\pi} \int_{4\pi} I(\mathbf{r}, \mathbf{s}') \mathbf{J}^{ll'} d\omega' \right\}$$

where

$$\mathbf{J}^{ll'} = \int_{\omega^l} \Phi(l', l) \mathbf{s} d\omega$$

\mathbf{D}^l , \mathbf{N}^l , and $\mathbf{J}^{ll'}$ are calculated by exact or precise numerical integration and stored for each direction and are independent of the spatial location.

Substituting these integrals into Eq.(5.3) and using Eqs.(5.1) and (5.2) gives the final form of the discretized equation:

$$\begin{aligned}\sum_{ip=1}^{N_{ip}} A_{s,ip} \left[-\frac{1}{\kappa} \frac{\partial I}{\partial x_j} D_{ij}^l \mathbf{e}_i + (1 - \Omega) I_b N_i^l \mathbf{e}_i + \frac{\Omega}{4\pi} \int_{4\pi} I' \mathbf{J}^{ll'} d\omega' \right] \cdot \mathbf{n}_{ip} \\ = [-(K_P + \sigma_P^s) I_P^l + K_P I_{b,P} + \sigma^s \bar{I}_P^l] V_P \omega^l\end{aligned}\quad (5.4)$$

The boundary condition for this equation is the same as Eq.(1.11). For a gray-diffuse surface at temperature T_s , the boundary condition for the surface intensity I_s^l which leaves the surface toward the medium, $\mathbf{s}^l \cdot \mathbf{n} < 0$, is

$$\epsilon_s A_s \sigma T_s^4 + (1 - \epsilon_s) \sum_{\mathbf{s}' \cdot \mathbf{n} < 0} Q^{l'} = \sum_{\mathbf{s}' \cdot \mathbf{n} > 0} Q_s^l = A_s \pi I_s^l \quad (5.5)$$

where \mathbf{n} is the unit surface normal pointing out of the medium, ϵ_s is the surface emissivity, and Q^l is the radiative heat transfer rate (Eq.(5.2)).

The left-hand side of Eq.(5.4) is approximated by a linear profile based on the nodal I^l values, in the same way as the Q_L equations (see Chapter 2 and Appendix B). The second and third terms in the right-hand side and the terms resulting from the approximation of the second and third terms in the left-hand side are lagged in the source term. Eq.(5.4) with Eq.(5.5) give a set of linear algebraic equations in the form of

$$a_P I_P^l = \sum_{nb} a_{nb} I_{nb}^l + b_P^l \quad (5.6)$$

5.3 Numerical Solution

The resulting equations (Eq.(5.6)) are elliptic in nature and are efficiently solved by the multigrid solver. For the case that the temperature field is known or not connected to radiation, the solution procedure is:

1. Calculate and store \mathbf{D}^l , \mathbf{N}^l , and $\mathbf{J}^{ll'}$.
2. Initializing the I^l and I_a values (e.g. $10^{-5} \text{ W m}^{-2} \text{ sr}^{-1}$ and W m^{-2}). I_b is calculated from the temperature field, or $I_b = I_a$ if the medium is in radiative equilibrium.
3. The multigrid solver is used in each direction to solve Eq.(5.6) and reduce the scaled maximum residual below the specified target. After finding the new I^l distribution in each direction, the I_a field is updated and the source terms are re-calculated (Gauss-Seidel update).
4. After sweeping through all directions, the scaled maximum residual of Eq.(5.6) in all control volumes and solid angles are checked and the iterative solution is terminated if the convergence criterion is satisfied.

5.4 Results

Several 2D benchmark problems are solved in this section to study the accuracy of the new differencing scheme. The new differencing scheme is used in the FVM which is then referred to as “New Scheme”. Results are compared with the exact solutions and results of the FVM with UDS (referred to as “UDS”) and the \mathbf{Q}_L^{UD} method where the superscript UD shows that the first-order UDS has been used in the FVM to find the α^l distribution for the \mathbf{Q}_L method. Also the second-order New Scheme can be used to provide the α^l distribution for the \mathbf{Q}_L method (which is then called \mathbf{Q}_L^{NS}), but the solution will be the same as the New Scheme solution since the New Scheme and the \mathbf{Q}_L^{NS} have the same discretization error.

The New Scheme is applied to a purely isotopically scattering medium enclosed in square and rectangular enclosures with black or partially reflecting surfaces.

The multigrid solver, computational grid, and convergence criteria¹ used for these problems are the same as before (see Chapter 3).

¹Note that the residuals are calculated for Eq.(5.6).

5.4.1 Square Enclosure

This test case is the same as Case 6 in the previous chapter. A purely isotropically scattering medium or an absorbing-emitting medium in radiative equilibrium is enclosed in a square enclosure with black surfaces. The bottom surface is hot $T_h = 100$ K and the other surfaces are cold $T_c = 0$ K.

The spatial grid is $N_x \times N_y = 27 \times 27$ with 4 levels in the multigrid solver ($MN_x \times MN_y = 3 \times 3$). $N_\theta \times N_\phi = 1 \times 24$ solid angles have been used in the angular discretization.

Fig.5.1 compares the New Scheme results for q^* with the exact solution and results of the UDS and the Q_L^{UD} method for three optical thicknesses: $\kappa^* = 0.25, 1,$ and 10 ; and Figs.5.2, 5.3, and 5.4 show the T^* distribution along the centerline. These comparisons show that the New Scheme is able to predict the radiative heat transfer accurately in both optically thin and thick media for this set of coarse grids whereas the UDS is inaccurate for the dense media, as explained before. However, for $\kappa^* = 0.25$, the T^* distribution predicted by the New Scheme deviates from the exact results near the hot surface while the predicted q^* by this method is in a very good agreement with the exact solution. The reason of this deviation is that although the New Scheme predicts the intensities in the directions closely parallel to the y axis accurately, its prediction for the intensities in the directions nearly parallel to the x axis (which have small contribution to q^*) is inaccurate. Since T^* is proportional to $I_b = I_a$, this inaccuracy adversely affects the T^* distribution.

Fig.5.5 quantifies the error in the predicted q^* at the center of the bottom surface for the UDS, Q_L^{UD} , and New Scheme (Q_L^{NS}), for a wide range of optical thicknesses. Results are reported for $N_x \times N_y = 27 \times 27$ control volumes with 4 levels in the multigrid solver and $N_\theta \times N_\phi = 1 \times 24$ solid angles. This figure depicts that the accuracy of the New Scheme is comparable to the accuracy of the Q_L^{UD} and the maximum error is below 1%.

To study the effect of the surface reflectivity on the accuracy of the New Scheme, the above problem has been solved when all surfaces are partially reflecting. The spatial and angular grids are the same as before. Fig.5.6 compares the results of the New Scheme with a very precise solution (Zone method [67]) and results of the UDS and Q_L^{UD} method. It is observed that the accuracy of the UDS and the New Scheme is comparable to the accuracy of the Q_L^{UD} method for this intermediate optical thickness and this set of coarse grids.

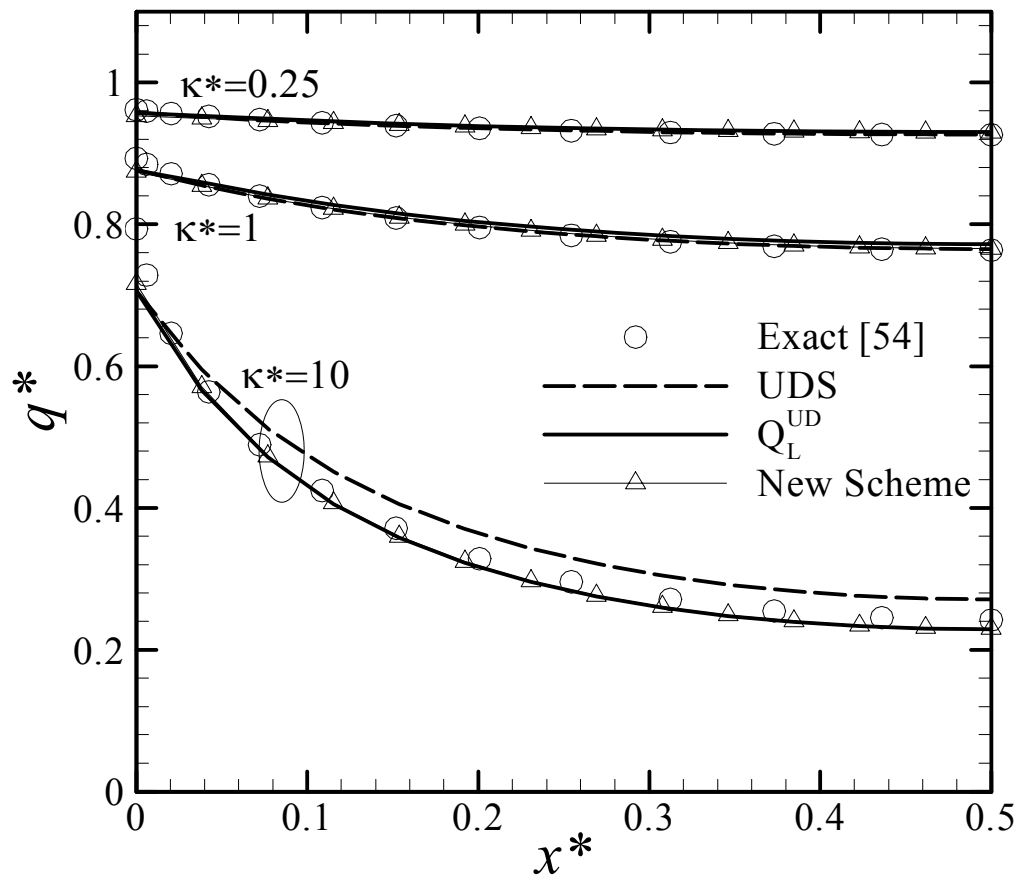


Figure 5.1: Nondimensional heat transfer on the hot bottom surface for a purely isotropically scattering medium enclosed in a square enclosure with black surfaces.

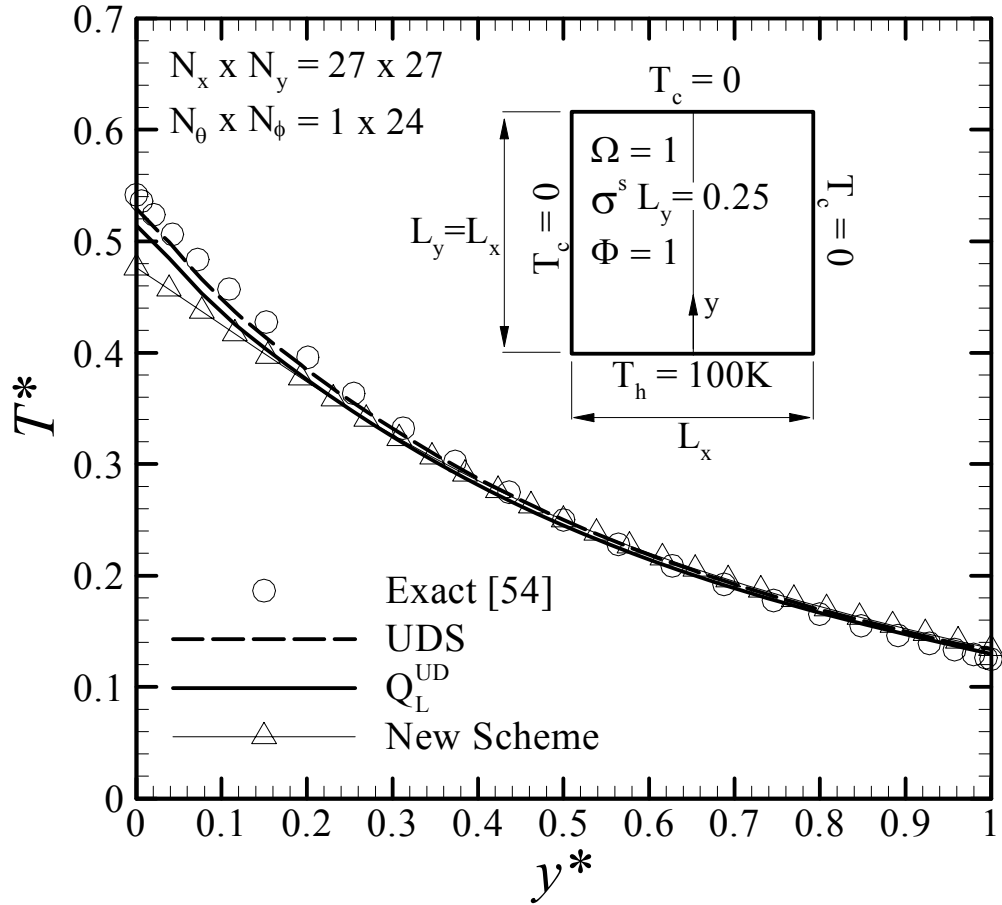


Figure 5.2: Nondimensional temperature along the centerline for a purely isotropically scattering medium enclosed in a square enclosure with black surfaces for $\kappa^* = 0.25$.

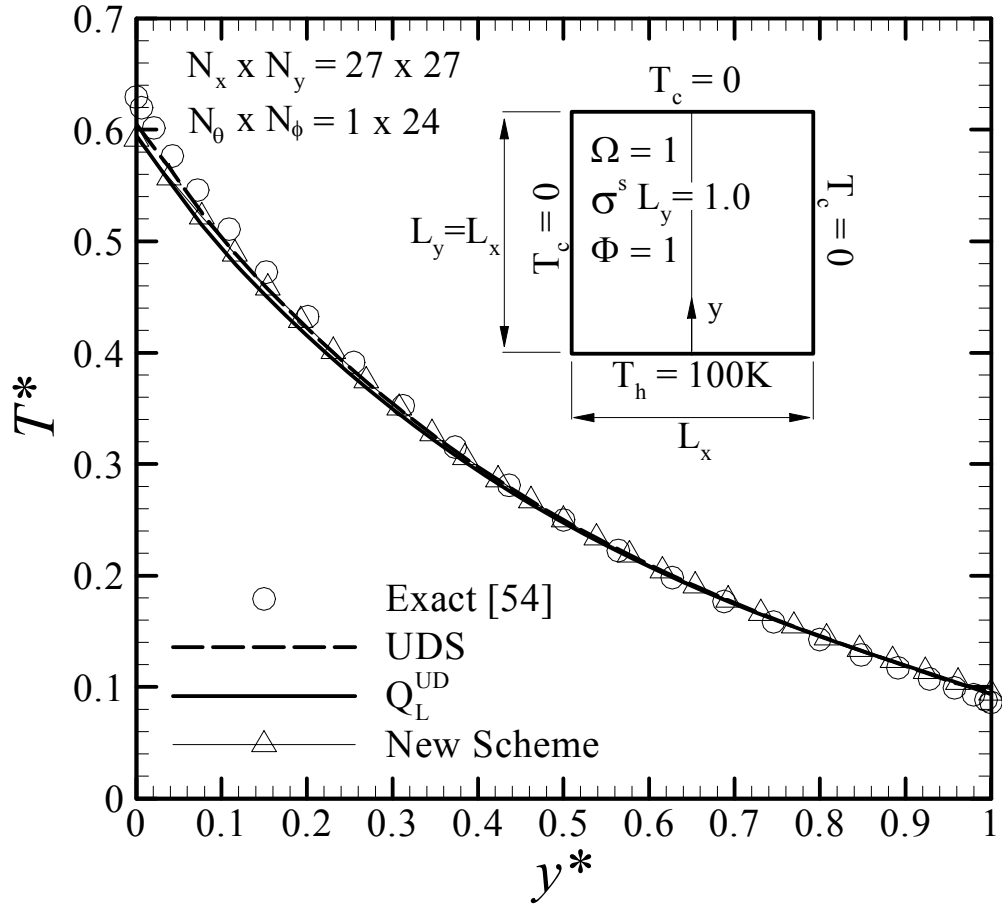


Figure 5.3: Nondimensional temperature along the centerline for a purely isotropically scattering medium enclosed in a square enclosure with black surfaces for $\kappa^* = 1$.

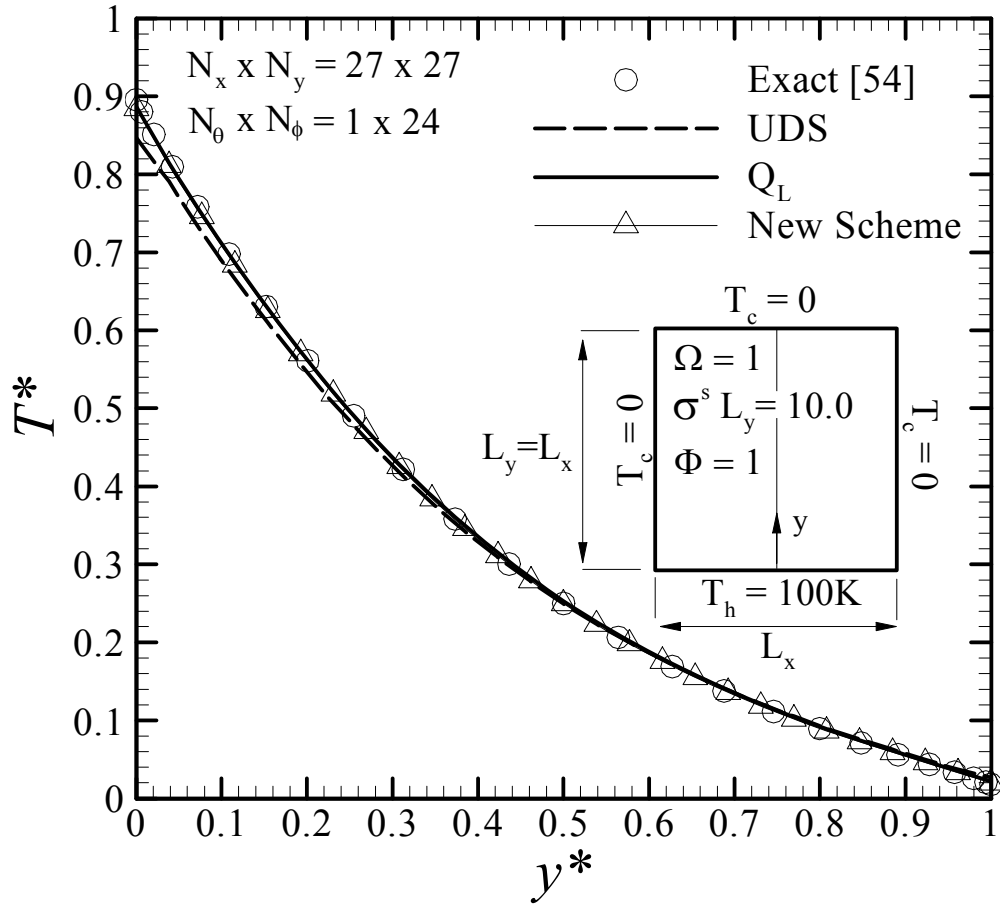


Figure 5.4: Nondimensional temperature along the centerline for a purely isotropically scattering medium enclosed in a square enclosure with black surfaces for $\kappa^* = 10$.

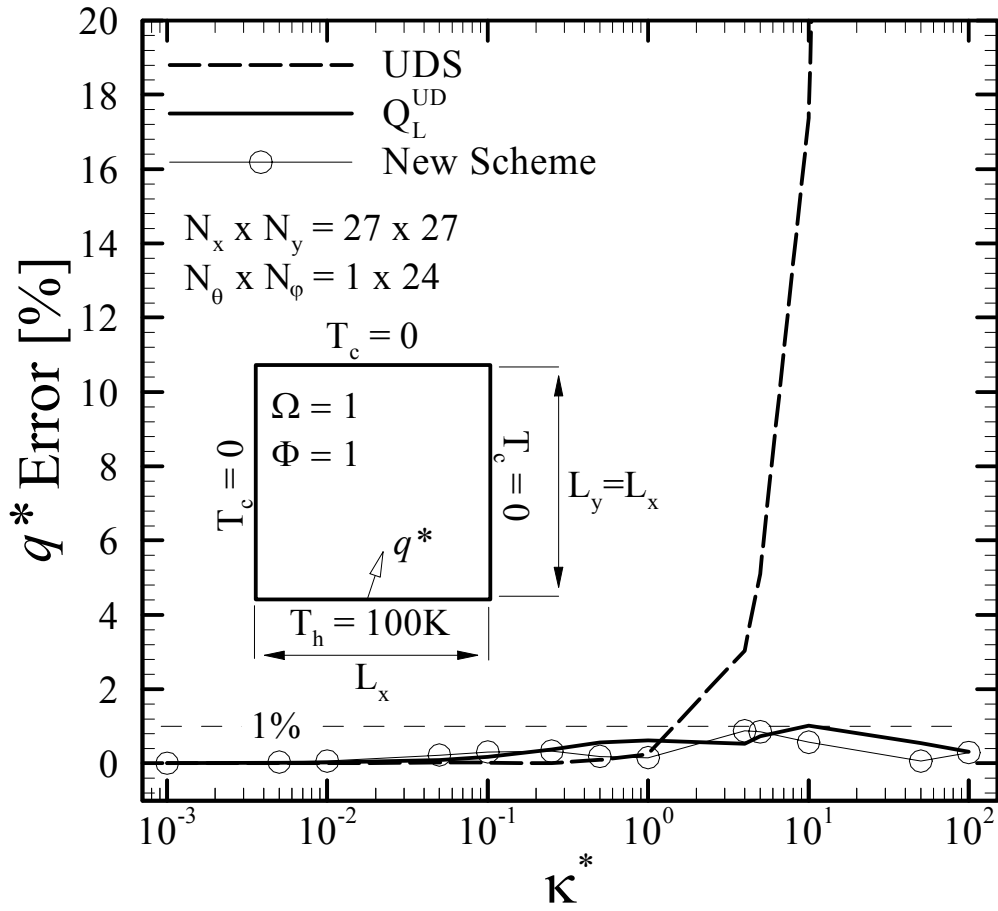


Figure 5.5: Error percentage in the predicted heat transfer at the center of the bottom surface in a purely isotropically scattering medium enclosed in a square enclosure with black surfaces.

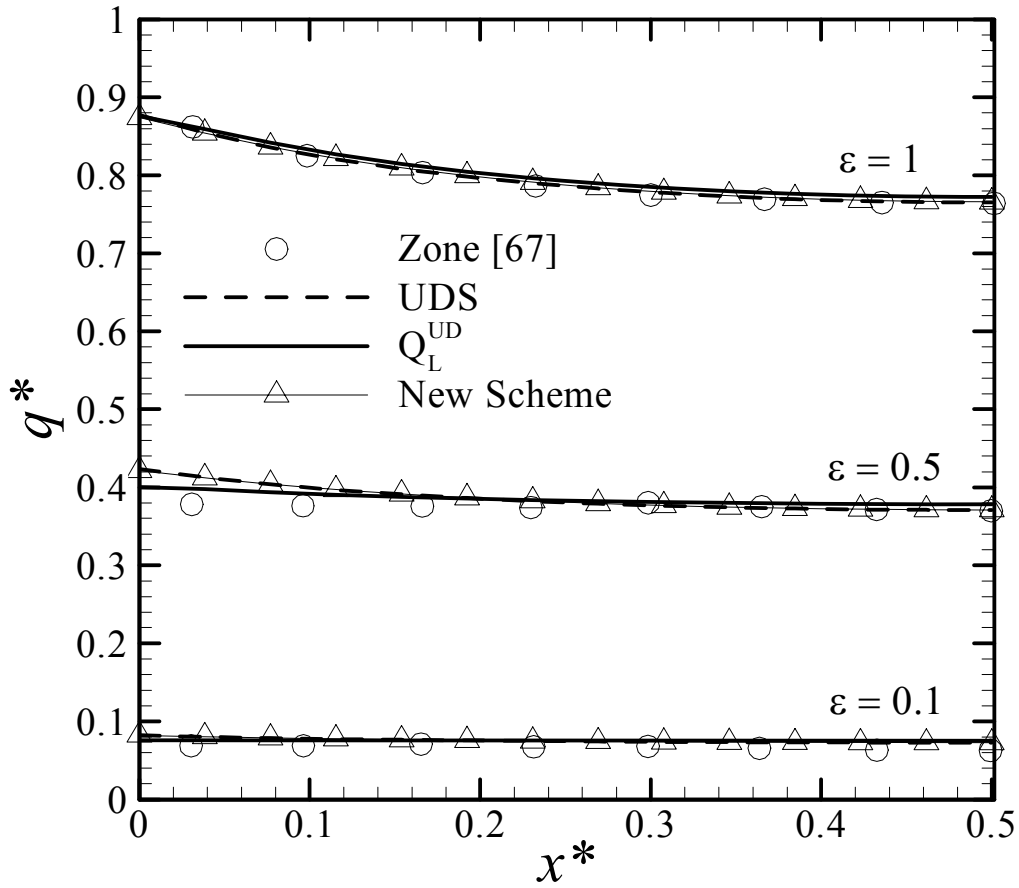


Figure 5.6: Nondimensional heat transfer on the hot bottom surface for a purely isotropically scattering medium enclosed in a square enclosure with partially reflecting surfaces.

Table 5.1: The solution cost and number of cycles required by the UDS and New Scheme applied to an isotropically scattering medium enclosed in a square enclosure with black surfaces.

		UDS		New Scheme	
κ^*	ϵ	cycle	WU	cycle	WU
0.25	1	5	0.5	8	70.5
1	0.1	113	11.1	163	140.1
	0.5	21	1.5	27	39.4
	1	9	0.6	9	27.8
10	1	87	6.2	87	40.1

Solution Cost

In addition to accuracy, it is also important to study the solution cost of the New Scheme and compare it with the cost of the UDS. In Table 5.1, the solution cost and number of cycles for these two methods have been reported for the problems solved before.

These results show that whereas the UDS and New Scheme have similar convergence rates (number of cycles), the New Scheme is much costlier than the UDS, especially for small optical thicknesses. This means that a cycle in the New Scheme is much more expensive than a cycle using UDS.

The reason of this large cost for each cycle of the New Scheme is that in this scheme, for a given direction, the intensities in all control volumes are spatially coupled because of the elliptic nature of the equations and an iterative solution is required to obtain the intensity field in each direction even when the I_a and I_b fields are known for an isotropically scattering medium in an enclosure with black surfaces. In spite of using the multigrid solver, solving the resulting equations may be costly especially when the optical thickness is small. In contrast to this scheme, for UDS, if the I_a and I_b fields are known for an isotropically scattering medium and the surfaces are black, the intensity in each control volume in a given direction only depends on the upstream intensities (parabolic nature), and therefore the solution is obtained in a single sweep of the grid.

5.4.2 Rectangular Enclosure

To further study the accuracy of the New Scheme, this method has been applied to two rectangular enclosures solved in the previous chapter ($AR = 10$ and $1/5$). All

surfaces are black and the optical thickness of the purely isotropically scattering medium is unity ($\sigma^s L_y = 1$).

For the enclosure with $AR = 10$, $N_x \times N_y = 9 \times 25$ control volumes have been used for the spatial grid with 3 levels in the multigrid solver ($MN_x \times MN_y = 3 \times 5$). $N_x \times N_y = 25 \times 9$ control volumes with 3 levels in the multigrid solver ($MN_x \times MN_y = 5 \times 3$) have been employed for the spatial grid in the case that $AR = 1/5$. In both cases, $N_\theta \times N_\phi = 1 \times 24$ solid angles are used for the angular discretization.

Figs.5.7 and 5.8 compare the q^* and T^* distributions predicted by the New Scheme with the exact solution and results of the UDS and Q_L^{UD} . These comparisons show that these three methods yield very accurate predictions for this set of coarse grids for the tall enclosure where the optical thickness is small. For the wide enclosure, New Scheme and Q_L^{UD} have comparable accuracies and both are more accurate than the UDS since the medium is dense in the x direction ($\kappa_x^* = 5$).

5.5 Concluding Remarks

A new spatial differencing scheme, the New Scheme, is introduced in this chapter. In this scheme, the radiant heat flux at an integration point is related to the gradient of I^l at that integration point which is easily calculated by a second-order linear profile approximation.

The New Scheme was applied to several simple 2D problems and found to be accurate in both optically thin and thick limits for the tested coarse grids. However, this scheme is very costly compared to the UDS, especially in the optically thin media.

Besides being very costly, it has been observed that the accuracy of the Q_L^{UD} method is comparable to the accuracy of the Q_L^{NS} . In fact, up to this point, studies have shown that the UDS can efficiently provide an accurate α^l distribution for the Q_L method. However, it should be pointed out that the Q_L^{UD} method is first order (because of the UDS) and to obtain a second-order method, the α^l distribution should be second-order accurate which implies the necessity of using a second-order differencing scheme in the FVM.

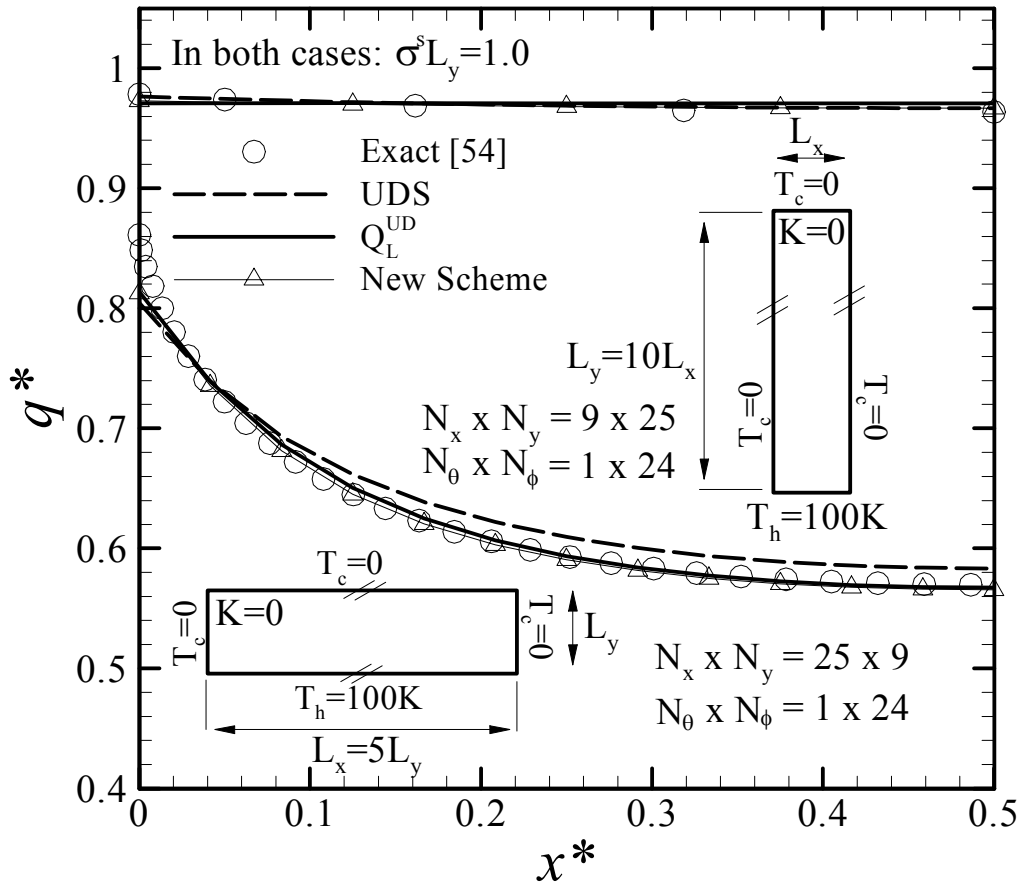


Figure 5.7: Nondimensional heat transfer on the hot bottom surface for a purely isotropically scattering medium with unit optical thickness in rectangular enclosures with black surfaces.

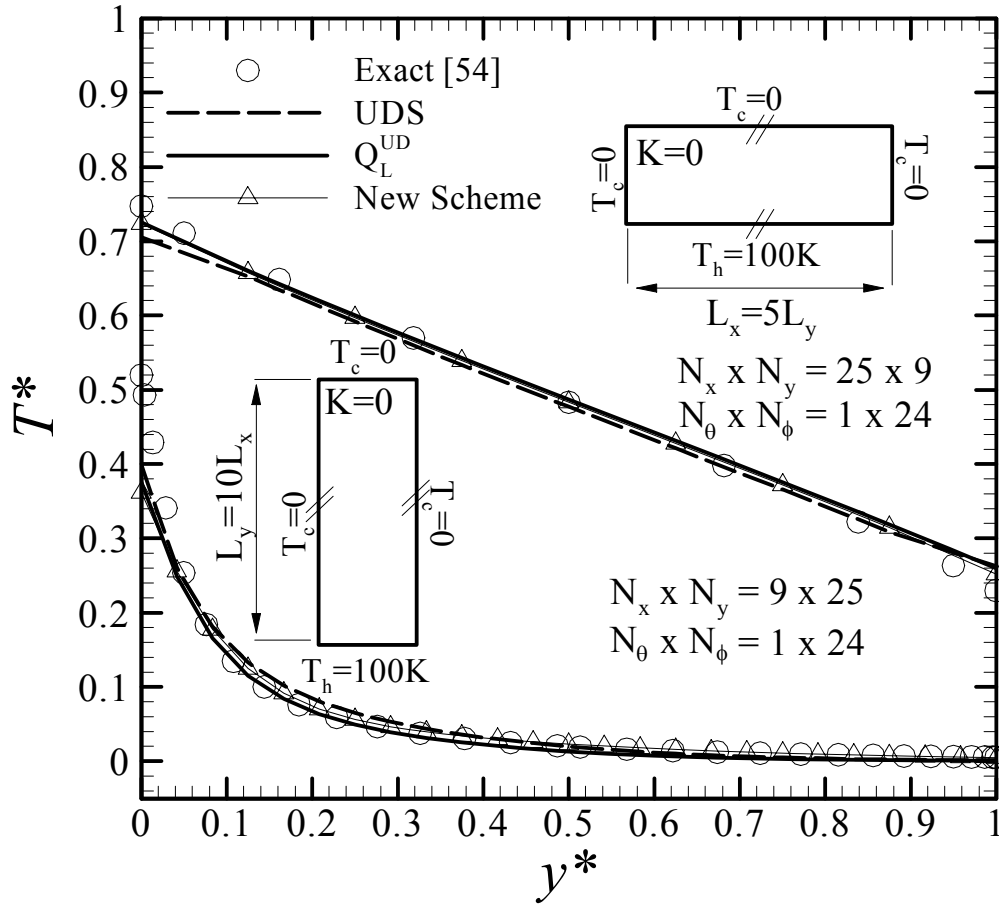


Figure 5.8: Nondimensional temperature along the centerline for a purely isotropically scattering medium with unit optical thickness in rectangular enclosures with black surfaces.

Chapter 6

Summary

In this study, a new computational radiation method, the Q_L method, has been investigated which is shown to be accurate, efficient, and stable. In this method, a single equation for I_a in each control volume is derived where heat flux at the integration points is obtained by re-arranging the RTE, and the phase weight concept is used to include the directional effects in this equation. Therefore, whereas this equation solves for I_a in each control volume, which ensures conservation of radiant energy in the control volume, it also accounts for the directional effects. The phase weights can be obtained from a method such as the FVM.

The Q_L equations are elliptic and standard differencing schemes (e.g. central differencing scheme) and efficient linear equations solvers (e.g. multigrid) are applicable to solve them. This method can be implemented in non-orthogonal and unstructured meshes, and is capable of handling anisotropic scattering (with any kind of phase function), partially reflecting boundaries, non-uniform radiative properties, and spectral effects.

In this research, the equations for the general case were derived and several simple 1D and 2D benchmark problems, including isotropic and anisotropic scattering, black and partially reflecting boundaries, and emitting-absorbing media, were solved on Cartesian grids to study the performance of this method. These test cases showed that the Q_L method is very stable and always converges with a reasonable number of cycles, regardless of the grid size and optical thickness. For the large optical thicknesses, especially when the surfaces are partially reflecting, the solution cost¹ of the Q_L method is much lower than the cost of the FVM with explicit update. There is a cost penalty for very small optical thicknesses which

¹Measured in work units.

is not of great importance since the solution cost in this limit is low. Also it was pointed out that the Q_L method does not work when κ^* is exactly zero, since the Q_L equations will be ill-posed. This drawback and the small cost penalty in the optically thin limit are the only disadvantages of the Q_L method have been diagnosed so far.

Solution of the Q_L method approaches the exact solution with spatial and angular grids refinement, and results of the benchmark problems showed that the Q_L method has similar or better accuracy than the FVM with UDS for a given spatial and angular grid. Especially in the optically dense limit, the Q_L method gives the correct diffusion approximation.

In this research, the Q_L method was only studied for simple test cases where the RTE and internal energy equation were disconnected. The real advantage of the Q_L method over the other available computational methods can be demonstrated when a fluid flow and heat transfer problem is solved. In such a costly problem, using the Q_L method can substantially reduce the computational cost compared to using the FVM with explicit update since: 1) only one variable (I_a) for radiation is solved for each control volume (instead of L directional intensities²), and 2) during the iterative solution, the radiant energy is conserved in each control volume. Therefore, the cost per cycle is less and the convergence rate is expected to be fast which together, will reduce the solution cost dramatically. The FVM is only applied occasionally to update the phase weight distribution and improve the accuracy.

Besides studying the Q_L method, a new differencing scheme has been introduced in this thesis. In this method, the radiant heat flux at the integration points is calculated by re-arranging the RTE and therefore, this scheme has a similar formulation to the Q_L equations, except that its equations are integrated over ω^l instead of 4π .

This scheme can be applied to the FVM or DOM and the resulting equations are elliptic. The standard differencing schemes and efficient linear equations solvers can be applied to solve these equations as well. The FVM with the new scheme is used to solve several 2D benchmark problems. Results on the coarse grids have shown that this method yields very accurate predictions in both optically thin and thick limits, and has similar or better (for the thick limit) accuracy than the FVM with UDS. The major drawback of this scheme is that it is very costly, especially when the optical thickness is small.

The distinctive feature of the Q_L method, solving for I_a with the directional

² L is the number of discrete solid angles and depends on the required accuracy. It may be larger than 30.

effects included, along with its very good performance observed in this study suggests this method as a promising method for general fluid flow and heat transfer solvers. This encourages further exploration and development of this method. In the following, a few suggestions for future research are given.

6.1 Future Directions

There are a few recommendations for future work on the Q_L method:

1. The Q_L method should be extended to 3D problems with non-orthogonal and unstructured grids. One issue that may arise is complexity of the equations since the Q_L equations contain both non-mixed derivatives (i.e. $\partial/\partial x_1 \mathbf{e}_1$) and mixed derivatives (i.e. $\partial/\partial x_1 \mathbf{e}_2$) which may increase the complexity. One remedy for this problem is lagging the mixed derivatives, but it may slow down the convergence.
2. The other important issue regarding the Q_L equations is that these equations are not guaranteed to be diagonally dominant since the coefficients depend on the α^l distribution. Although the Q_L method was found very stable in the tested cases, the only way to guarantee this robustness for any kind of problem is ensuring the diagonal dominance. Therefore, it is worth to try to assure the diagonal dominance of the Q_L equations.
3. The most important suggestion for the next stage is using the Q_L method in a fluid flow and heat transfer solver to explore its performance. In such a solver, it would be possible to control the solution cost and accuracy with changing the number of α^l distribution updates.
4. Although the FVM with UDS was found accurate enough to calculate the α^l distribution for the Q_L method in the simple test cases, the solution is first-order accurate. Therefore, it is suggested to study the effect of more accurate differencing schemes in the FVM on the performance of the Q_L method.
5. There is a cost penalty for the small optical thicknesses, and the Q_L method does not work when $\kappa^* = 0$. This problem can be overcome by changing the value of κ^* from zero to a very small number. The influence of these drawbacks for the nearly non-participating media in practical problems should be meticulously scrutinized.

Bibliography

- [1] Hollands, K. G. T., *Thermal Radiation Fundamentals*, 1st ed., Begell House Inc., New York, 2004.
- [2] Viskanta, R., and Mengüç, M. P., “Radiation Heat Transfer in Combustion Systems,” *Progress in Energy and Combustion Science*, Vol. 13, No. 2, 1987, pp. 97 – 160.
- [3] Modest, M. F., *Radiative Heat Transfer*, 2nd ed., Academic Press, New York, 2003.
- [4] Lewis, E. E., and Miller, W. F., *Computational Methods of Neutron Transport*, John Wiley & Sons, New York, 1984.
- [5] Siegel, R., and Howell, J. R., *Thermal Radiation Heat Transfer*, 3rd ed., Hemisphere Publishing Corp., 1992.
- [6] Sazhin, S. S., Sazhina, E. M., Faltsi-Saravelou, O., and Wild, P., “The P_1 Model for Thermal Radiation Transfer: Advantages and Limitations,” *Fuel*, Vol. 75, No. 3, 1996, pp. 289 – 294.
- [7] Chandrasekhar, S., *Radiative Transfer*, Dover Publications, 1960.
- [8] Lathrop, K. D., “Use of Discrete-Ordinate Methods for Solution of Photon Transport Problems,” *Nuclear Science and Engineering*, Vol. 24, 1966, pp. 381 – 388.
- [9] Carlson, B. G., and Lathrop, K. D., “Transport Theory-the Method of Discrete Ordinates ,” *Computing Methods in Reactor Physics*, eds. H. Greenspan, C. N. Kelber, and D. Okrent, Gordon & Breach, New York, 1968.
- [10] Fiveland, W. A., “A Discrete Ordinates Method for Predicting Radiative Heat Transfer in Axisymmetric Enclosures,” *ASME Paper 82-HT-20*, 1982.

- [11] Fiveland, W. A., “Discrete Ordinate Solutions of the Radiative Transport Equation for Rectangular Enclosures,” *Journal of Heat Transfer*, Vol. 106, 1984, pp. 699 – 706.
- [12] Fiveland, W. A., “Discrete Ordinate Methods for Radiative Heat Transfer in Isotropically and Anisotropically Scattering Media,” *Journal of Heat Transfer*, Vol. 109, 1987, pp. 809 – 812.
- [13] Truelove, J. S., “Discrete-Ordinate Solutions of the Radiation Transport Equation,” *Journal of Heat Transfer*, Vol. 109, No. 4, 1987, pp. 1048 – 1051.
- [14] Truelove, J. S., “Three-Dimensional Radiation in Absorbing-Emitting-Scattering Media using the Discrete-Ordinates Approximation,” *Journal of Quantitative Spectroscopy and Radiative Transfer*, Vol. 39, No. 1, 1988, pp. 27 – 31.
- [15] Raithby, G. D., and Chui, E. H., “A Finite-Volume Method for Predicting a Radiant Heat Transfer in Enclosures with Participating Media,” *Journal of Heat Transfer*, Vol. 112, 1990, pp. 415 – 423.
- [16] Chui, E. H., and Raithby, G. D., “Computation of Radiant Heat Transfer on a Nonorthogonal Mesh using the Finite Volume Method,” *Numerical Heat Transfer*, Vol. 23, 1993, pp. 269 – 288.
- [17] Baek, S. W., Kim, M. Y., and Kim, J. S., “Nonorthogonal Finite-Volume Solutions of Radiative Heat Transfer in a Three-dimensional Enclosure,” *Numerical Heat Transfer*, Vol. 34, 1998, pp. 419 – 437.
- [18] Chui, E. H., Raithby, G. D., and Hughes, P. M. J., “Prediction of Radiative Heat Transfer in Cylindrical Enclosures with the Finite Volume Method,” *Journal of Thermophysics and Heat Transfer*, Vol. 6, No. 4, 1992, pp. 605–611.
- [19] Moder, J. P., Chai, J. C., Parthasarathy, G., Lee, H. S., and Patankar, S. V. “Nonaxisymmetric Radiative Transfer in Cylindrical Enclosures,” *Numerical Heat Transfer*, Vol. 30, 1996, pp. 437 – 452.
- [20] Kim, M. Y., and Baek, S. W., “Radiative Heat Transfer in a Body-fitted Axisymmetric Cylindrical Enclosure,” *Journal of Thermophysics and Heat Transfer*, Vol. 12, 1998, pp. 596 – 599.
- [21] Ben Salah, M., Askri, F., Slimi, K., and Ben Nasrallah, S., “Numerical Resolution of the Radiative Transfer Equation in a Cylindrical Enclosure with the

- Finite-Volume Method,” *International Journal of Heat and Mass Transfer*, Vol. 47, 2004, pp. 2501 – 2509.
- [22] Chui, E. H., Hughes, P. M. J., and Raithby, G. D., “Implementation of the Finite Volume Method for Calculating Radiative Heat Transfer in a Pulverized Fuel Flame,” *Combustion Science and Technology*, Vol. 92, No. 4/6, 1993, pp. 225 – 242.
- [23] Murthy, J. Y., and Mathur, S. R., “Finite Volume Method for Radiative Heat Transfer using Unstructured Meshes,” *Journal of Thermophysics and Heat Transfer*, Vol. 12, No. 3, 1998, pp. 313 – 321.
- [24] Murthy, J. Y., and Mathur, S. R., “Radiative Heat Transfer in Axisymmetric Geometries using an Unstructured Finite-Volume Method,” *Numerical Heat Transfer*, Vol. 33, 1998, pp. 397 – 416.
- [25] Liu, J., Shang, H. M., and Chen, Y. S., “Development of an Unstructured Radiation Model Applicable for Two-dimensional Planar, Axisymmetric, and Three-dimensional Geometries,” *Journal of Quantitative Spectroscopy and Radiative Transfer*, Vol. 66, 2000, pp. 17 – 33.
- [26] Kim, M. Y., Baek, S. W., and Park, J. H., “Unstructured Finite-Volume Method for Radiative Heat Transfer in a Complex Two-dimensional Geometry with Obstacles,” *Numerical Heat Transfer*, Vol. 39, 2001, pp. 617 – 635.
- [27] Kim, G., Kim, S., and Kim, Y., “Parallelized Unstructured-Grid Finite Volume Method for Modeling Radiative Heat Transfer,” *Journal of Mechanical Science and Technology*, Vol. 19, 2005, pp. 1006 – 1017.
- [28] Mathur, S. R., and Murthy, J. Y., “Radiative Heat Transfer in Periodic Geometries using a Finite Volume Scheme,” *Journal of Heat Transfer*, Vol. 121, No. 2, 1999, pp. 357 – 364.
- [29] Chai, J. C., Lee, H. S., and Patankar, S. V., “Treatment of Irregular Geometries using a Cartesian Coordinates Finite-Volume Radiation Heat Transfer Procedure,” *Numerical Heat Transfer*, Vol. 26, 1994, pp. 225 – 235.
- [30] Chai, J. C., Parthasarathy, G., Lee, H. S., and Patankar, S. V., “Finite Volume Method Radiative Heat Transfer Procedure for Irregular Geometries,” *Journal of Thermophysics and Heat Transfer*, Vol. 9, No. 3, 1995, pp. 410 – 415.

- [31] Chai, J. C., Lee, H. S., and Patankar, S. V., “Finite Volume Method for Radiation Heat Transfer,” *Journal of Thermophysics and Heat Transfer*, Vol. 8, No. 3, 1994, pp. 419 – 425.
- [32] Raithby, G. D., “Discussion of the Finite-Volume Method for Radiation, and its Application using 3D Unstructured Meshes,” *Numerical Heat Transfer*, Vol. 35, No. 4, 1999, pp. 389 – 405.
- [33] Liu, J., Shang, H. M., Chen, Y. S., and Wang, T. S., “Analysis of Discrete Ordinates Method with Even Parity Formulation,” *Journal of Thermophysics and Heat Transfer*, Vol. 11, No. 2, 1997, pp. 253 – 260.
- [34] Fiveland, W. A., and Jessee, J. P., “Comparison of Discrete Ordinates Formulation for Radiative Heat-Transfer in Multidimensional Geometries,” *Journal of Thermophysics and Heat Transfer*, Vol. 9, No. 1, 1995, pp. 47 – 54.
- [35] Kim, S. H., and Huh, K. Y., “Assessment of the Finite-Volume Method and the Discrete Ordinate Method for Radiative Heat Transfer in a Three-Dimensional Rectangular Enclosure,” *Numerical Heat Transfer*, Vol. 35, No. 1, 1999, pp. 85 – 112.
- [36] Raithby, G. D., “Evaluation of Discretization Errors in Finite-Volume Radiant Heat Transfer Predictions,” *Numerical Heat Transfer*, Vol. 36, 1999, pp. 241 – 264.
- [37] Kim, S. H., and Huh, K. Y., “A New Angular Discretization Scheme of the Finite Volume Method for 3D Radiative Heat Transfer in Absorbing, Emitting and Anisotropically Scattering Media,” *International Journal of Heat and Mass Transfer*, Vol. 43, 2000, pp. 1233 – 1242.
- [38] Vaidya, N., “Multidimensional Simulation of Radiation using an Unstructured FVM,” AIAA Paper 98-0856, 1998.
- [39] Chui, E. H., and Raithby, G. D., “Implicit Solution Scheme to Improve Convergence Rate in Radiative Transfer Problems,” *Numerical Heat Transfer*, Vol. 22, 1992, pp. 251 – 272.
- [40] Chui, E. H., “Modeling of Radiative Heat Transfer in Participating Media by The Finite Volume Method,” PhD thesis, University of Waterloo, 1990.
- [41] Fiveland, W. A., and Jessee, J. P., “Acceleration Schemes for the Discrete Ordinates Method,” *Journal of Thermophysics and Heat Transfer*, Vol. 10, No. 3, 1996, pp. 445 – 451.

- [42] Raithby, G. D., and Chui, E. H., “Accelerated Solution of the Radiation-Transfer Equation with Strong Scattering,” *Journal of Thermophysics and Heat Transfer*, Vol. 18, No. 4, 2004, pp. 156 – 159.
- [43] Cefus, G. R., and Larsen, E. W., “Stability Analysis of Coarse-Mesh Rebalance,” *Nuclear Science and Engineering*, Vol. 105, 1990, pp. 31 – 39.
- [44] Cho, N. Z., and Park, C. J., “A Comparison of Coarse Mesh Rebalance and Coarse Mesh Finite Difference Accelerations for the Neutron Transport Calculations,” *Proceeding Nuclear Mathematical and Computational Sciences: A Century in Review, A century Anew*, Gatlinburg, Tennessee, April 6 – 11, 2003, American Nuclear Society (2003). [CD-ROM]
- [45] Yamamoto, A., Kitamura, Y., Ushio, T., and Sugimura, N., “Convergence Improvement of Coarse Mesh Rebalance Method for Neutron Transport Calculations,” *Journal of Nuclear Science and Technology*, Vol. 41, No. 8, 2004, pp. 781 – 789.
- [46] Mathur, S. R., and Murthy, J. Y., “Coupled Ordinates Method for Multigrid Acceleration of Radiation Calculations,” *Journal of Thermophysics and Heat Transfer*, Vol. 13, No. 4, 1999, pp. 467 – 473.
- [47] Mathur, S. R., and Murthy, J. Y., “Acceleration of Anisotropic Scattering Computations using Coupled Ordinates Method (COMET),” *Journal of Heat Transfer*, Vol. 123, 2001, pp. 607 – 612.
- [48] Hutchinson, B. R., and Raithby, G. D., “A Multigrid Method Based on the Additive Correction Strategy,” *Numerical Heat Transfer*, Vol. 9, 1986, pp. 511 – 537.
- [49] Heaslet, M. A., and Warming, R. F., “Radiative Transport and Wall Temperature Slip in Absorbing Planar Medium,” *International Journal of Heat Mass Transfer*, Vol. 8, 1965, pp. 979 – 994.
- [50] Olfe, D. B., “A Modification of Differential Approximation for Radiative Transfer,” *AIAA Journal*, Vol. 5, No. 4, 1967, pp. 638.
- [51] Bayazitoglu, Y., and Higenyi, J., “Higher-Order Differential Equations of Radiative Transfer: P_3 Approximation,” *AIAA Journal*, Vol. 17, No. 4, 1979, pp. 424 – 431.

- [52] Busbridge, I. W., and Orchard, S. E., “Reflection and Transmission of Light by a Thick Atmosphere According to a Phase Function: $1 + x \cos(\theta)$,” *The Astrophysical Journal*, Vol. 149, 1967, pp. 655 – 664.
- [53] Orchard, S. E., “Reflection and Transmission of Light by a Thick Atmosphere of Pure Scatterers with a Phase Function: $1 + \bar{\omega}_1 P_1(\cos(\theta)) + \bar{\omega}_2 P_2(\cos(\theta))$,” *The Astrophysical Journal*, Vol. 149, 1967, pp. 665 – 674.
- [54] Crosbie, A. L., and Schrenker, R. G., “Radiative Transfer in a Two-Dimensional Rectangular Medium Exposed to Diffuse Radiation,” *Journal of Quantitative Spectroscopy and Radiative Transfer*, Vol. 31, No. 4, 1984, pp. 339 – 372.
- [55] Altaç, Z., and Tekkalmaz, M., “Solution of the Radiative Integral Transfer Equations in Rectangular Absorbing, Emitting, and Anisotropically Scattering Homogeneous Medium,” *Journal of Heat Transfer*, Vol. 126, 2004, pp. 137 – 140.
- [56] Chung, T. J., *Computational Fluid Dynamics*, 1st ed., Cambridge University Press, United Kingdom, 2002.
- [57] Jessee, J. P., and Fiveland, W. A., “Bounded, High-Resolution Differencing Schemes Applied to the Discrete Ordinates Method,” *Journal of Thermophysics and Heat Transfer*, Vol. 11, No. 4, 1997, pp. 540 – 548.
- [58] Lathrop, K. D., “Spatial Differencing of the Transport Equation: Positivity vs. Accuracy,” *Journal of Computational Physics*, Vol. 4, 1969, pp. 475 – 498.
- [59] Jamaluddin, A. S., and Smith, P. J., “Predicting Radiative Transfer in Rectangular Enclosures using the Discrete Ordinates Method,” *Combustion and Technology*, Vol. 59, 1988, pp. 321 – 340.
- [60] Fiveland, W. A., “Three Dimensional Radiative Heat Transfer Solution by the Discrete Ordinates Method,” *Journal of Thermophysics and Heat Transfer*, Vol. 2, No. 4, 1988, pp. 309 – 316.
- [61] Chai, J. C., Patankar, S. V., and Lee, H. S., “Evaluation of Spatial Differencing Practices for the Discrete-Ordinates Method,” *Journal of Thermophysics and Heat Transfer*, Vol. 8, No. 1, 1994, pp. 140 – 144.
- [62] Lathrop, K. D., and Carlson, B. “Numerical Solution of the Boltzmann Transport Equation,” *Journal of Computational Physics*, Vol. 2, 1967, pp. 173 – 197.

- [63] Chai, J. C., Lee, H. S., and Patankar, S. V., “Improved Treatment of Scattering using the Discrete Ordinates Method,” *Journal of Heat Transfer*, No. 116, 1994, pp. 260 – 263.
- [64] Fiveland, W. A., and Jessee, J. P., “Finite Element Formulation of the Discrete-Ordinates Method for Multidimensional Geometries” *Journal of Thermophysics and Heat Transfer*, Vol. 8, No. 3, 1994, pp. 426 – 433.
- [65] Liu, J., Shang, H. M., Chen, Y. S., and Wang, T. S., “Analysis of Discrete Ordinates Method with Even Parity Formulation” *Journal of Thermophysics and Heat Transfer*, Vol. 11, No. 2, 1997, pp. 253 – 260.
- [66] Kaplan, S., and Davis, J., “Canonical and Involuntary Transformation of the Variational Problems of Transport Theory” *Numerical Science and Engineering*, Vol. 28, No. 1, 1967, pp. 166 – 176.
- [67] Ratzel, A. C., and Howell, J. R., “Two-Dimensional Radiation in Absorbing-Emitting Media using the $P-N$ Approximation” *Journal of Heat Transfer*, Vol. 105, 1983, pp. 333 – 340.
- [68] Li, G., and Modest, M. F., “A Method to Accelerate Convergence and to Preserve Radiative Energy Balance in Solving the P1 Equation by Iterative Methods” *Journal of Heat Transfer*, Vol. 124, 2002, pp. 580 – 582.
- [69] Krishnamoorthy, G., Rawat, R., and Smith, P. J., “Parallelization of the P-1 Radiation Model” *Numerical Heat Transfer*, Vol. 49, 2006, pp. 1 – 17.

Appendix A

The Multiplicative Method

It was stated in Chapter 1 that the best available acceleration scheme for the RTE, the multiplicative method, is practically useless since it fails to produce convergence for the strongly participating media on fine grids [41, 42]. Understanding the reason of this poor performance can be very helpful in developing new efficient methods. In this appendix, after a brief introduction to the multiplicative method, the convergence of the accelerated RTE solution with the multiplicative method will be studied to demonstrate its performance and its breakdown for certain conditions. Then the reason of this failure will be discussed.

A.1 Formulation of the Multiplicative Method

The multiplicative method has been formulated based on the conservation of total radiant energy over each control volume. Fiveland and Jessee [41] interpreted the multiplicative method as a two-level multigrid scheme where the angular rather than the spatial discretization is coarsened.

Discretizing the RTE with the finite volume method gives (Eq.(1.10))

$$a_P^l I_P^l = \sum_{nb} a_{nb}^l I_{nb}^l + b_P^l \quad (\text{A.1})$$

where nb refers to the neighbor nodes. This equation ensures conservation of radiant energy over the control volume surrounding node P within the discrete solid angle ω^l . Therefore, summing this equation over all solid angles will yield an equation

that ensures total energy conservation over all directions for this control volume:

$$\sum_{l=1}^L a_P^l I_P^l = \sum_{l=1}^L \sum_{nb} a_{nb}^l I_{nb}^l + \sum_{l=1}^L b_P^l \quad (\text{A.2})$$

where L is the total number of solid angles so that $\sum_{l=1}^L \omega^l = 4\pi$.

The phase weight was defined before as

$$\alpha_P^l = \frac{I_P^l}{I_{a,P}}$$

where re-arranging gives

$$I_P^l = \alpha_P^l I_{a,P} \quad (\text{A.3})$$

Inserting Eq.(A.3) in Eq.(A.2) and combining all direction-dependent parameters in the coefficients a and the source term b gives an implicit equation for I_a as

$$a_P I_{a,P} = \sum_{nb} a_{nb} I_{a,nb} + b_P \quad (\text{A.4})$$

The coefficients and the source term for the general case has been presented in [39] and [40].

A.2 Performance and Failure

In this section, a simple 2D problem is solved to study the performance of the multiplicative method. The medium is purely isotropically scattering (with scattering coefficient = σ^s) and gray, enclosed in a square enclosure of dimension $H \times H$ with black walls. The bottom wall is hot at 100 K and the other three walls are cold at 0 K.

Radiative heat transfer has been found by solving the RTE with the finite volume method of Raithby and Chui [15]. The UDS is used to discretize the RTE and the multiplicative method of Chui and Raithby [39] is used to accelerate the convergence.

In this case, the governing equations are the discretized RTE (Eq.(A.1))

$$\underbrace{\left(\overbrace{\sum_{nb} a_{nb}^l}^{\tilde{a}_P^l} + \sigma^s V_P \omega^l \right)}_{a_P^l} I_P^l = \sum_{nb} a_{nb}^l I_{nb}^l + \underbrace{\sigma^s V_P \omega^l I_{a,P}}_{b_P^l} \quad (\text{A.5})$$

and the implicit equation (Eq.(A.4))

$$a_P I_{a,P} = \sum_{nb} a_{nb} I_{a,nb} + b_P \quad (\text{A.6})$$

where

$$a_P = \sum_L \hat{a}_P^l \alpha_P^l \quad \text{and} \quad a_{nb} = \sum_l a_{nb}^l \alpha_{nb}^l \quad (\text{A.7})$$

and $b_P = 0$ except at the boundaries. These coefficients will be presented later.

The phase weights are calculated from

$$\alpha_P^l = \frac{I_P^l}{\tilde{I}_{a,P}} \quad (\text{A.8})$$

where $\tilde{I}_{a,P} = \frac{1}{4\pi} \sum_L I_P^l \omega^l$, and the I_P^l values are obtained from Eq.(A.5). The solution procedure is:

1. All I_a values are initialized (in this case: 10^{-5} W m^{-2}).
2. Eq.(A.5) is solved for each node and each solid angle to find I_P^l .
3. The intermediate $I_{a,P}$ values ($\tilde{I}_{a,P}$) are calculated from $\tilde{I}_{a,P} = \frac{1}{4\pi} \sum_{l=1}^L I_P^l \omega^l$.
4. α_P^l values are updated from Eq.(A.8).
5. Using the newly evaluated phase weights, Eq.(A.7) is used to calculate the coefficients of the implicit equation (Eq.(A.6)).
6. Eq.(A.6) is solved for I_a at each node.
7. Steps 2 through 7 are repeated until the convergence criterion is satisfied.

Steps 2 through 7 constitute a cycle. The solution is judged to have converged in Step 7 when the scaled residuals for all of the I_a equations in the multiplicative method have reduced to 10^{-6} . In each cycle, the I_a equations are solved to reduce the scaled maximum residuals to 10^{-4} (Step 6). Because of the parabolic character of Eq.(A.5), the solution of this equation (Step 2) can be achieved by one sweep over all control volumes and solid angles. This has been explained before in Chapter 3 (see Fig.3.4)

A 2D uniform Cartesian vertex-centered grid, which was explained in Chapter 3, with $N \times N$ control volumes has been used. The width and height of the interior

Table A.1: Number of cycles to achieve convergence in a 2D problem for the multiplicative method.

Grid size	$\sigma^s \Delta$									
	0.001	0.01	0.05	0.10	0.25	0.5	1.0	5.0	10	100
5×5	4	5	6	7	10	11	11	8	7	5
10×10	4	5	8	10	15	18	16	9	8	5
25×25	4	7	13	23	89	101	34	11	9	6
50×50	5	9	29	/	/	/	92	11	8	6
100×100	5	12	/	/	Div.	Div.	Div.	12	9	6

control volumes are $\Delta = H/(N - 1)$. Direction is divided into L equal solid angles labeled $\omega^1, \omega^2, \dots, \omega^l, \dots, \omega^L$. Each solid angle covers the complete range of the polar angle ($0 \leq \theta \leq \pi$). 24 solid angles have been used for this problem.

It has been shown [41, 42] that the cell optical thickness ($\sigma^s \Delta$) plays a more important role than the optical thickness ($\sigma^s H$) in the performance of the multiplicative method. Thus, in this study the attention has been focused on the cell optical thickness and the grid size.

Table A.1 shows the number of cycles to achieve convergence for different grid sizes and cell optical thicknesses. These results show that for coarse grids, the method works well for all values of $\sigma^s \Delta$, as reported before [39, 41, 42]. In some cases for the fine grids and $0.05 \leq \sigma^s \Delta \leq 1.0$, convergence was not achieved and in fact, the code diverged for three cases, as indicated by “Div.”. This range for poor convergence was previously reported by Raithby and Chui [42]. In cases which are indicated by “/”, the convergence was not achieved within 150 cycles. The reason of this failure is given in the next section.

A.3 The Breakdown

The poor convergence of the iterative solution, indicated in Table A.1, has been discussed by Raithby and Chui [42]. Their explanation is given first and then a very simple 1D problem will be used to support it.

There are only two ways for interaction between the equations in the multiplicative method:

1. The calculated values of $I_{a,P}$ from Eq.(A.6) are influenced by the I_P^l values from the solution of Eq.(A.5) only through the phase weights α_P^l .

2. The calculated values of I_p^l from Eq.(A.5) are influenced by the $I_{a,P}$ values computed from Eq.(A.6) only through the term on the right-hand side.

To obtain rapid convergence, at least one of these influences must be weak. For $\sigma^s \Delta \gg 1$, scattering is so dominant that the I_p^l intensities from Eq.(A.5) are very nearly isotropic. Because the information that flows from Eq.(A.5) to Eq.(A.6) is almost independent of the information that flows back from Eq.(A.6) to Eq.(A.5), convergence is achieved rapidly. For $\sigma^s \Delta \ll 1$, the term on the right-hand side of Eq.(A.5) is small, independent of the exact values of $I_{a,P}$, since σ^s is small. Hence, the linkage between Eq.(A.5) and Eq.(A.6) is weak, and the convergence rate is fast.

For intermediate $\sigma^s \Delta$, the phase weights on a given cycle can be asymmetric, being larger in directions pointing away from the lower wall (the hot wall). This results in asymmetric neighbor coefficients a_{nb} in the $I_{a,P}$ equation, with those on the lower side of node P being larger. This carries energy from the hot wall to the medium and increases the level of $I_{a,P}$ in the enclosure. Inserting these $I_{a,P}$ values into Eq.(A.5) yields I_p^l values that are more isotropic (the phase weights are more symmetric) which then reduces the interior values of $I_{a,P}$. The residual bounces from cycle to cycle about some level in a chaotic manner. No oscillations appear on a coarse grid, presumably because the number of degree of freedom is too small.

The lack of diagonal dominance in the $I_{a,P}$ equation appears to amplify the resonance between the equations. Raithby and Chui [42] checked this explanation by underrelaxing Eq.(A.6) to ensure diagonal dominance. This eliminated all cases of divergence but the residual still bounced, and convergence was not achieved. The convergence can be improved by introducing underrelaxation to both Eq.(A.6) and Eq.(A.8). Details of this procedure can be found in [42]. This procedure is not the final solution for the poor convergence since these factors are problem and grid dependent.

The above explanation for the poor convergence and the physical reason of the lack of diagonal dominance are clarified next by an illustrative example.

A.3.1 Illustrative Example

To demonstrate the reasons behind the fluctuations in the I_a values and the lack of diagonal dominance, a very simple 1D problem is solved with the multiplicative method. A purely isotropically scattering gray medium is enclosed between two parallel black surfaces which are at the same temperature $T_B = T_T = 100$ K, and

are 0.1 m apart (Fig.A.1 (d)). The scattering coefficient is $\sigma^s = 18 \text{ m}^{-1}$ and 7 control volumes have been used along with 16 solid angles. Since the first and the last control volumes are half of the others, Δ for the interior control volumes is $\Delta = 0.1/6$ and the cell optical thickness is calculated as

$$\sigma^s \Delta = 18 \times \frac{0.1}{6} = 0.3$$

This cell optical thickness is in the range where the poor convergence was observed for fine grids (Table A.1). However for this problem, since the temperature difference between two walls is zero, the convergence is not achieved even for this very coarse grid ($N = 7$).

Generally, it has been observed in the 1D problems that decreasing the difference between the temperatures of the walls degrades the convergence. For example in this problem, for $T_B = 100 \text{ K}$ and $T_T = 0 \text{ K}$ the solution converges in 16 cycles while for $T_B = 100 \text{ K}$ and $T_T = 80 \text{ K}$ the convergence needs 31 cycles. For the case that we are interested in, $T_B = T_T = 100 \text{ K}$, convergence is never achieved.

Fig.A.1 shows the α^l distribution for the first 3 interior nodes for the first 4 cycles. Since the problem is symmetric, the distributions at the interior nodes above the middle are the mirror image of Fig.A.1. It is seen that the α^l profiles flip between the solid-line profiles and the dashed-line profiles and each is repeated in every second cycle. For example, the distributions for cycles 2 and 4 are almost the same. This behavior was observed before by Raithby and Chui [42] for the 2D problem and the reason was explained in the last section.

To better understand this behavior, we should look at the matrix of coefficients, the I_a distributions, and the α^l profiles simultaneously. The α^l profiles were presented before, but the two others (matrix of coefficients and I_a distributions) need to be explained.

Matrix of Coefficients: Eq.(A.6) may be written in the matrix form as

$$[A] \{I_a\} = [B]$$

where the elements of the matrix of coefficients $[A]$ are obtained from Eq.(A.7):

$$[A] = \begin{bmatrix} a_P^1 & -a_N^1 & 0 & 0 & 0 \\ \ddots & \ddots & \ddots & 0 & 0 \\ 0 & -a_S^i & a_P^i & -a_N^i & 0 \\ 0 & 0 & \ddots & \ddots & \ddots \\ 0 & 0 & 0 & -a_S^7 & a_P^7 \end{bmatrix}$$

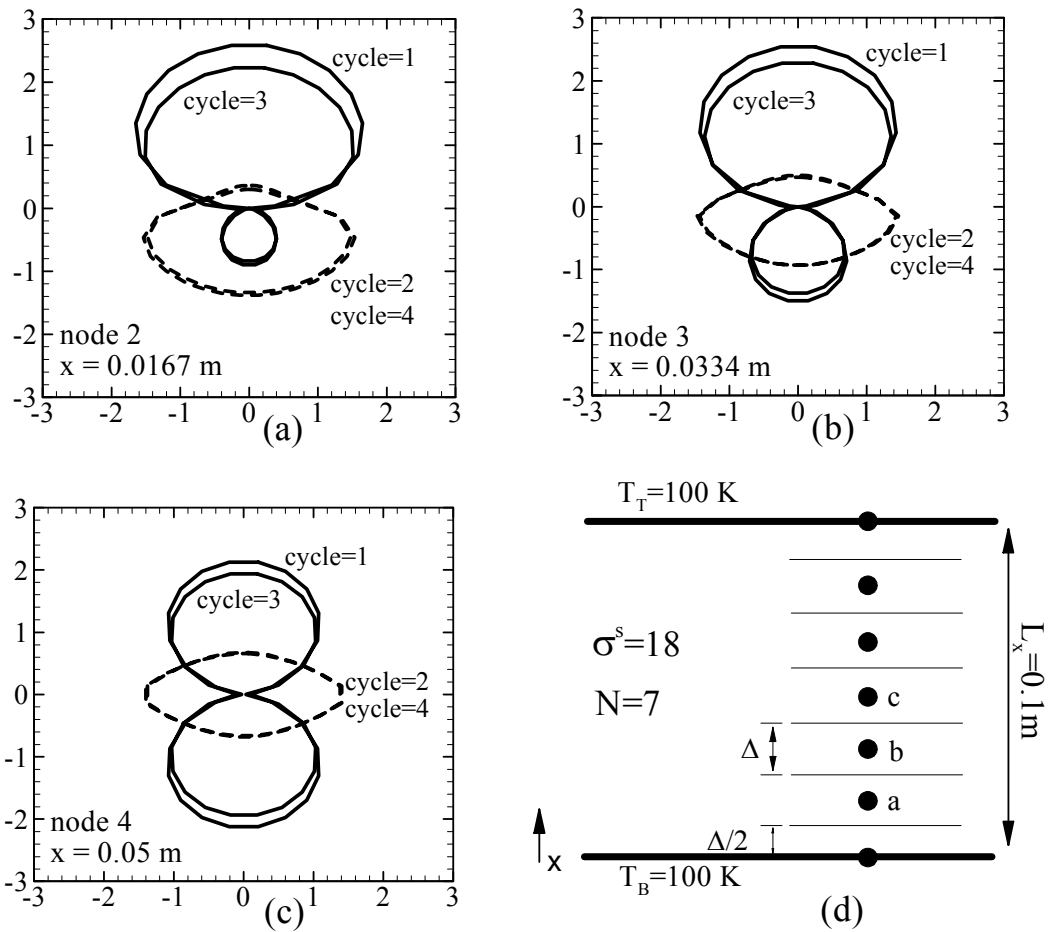


Figure A.1: The α^l distributions for the first 4 cycles in 3 nodes for $\sigma^s \Delta = 0.3$.

where i refers to the control volume index. Eqs.(A.9), (A.10) and (A.11) are matrices of coefficients for the first 3 cycles:

$$[A]_1 = \begin{bmatrix} 7.3 & -1.6 & 0 & 0 & 0 & 0 & 0 \\ -6.4 & 8.1 & -2.8 & 0 & 0 & 0 & 0 \\ 0 & -6.5 & 8.6 & -4.4 & 0 & 0 & 0 \\ 0 & 0 & -5.8 & 8.8 & -5.8 & 0 & 0 \\ 0 & 0 & 0 & -4.4 & 8.6 & -6.5 & 0 \\ 0 & 0 & 0 & 0 & -2.8 & 8.1 & -6.4 \\ 0 & 0 & 0 & 0 & 0 & -1.6 & 7.3 \end{bmatrix} \quad (\text{A.9})$$

$$[A]_2 = \begin{bmatrix} 6.7 & -4.7 & 0 & 0 & 0 & 0 & 0 \\ -0.6 & 6.0 & -3.5 & 0 & 0 & 0 & 0 \\ 0 & -1.3 & 5.5 & -2.7 & 0 & 0 & 0 \\ 0 & 0 & -2.0 & 5.4 & -2.0 & 0 & 0 \\ 0 & 0 & 0 & -2.7 & 5.5 & -1.3 & 0 \\ 0 & 0 & 0 & 0 & -3.5 & 6.0 & -0.6 \\ 0 & 0 & 0 & 0 & 0 & -4.7 & 6.7 \end{bmatrix} \quad (\text{A.10})$$

$$[A]_3 = \begin{bmatrix} 6.5 & -1.7 & 0 & 0 & 0 & 0 & 0 \\ -5.1 & 7.6 & -2.8 & 0 & 0 & 0 & 0 \\ 0 & -5.9 & 8.2 & -4.2 & 0 & 0 & 0 \\ 0 & 0 & -5.6 & 8.5 & -5.6 & 0 & 0 \\ 0 & 0 & 0 & -4.2 & 8.2 & -5.9 & 0 \\ 0 & 0 & 0 & 0 & -2.8 & 7.6 & -5.1 \\ 0 & 0 & 0 & 0 & 0 & -1.7 & 6.5 \end{bmatrix} \quad (\text{A.11})$$

It is very important to understand that the $[A]$ matrices are influenced by the α^l distributions. According to the multiplicative method formulation (Eqs.(A.6) and (A.7)), the coefficients for the control volume of the node P are

$$\begin{aligned} a_P &= \sum_L \alpha_P^l \hat{a}_P^l \\ a_N &= \sum_{\mathbf{s}^l \cdot \mathbf{e}_1 < 0} \alpha_N^l a_N^l \\ a_S &= \sum_{\mathbf{s}^l \cdot \mathbf{e}_1 > 0} \alpha_S^l a_S^l \end{aligned}$$

where $\mathbf{s}^l \cdot \mathbf{e}_1 > 0$ implies summation only on \mathbf{s} directions that are upward. When an

upwind differencing scheme is used, the a^l coefficients are

$$\begin{aligned}\widehat{a}_P^l &= \max[-\mathbf{N}^l \cdot \mathbf{e}_1, \mathbf{N}^l \cdot \mathbf{e}_1] = |\mathbf{N}^l| \\ a_N^l &= \max[-\mathbf{N}^l \cdot \mathbf{e}_1, 0] \\ a_S^l &= \max[\mathbf{N}^l \cdot \mathbf{e}_1, 0]\end{aligned}\tag{A.12}$$

where $\mathbf{N}^l = \int_{\omega^l} \mathbf{s} d\omega$. Therefore

$$\begin{aligned}a_P &= \sum_L |\mathbf{N}^l| \alpha_P^l \\ a_S &= \sum_{\mathbf{s}^l \cdot \mathbf{e}_1 > 0} |\mathbf{N}^l| \alpha_S^l \\ a_N &= \sum_{\mathbf{s}^l \cdot \mathbf{e}_1 < 0} |\mathbf{N}^l| \alpha_N^l\end{aligned}\tag{A.13}$$

Since the $|\mathbf{N}^l|$ values in each direction are equivalent in these coefficients, the relative magnitudes of the a coefficients only vary with the α^l distribution.

Now we can consider the connection between the $[A]$ matrices and the α^l distributions with an example. For the third node, $i = 3$, the coefficients are

$$\begin{aligned}A_1(3, 3) &= a_P^3 = \sum_L |\mathbf{N}^l| \alpha_3^l \\ A_1(3, 2) &= -a_S^3 = - \sum_{\mathbf{s}^l \cdot \mathbf{e}_1 > 0} |\mathbf{N}^l| \alpha_2^l \\ A_1(3, 4) &= -a_N^3 = - \sum_{\mathbf{s}^l \cdot \mathbf{e}_1 < 0} |\mathbf{N}^l| \alpha_4^l\end{aligned}\tag{A.14}$$

Fig.A.1 shows that in the first cycle, the α^l values at the second node (α_2^l) in the upward directions are larger than the α^l values in the fourth node (α_4^l) in the downward directions. Looking at Eqs.(A.14) shows that $\alpha_2^l > \alpha_4^l$ results in $a_S^3 > a_N^3$. Therefore, in the third row of the $[A]_1$ matrix $a_S > a_N$ ($|A_1(3, 2)| > |A_1(3, 4)|$). As another example, Fig.A.1 depicts that in the second cycle, the α^l values at the second node in the upward directions are smaller than the α^l values at the fourth node in the downward directions. As a result, $a_N > a_S$ ($|A_2(3, 2)| < |A_2(3, 4)|$) at the third node in the second cycle (third row of the $[A]_2$ matrix).

The I_a Distribution: I_a (obtained in Step 6 from the implicit equation) across the medium in each cycle has been plotted in Fig.A.2. I_a is scaled by σT_B^4 and x is scaled by L_x , and are denoted by I_a^* and x^* in the figure, respectively.

Discussion

Now we have enough information to discuss the observed fluctuations and the poor convergence. Solving the RTE in Step 2 gives the I^l values which are integrated in Step 3 to find the \tilde{I}_a values in the first cycle. Then α^l values are calculated in Step 4 which are shown in Fig.A.1 (the first cycle). Forming the coefficients in Step 5 results in the $[A]_1$ matrix.

Looking at the $[A]_1$ matrix shows that below the midpoint (rows 1 to 3), $a_S > a_N$ which implies transfer of energy from the bottom wall to the middle of the enclosure. For the nodes above the midpoint, $a_N > a_S$ which forces energy to transfer from the top wall to the middle of the enclosure. Therefore, the level of energy at the middle of the enclosure will be very high at the end of the first cycle. This high level of energy is observed in Fig.A.2 (I_a^* level in the first cycle).

In the second cycle, this high I_a level results in the I^l values which give the \tilde{I}_a values. The α^l distributions are then obtained which are quite different from the first cycle and the $[A]_2$ matrix is formed by these α^l values. In contrast to the first cycle, the $[A]_2$ matrix shows that in the second cycle, energy is forced to transfer from the middle towards the walls. Fig.A.2 shows that the I_a^* level in the medium at the end of the second cycle is low (the lowest curve). Again, the $[A]_3$ matrix shows that the situation in the third cycle is the same as the first one and energy is carried to the middle of the enclosure and these fluctuations continue.

Diagonal Dominance

So far we have explained the reason of the fluctuations in the phase weights and average intensity levels. Although these oscillations can be responsible for the poor convergence, it seems that they are not the only ones. These fluctuations also happen in some other cases which are damped after several cycles and the solution converges at the end (sometimes with an acceptable number of cycles).

The other important issue is the lack of diagonal dominance which was first mentioned by Raithby and Chui [42]. It is clear that the $[A]_1$ and $[A]_3$ matrices are not diagonally dominant while $[A]_2$ is. In fact, the condition number of $[A]_1$ is 549 and the condition number of $[A]_3$ is 252. Condition numbers of the $[A]_2$ and $[A]_4$ matrices are smaller than 10. It can be concluded that the lack of diagonal dominance in the odd cycles intensifies the fluctuations and destroys the convergence.

Now the question is what causes the lack of diagonal dominance. Fig.A.3 shows the phase weight profiles schematically for a node at the center of the enclosure

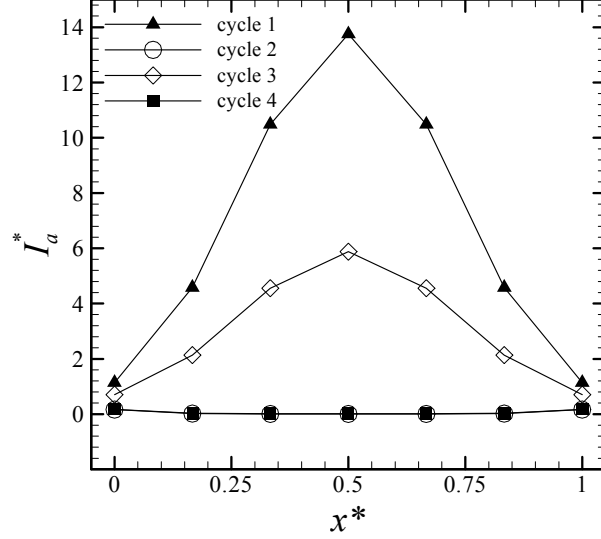


Figure A.2: Scaled I_a distributions across the enclosure for the first 4 iterations.

(node P) and its neighbors (named N and S). This distribution is the same as solid-line profiles in Fig.A.1 (cycles 1 and 3) where the $[A]$ matrices are not diagonally dominant.

The a^l and a coefficients were given before (Eqs.(A.12) and (A.13)). From Eq.(A.13):

$$\begin{aligned}
 a_P &= \sum_L |\mathbf{N}^l| \alpha_P^l \propto (R_1 + R_3) \\
 a_S &= \sum_{s^l \cdot \mathbf{e}_1 > 0} |\mathbf{N}^l| \alpha_S^l \propto R_2 \\
 a_N &= \sum_{s^l \cdot \mathbf{e}_1 < 0} |\mathbf{N}^l| \alpha_N^l \propto R_4
 \end{aligned}$$

where the R values are proportional to the magnitudes of the α^l distribution indicated by regions 1, 2, 3 and 4 in Fig.A.1. Since $(R_2 = R_4) > (R_1 = R_3)$ (from Fig.A.3), it is obvious that $a_S + a_N$ will be larger than a_P . This shows why the $[A]_1$ and $[A]_3$ matrices are not diagonally dominant ($a_P < a_S + a_N$).

This very simple 1D example shows clearly the reasons of bouncing in residuals and also the lack of diagonal dominance. All observations and conclusions in this

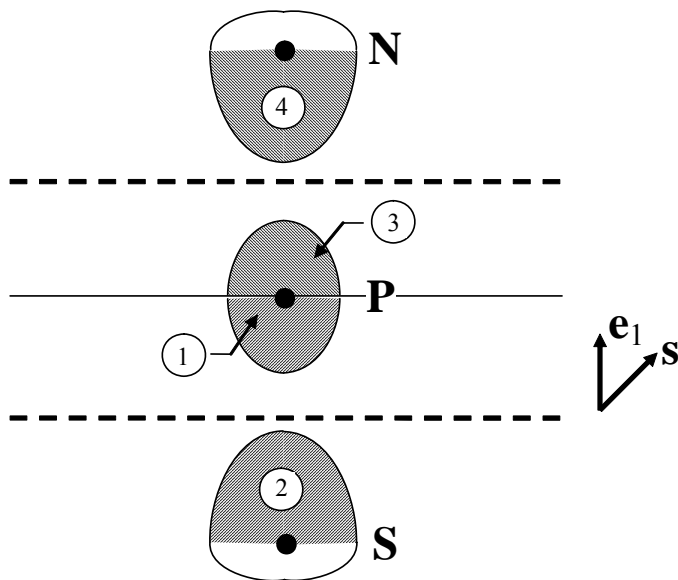


Figure A.3: Schematic α^l profiles at 3 nodes in the middle of the enclosure

example are consistent with what Raithby and Chui [42] found in the 2D problem.

A.4 Other Differencing Schemes

Until now only the UDS has been used in studies focused on the performance of the multiplicative method [41, 42]. It is also interesting to consider discretization methods other than the upwind scheme in the multiplicative method to see the effect of the differencing scheme on the performance; and also to ensure that the poor convergence is not caused by the upwind scheme.

To study a more strongly coupled scheme, the second-order exponential scheme of Raithby and Chui [15] has been used to solve the 1D problem (the illustrative example). The only difference is that here, $T_B = 100$ K and $T_T = 0$ K. In the exponential scheme, the intensity in an integration point is approximated by the analytical solution of the RTE between the upstream node and the integration point.

Table A.2 compares the multiplicative method performance for two different schemes: the upwind scheme and the exponential scheme. Table A.2 shows that

Table A.2: Number of cycles to achieve convergence in a 1D problem for the multiplicative method with the upwind and exponential schemes.

	$\sigma^s \Delta$									
Grid	0.001	0.01	0.05	0.10	0.25	0.5	1.0	5.0	10	100
<i>Upwind Scheme</i>										
5	4	6	8	10	13	14	13	8	7	4
10	4	7	11	16	25	30	22	9	7	4
25	5	9	25	132	/	/	76	9	7	4
50	6	12	/	/	/	/	/	10	7	4
100	7	20	/	/	/	/	/	10	7	4
<i>Exponential Scheme</i>										
5	4	5	8	9	12	14	12	5	4	2
10	4	6	11	15	27	33	19	5	4	2
25	5	9	24	/	/	/	35	5	4	2
50	5	12	/	/	/	/	53	5	4	2
100	7	20	/	/	/	/	77	5	4	2

the range of $0.05 \leq \sigma^s \Delta \leq 1$ for poor convergence is common between the 1D and 2D problems with different differencing schemes.

A.5 Concluding Remarks

In this appendix, the effectiveness of the multiplicative method in accelerating the RTE solution was studied. It was shown that this method fails to produce convergence in the intermediate optical thickness range ($0.05 \leq \sigma^s \Delta \leq 1$) for fine grids. The explanation given before in the literature was verified by a simple example. Looking at the matrices of coefficients, α^l profiles and I_a levels simultaneously showed the physical reason behind the fluctuations which cause the poor convergence. Also the lack of diagonal dominance, which intensifies the fluctuations, was discussed and explained. At the end, it was shown by a 1D problem that the poor convergence is not limited to the upwind differencing scheme, and the range that this breakdown happens is common between the upwind and exponential schemes.

Appendix B

Two-Dimensional Discretization

In this appendix, the complete discretization of the Q_L equations for a 2D Cartesian grid is presented. The 2D Cartesian grid, which has been used in this research, was explained in Chapter 3 (Figs.3.2 and 3.3).

As explained in Chapter 2, in the Q_L method, \mathbf{q}_{ip} is obtained from Eq.(2.22) or Eq.(2.26) and is inserted in Eq.(2.25) to form Eq.(2.27). The aim of this appendix is to find the coefficients and source term of Eq.(2.27) for the interior and boundary control volumes for the general case.

B.1 Interior Control Volumes

Starting from the interior control volumes, inserting Eq.(2.22) in Eq.(2.25) gives

$$\sum_{ip} \left[\frac{-1}{\kappa} \frac{\partial}{\partial x_j} (I_a T_{ij}) + \Omega (I_a S_i) \right] \mathbf{e}_i \cdot \mathbf{n}_{ip} A_{s,ip} = 4\pi K_P V_P (I_{b,P} - I_{a,P}) \quad (\text{B.1})$$

where T_{ij} and S_i were defined before by Eqs.(2.20) and (2.21) as

$$T_{ij} = \sum_{l=1}^L \alpha^l D_{ij}^l$$

and

$$S_i = \sum_{l'=1}^L \alpha^{l'} F_i^{l'}$$

Each of these variables has two parts: one part which does not change during the iterative solution and is calculated and stored at the beginning of the solution (D_{ij}^l and F_i^l) and the other part, α^l , which changes during the solution. Therefore, T_{ij} and S_i should be updated once a new α^l distribution is obtained.

D_{ij}^l and F_i^l are easily calculated by exact or precise numerical integration at the beginning of the solution. D_{ij}^l is independent of the spatial position and depends only on the angular grid:

$$D_{ij}^l = \int_{\omega^l} s_i s_j d\omega$$

It is known that (Fig.B.1 (a))

$$\begin{aligned} \mathbf{s} &= s_1 \mathbf{e}_1 + s_2 \mathbf{e}_2 + s_3 \mathbf{e}_3 \\ &= \sin(\theta) \cos(\phi) \mathbf{e}_1 + \sin(\theta) \sin(\phi) \mathbf{e}_2 + \cos(\theta) \mathbf{e}_3 \end{aligned}$$

Therefore

$$\begin{aligned} D_{11}^l &= \int_{\omega^l} s_1 s_1 d\omega = \int_{\phi_-^l}^{\phi_+^l} \int_{\theta_-^l}^{\theta_+^l} \sin^3(\theta) \cos^2(\phi) d\theta d\phi \\ &= \left[\frac{1}{3} (\cos^3(\theta_+^l) - \cos^3(\theta_-^l)) - (\cos(\theta_+^l) - \cos(\theta_-^l)) \right] \\ &\quad \times \left[\frac{1}{2} (\phi_+^l - \phi_-^l) + \frac{1}{4} (\sin(2\phi_+^l) - \sin(2\phi_-^l)) \right] \end{aligned}$$

$$\begin{aligned} D_{12}^l &= D_{21}^l = \int_{\omega^l} s_1 s_2 d\omega = \int_{\phi_-^l}^{\phi_+^l} \int_{\theta_-^l}^{\theta_+^l} \sin^3(\theta) \cos(\phi) \sin(\phi) d\theta d\phi \\ &= \left[\frac{1}{3} (\cos^3(\theta_+^l) - \cos^3(\theta_-^l)) - (\cos(\theta_+^l) - \cos(\theta_-^l)) \right] \times \left[\frac{1}{2} (\sin^2(\phi_+^l) - \sin^2(\phi_-^l)) \right] \end{aligned}$$

$$\begin{aligned} D_{22}^l &= \int_{\omega^l} s_2 s_2 d\omega = \int_{\phi_-^l}^{\phi_+^l} \int_{\theta_-^l}^{\theta_+^l} \sin^3(\theta) \sin^2(\phi) d\theta d\phi \\ &= \left[\frac{1}{3} (\cos^3(\theta_+^l) - \cos^3(\theta_-^l)) - (\cos(\theta_+^l) - \cos(\theta_-^l)) \right] \\ &\quad \times \left[\frac{1}{2} (\phi_+^l - \phi_-^l) - \frac{1}{4} (\sin(2\phi_+^l) - \sin(2\phi_-^l)) \right] \end{aligned}$$

where θ_+^l , θ_-^l , ϕ_+^l , and ϕ_-^l are limits that define the solid angle ω^l (Fig.B.1 (b)). For a 2D problem, D_{i3}^l and D_{3i}^l are not required; however, they can be easily calculated as before.

$F_i^{l'}$ depends on both of the angular grid and scattering phase function:

$$F_i^{l'} = \int_{\omega^{l'}} \left\{ \frac{1}{4\pi} \int_{4\pi} \Phi(\mathbf{s}', \mathbf{s}) s_i d\omega \right\} d\omega'$$

For the non-linear scattering phase function,

$$\Phi(\mathbf{s}', \mathbf{s}) = 1 + a_1(\mathbf{s} \cdot \mathbf{s}') + a_2(3(\mathbf{s} \cdot \mathbf{s}')^2 - 1) \quad (\text{B.2})$$

this equation becomes

$$\begin{aligned} F_i^{l'} &= \int_{\omega^{l'}} \left\{ \frac{1}{4\pi} \int_{4\pi} [1 + a_1(\mathbf{s} \cdot \mathbf{s}') + a_2(3(\mathbf{s} \cdot \mathbf{s}')^2 - 1)] s_i d\omega \right\} d\omega' \\ &= \int_{\omega^{l'}} \left\{ \frac{1}{4\pi} \int_{4\pi} a_1(\mathbf{s} \cdot \mathbf{s}') s_i d\omega \right\} d\omega' \\ &= \frac{a_1}{4\pi} \int_{\omega^{l'}} \int_{4\pi} [\sin(\theta) \cos(\phi) \sin(\theta') \cos(\phi') + \sin(\theta) \sin(\phi) \sin(\theta') \sin(\phi') \\ &\quad + \cos(\theta) \cos(\theta')] s_i d\omega d\omega' \end{aligned}$$

Notice that the isotropic and non-linear parts of the phase function (the first and third terms in Eq.(B.2)) do not contribute to $F_i^{l'}$ and their integrals are zero. Hence

$$\begin{aligned} F_1^{l'} &= \frac{a_1}{4\pi} \int_{\omega^{l'}} \int_0^{2\pi} \int_0^\pi [\sin^3(\theta) \cos^2(\phi) \sin(\theta') \cos(\phi') + \sin^3(\theta) \sin(\phi) \cos(\phi) \sin(\theta') \sin(\phi') \\ &\quad + \sin^2(\theta) \cos(\theta) \cos(\phi) \cos(\theta')] d\theta d\phi d\omega' \\ &= \frac{a_1}{4\pi} \int_{\phi_-^{l'}}^{\phi_+^{l'}} \int_{\theta_-^{l'}}^{\theta_+^{l'}} \left[\frac{4\pi}{3} \sin(\theta') \cos(\phi') \right] \sin(\theta') d\theta' d\phi' \\ &= \frac{a_1}{6} \left[(\theta_+^{l'} - \theta_-^{l'}) - \frac{1}{2} (\sin(2\theta_+^{l'}) - \sin(2\theta_-^{l'})) \right] \times (\sin(\phi_+^{l'}) - \sin(\phi_-^{l'})) \end{aligned}$$

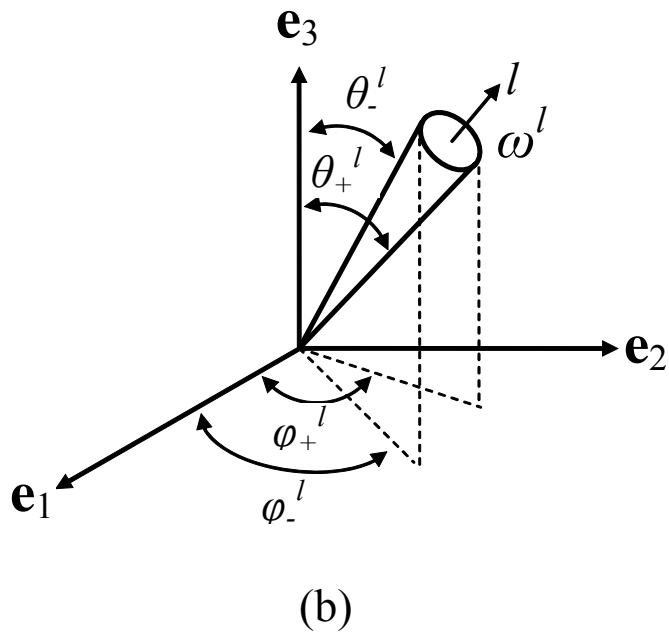
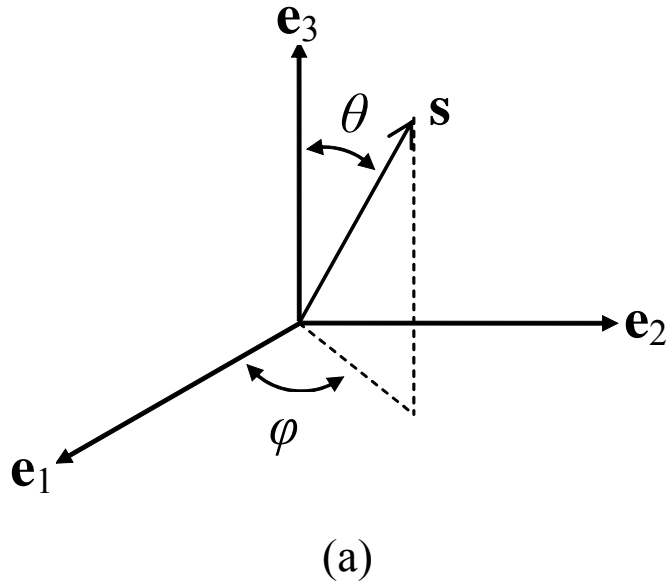


Figure B.1: The polar coordinate system (a) and a solid angle (b).

$$\begin{aligned}
F_2^{l'} &= \frac{a_1}{4\pi} \int_{\omega'} \int_0^{2\pi} \int_0^\pi \left[\sin^3(\theta) \sin(\phi) \cos(\phi) \sin(\theta') \cos(\phi') + \sin^3(\theta) \sin^2(\phi) \sin(\theta') \sin(\phi') \right. \\
&\quad \left. + \sin^2(\theta) \cos(\theta) \sin(\phi) \cos(\theta') \right] d\theta d\phi d\omega' \\
&= \frac{a_1}{4\pi} \int_{\phi_-^{l'}}^{\phi_+^{l'}} \int_{\theta_-^{l'}}^{\theta_+^{l'}} \left[\frac{4\pi}{3} \sin(\theta') \sin(\phi') \right] \sin(\theta') d\theta' d\phi' \\
&= -\frac{a_1}{6} \left[\left(\theta_+^{l'} - \theta_-^{l'} \right) - \frac{1}{2} \left(\sin(2\theta_+^{l'}) - \sin(2\theta_-^{l'}) \right) \right] \times \left(\cos(\phi_+^{l'}) - \cos(\phi_-^{l'}) \right)
\end{aligned}$$

It is important to mention that although the non-linear part of the phase function has dropped out of the Q_L equations, it still affects these equations through the α^l distribution and therefore, the Q_L method is able to predict the radiative heat transfer for non-linear phase functions accurately.

For the case of our interest, 2D Cartesian grid, Eq.(B.1) reduces to

$$\begin{aligned}
\sum_{ip=1}^8 \left\{ \left[\frac{-1}{\kappa} \left(\frac{\partial (I_a T_{11})}{\partial x_1} + \frac{\partial (I_a T_{12})}{\partial x_2} \right) + \Omega (I_a S_1) \right] \mathbf{e}_1 + \right. \\
\left. \left[\frac{-1}{\kappa} \left(\frac{\partial (I_a T_{21})}{\partial x_1} + \frac{\partial (I_a T_{22})}{\partial x_2} \right) + \Omega (I_a S_2) \right] \mathbf{e}_2 \right\} \cdot \mathbf{n}_{ip} A_{s,ip} = 4\pi K_P V_P (I_{b,P} - I_{a,P})
\end{aligned}$$

Using $x_1 = x$ and $x_2 = y$ for convenience simplifies this equation to

$$\begin{aligned}
\sum_{ip=1}^8 \left\{ \left[\frac{-1}{\kappa} \left(\frac{\partial (I_a T_{xx})}{\partial x} + \frac{\partial (I_a T_{xy})}{\partial y} \right) + \Omega (I_a S_x) \right] \mathbf{e}_1 + \right. \\
\left. \left[\frac{-1}{\kappa} \left(\frac{\partial (I_a T_{yx})}{\partial x} + \frac{\partial (I_a T_{yy})}{\partial y} \right) + \Omega (I_a S_y) \right] \mathbf{e}_2 \right\} \cdot \mathbf{n}_{ip} A_{s,ip} = 4\pi K_P V_P (I_{b,P} - I_{a,P})
\end{aligned} \tag{B.3}$$

Knowing D_{ij}^l and $F_i^{l'}$, T_{ij} and S_i are updated at all computational nodes once a new α^l distribution is obtained. To complete the discretization, the derivatives of $I_a T_{ij}$ and values of $I_a S_i$ in the left-hand side of Eq.(B.3) should be approximated based on the nodal values. These derivatives and values are approximated for each variable using linear profiles within each element. The basis of this approximation is explained in the following.

Fig.B.2 shows an element where the integration points are located at the center of the panels. A local temporary $t - s$ coordinate system is located at the center

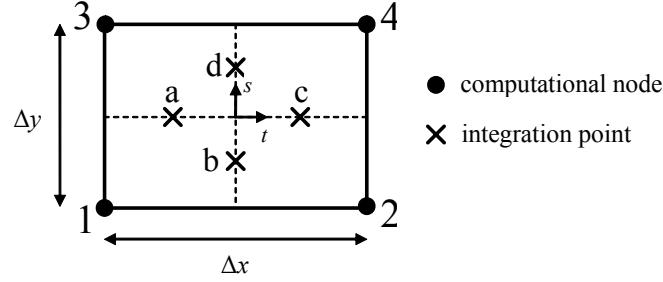


Figure B.2: A typical 2D rectangular element.

of the element where t and s both vary between -1 and 1 . Anywhere inside the element, the value of a variable J can be approximated as

$$J = \frac{(1-s)(1-t)J_1 + (1-s)(1+t)J_2 + (1+s)(1-t)J_3 + (1+s)(1+t)J_4}{4} \quad (\text{B.4})$$

where J_1 , J_2 , J_3 , and J_4 are values at the computational nodes. For example, at the integration point a , $t = -0.5$ and $s = 0$, J_a is calculated as

$$J_a = \frac{3J_1 + J_2 + 3J_3 + J_4}{8}$$

To find the derivatives at the integration points, Eq.(B.4) is differentiated with respect to x and y as

$$\frac{\partial J}{\partial x} = \frac{\partial J}{\partial t} \frac{\partial t}{\partial x} = \frac{\partial J}{\partial t} \frac{\Delta t}{\Delta x} = \frac{2}{\Delta x} \frac{\partial J}{\partial t}$$

$$\frac{\partial J}{\partial y} = \frac{\partial J}{\partial s} \frac{\partial s}{\partial y} = \frac{\partial J}{\partial s} \frac{\Delta s}{\Delta y} = \frac{2}{\Delta y} \frac{\partial J}{\partial s}$$

where

$$\frac{\partial J}{\partial t} = \frac{-(1-s)J_1 + (1-s)J_2 - (1+s)J_3 + (1+s)J_4}{4}$$

$$\frac{\partial J}{\partial s} = \frac{-(1-t)J_1 - (1+t)J_2 + (1-t)J_3 + (1+t)J_4}{4}$$

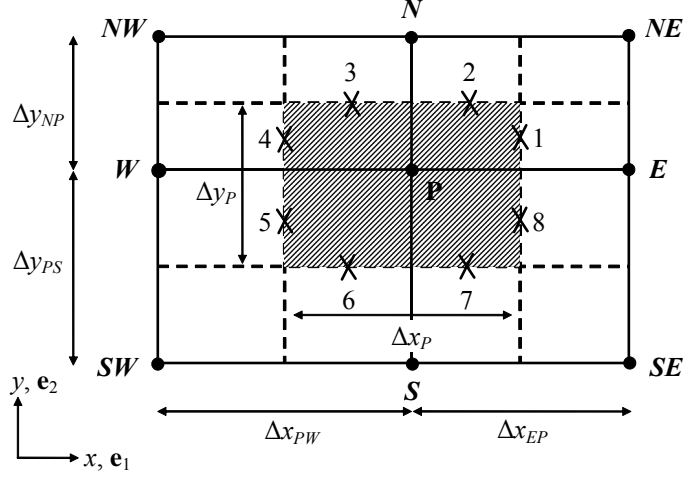


Figure B.3: An interior control volume in a 2D Cartesian grid.

Therefore

$$\begin{aligned}\frac{\partial J}{\partial x} &= \frac{-(1-s)J_1 + (1-s)J_2 - (1+s)J_3 + (1+s)J_4}{2\Delta x} \\ \frac{\partial J}{\partial y} &= \frac{-(1-t)J_1 - (1+t)J_2 + (1-t)J_3 + (1+t)J_4}{2\Delta y}\end{aligned}\quad (\text{B.5})$$

For example, at the integration point d , $t = 0$ and $s = 0.5$, derivatives are calculated as

$$\begin{aligned}\left.\frac{\partial J}{\partial x}\right|_d &= \frac{-J_1 + J_2 - 3J_3 + 3J_4}{4\Delta x} \\ \left.\frac{\partial J}{\partial y}\right|_d &= \frac{-J_1 - J_2 + J_3 + J_4}{2\Delta y}\end{aligned}$$

In Eq.(B.3), derivatives of $I_a T_{ij}$ and values of $I_a S_i$ at the integration points should be found by Eqs.(B.4) and (B.5).

A control volume in a 2D Cartesian grid was shown before in Chapter 3 and is repeated here for convenience (Fig.B.3). At $ip = 1$, $n_{ip} = \mathbf{e}_1$; therefore, the second term inside the summation in Eq.(B.3) vanishes since $\mathbf{e}_2 \cdot \mathbf{e}_1 = 0$. $ip = 1$ in element $P - E - N - NE$ in Fig.B.3 is similar to integration point “ b ” in Fig.B.2 and

nodes 1, 2, 3, and 4 in Fig.B.2 are similar to nodes P , E , N , and NE in Fig.B.3 respectively. Consequently for $ip = 1$

$$\begin{aligned}\frac{\partial (I_a T_{xx})}{\partial x} \Big|_{ip=1} &= \frac{-3(I_a T_{xx})_P + 3(I_a T_{xx})_E - (I_a T_{xx})_N + (I_a T_{xx})_{NE}}{4\Delta x_{EP}} \\ \frac{\partial (I_a T_{xy})}{\partial y} \Big|_{ip=1} &= \frac{-(I_a T_{xy})_P - (I_a T_{xy})_E + (I_a T_{xy})_N + (I_a T_{xy})_{NE}}{2\Delta y_{NP}} \\ (I_a S_x) \Big|_{ip=1} &= \frac{3(I_a S_x)_P + 3(I_a S_x)_E + (I_a S_x)_N + (I_a S_x)_{NE}}{8}\end{aligned}$$

where Δx_{EP} and Δy_{NP} are the width and height of the element (Fig.B.3).

At $ip = 2$, $n_{ip} = \mathbf{e}_2$, and this point is similar to point “a”. Therefore

$$\begin{aligned}\frac{\partial (I_a T_{yx})}{\partial x} \Big|_{ip=2} &= \frac{-(I_a T_{yx})_P + (I_a T_{yx})_E - (I_a T_{yx})_N + (I_a T_{yx})_{NE}}{2\Delta x_{EP}} \\ \frac{\partial (I_a T_{yy})}{\partial y} \Big|_{ip=2} &= \frac{-3(I_a T_{yy})_P - (I_a T_{yy})_E + 3(I_a T_{yy})_N + (I_a T_{yy})_{NE}}{4\Delta y_{NP}} \\ (I_a S_y) \Big|_{ip=2} &= \frac{3(I_a S_y)_P + (I_a S_y)_E + 3(I_a S_y)_N + (I_a S_y)_{NE}}{8}\end{aligned}$$

$ip = 3$ is in another element, $W - P - NW - N$, and is similar to point “c” in Fig.B.2. Therefore

$$\begin{aligned}\frac{\partial (I_a T_{yx})}{\partial x} \Big|_{ip=3} &= \frac{-(I_a T_{yx})_W + (I_a T_{yx})_P - (I_a T_{yx})_{NW} + (I_a T_{yx})_N}{2\Delta x_{PW}} \\ \frac{\partial (I_a T_{yy})}{\partial y} \Big|_{ip=3} &= \frac{-(I_a T_{yy})_W - 3(I_a T_{yy})_P + (I_a T_{yy})_{NW} + 3(I_a T_{yy})_N}{4\Delta y_{NP}} \\ (I_a S_y) \Big|_{ip=3} &= \frac{(I_a S_y)_W + 3(I_a S_y)_P + (I_a S_y)_{NW} + 3(I_a S_y)_N}{8}\end{aligned}$$

All derivatives and values at the other 5 integration points are calculated in the same manner. Inserting them in Eq.(B.3) results in Eq.(2.27):

$$\begin{aligned}a_P I_{a,P} &= a_N I_{a,N} + a_E I_{a,E} + a_S I_{a,S} + a_W I_{a,W} \\ &\quad + a_{NE} I_{a,NE} + a_{SE} I_{a,SE} + a_{NW} I_{a,NW} + a_{SW} I_{a,SW} + b_P\end{aligned}\quad (\text{B.6})$$

where

$$\begin{aligned}
a_P &= \frac{3}{4\kappa_P} \left[\left(\frac{\Delta y_P}{\Delta x_{EP}} + \frac{\Delta y_P}{\Delta x_{PW}} \right) T_{xx}^P + \left(\frac{\Delta x_P}{\Delta y_{NP}} + \frac{\Delta x_P}{\Delta y_{PS}} \right) T_{yy}^P \right] + 4\pi K_P \Delta x_P \Delta y_P \\
a_N &= \frac{1}{8\kappa_P} \left[- \left(\frac{\Delta y_{NP}}{\Delta x_{EP}} + \frac{\Delta y_{NP}}{\Delta x_{PW}} \right) T_{xx}^N + \frac{6\Delta x_P}{\Delta y_{NP}} T_{yy}^N \right] - \frac{3\Omega}{8} S_y^N \Delta x_P \\
a_E &= \frac{1}{8\kappa_P} \left[\frac{6\Delta y_P}{\Delta x_{EP}} T_{xx}^E - \left(\frac{\Delta x_{EP}}{\Delta y_{NP}} + \frac{\Delta x_{EP}}{\Delta y_{PS}} \right) T_{yy}^E \right] - \frac{3\Omega}{8} S_x^E \Delta y_P \\
a_S &= \frac{1}{8\kappa_P} \left[- \left(\frac{\Delta y_{PS}}{\Delta x_{PW}} + \frac{\Delta y_{PS}}{\Delta x_{EP}} \right) T_{xx}^S + \frac{6\Delta x_P}{\Delta y_{PS}} T_{yy}^S \right] + \frac{3\Omega}{8} S_y^S \Delta x_P \\
a_W &= \frac{1}{8\kappa_P} \left[\frac{6\Delta y_P}{\Delta x_{PW}} T_{xx}^W - \left(\frac{\Delta x_{PW}}{\Delta y_{NP}} + \frac{\Delta x_{PW}}{\Delta y_{PS}} \right) T_{yy}^W \right] + \frac{3\Omega}{8} S_x^W \Delta y_P \\
a_{NE} &= \frac{1}{8\kappa_P} \left[\frac{\Delta y_{NP}}{\Delta x_{EP}} T_{xx}^{NE} + 4T_{xy}^{NE} + \frac{\Delta x_{EP}}{\Delta y_{NP}} T_{yy}^{NE} \right] - \frac{\Omega}{16} (S_x^{NE} \Delta y_{NP} + S_y^{NE} \Delta x_{EP}) \\
a_{NW} &= \frac{1}{8\kappa_P} \left[\frac{\Delta y_{NP}}{\Delta x_{PW}} T_{xx}^{NW} - 4T_{xy}^{NW} + \frac{\Delta x_{PW}}{\Delta y_{NP}} T_{yy}^{NW} \right] + \frac{\Omega}{16} (S_x^{NW} \Delta y_{NP} - S_y^{NW} \Delta x_{PW}) \\
a_{SE} &= \frac{1}{8\kappa_P} \left[\frac{\Delta y_{PS}}{\Delta x_{EP}} T_{xx}^{SE} - 4T_{xy}^{SE} + \frac{\Delta x_{EP}}{\Delta y_{PS}} T_{yy}^{SE} \right] + \frac{\Omega}{16} (-S_x^{SE} \Delta y_{PS} + S_y^{SE} \Delta x_{EP}) \\
a_{SW} &= \frac{1}{8\kappa_P} \left[\frac{\Delta y_{PS}}{\Delta x_{PW}} T_{xx}^{SW} + 4T_{xy}^{SW} + \frac{\Delta x_{PW}}{\Delta y_{PS}} T_{yy}^{SW} \right] + \frac{\Omega}{16} (S_x^{SW} \Delta y_{PS} + S_y^{SW} \Delta x_{PW}) \\
b_P &= 4\pi K_P \Delta x_P \Delta y_P I_{b,P}
\end{aligned}$$

Notice that Δx_P and Δy_P are the width and height of the control volume (Fig.B.3) and are calculated as

$$\begin{aligned}
\Delta x_P &= \frac{\Delta x_{EP} + \Delta x_{PW}}{2} \\
\Delta y_P &= \frac{\Delta y_{NP} + \Delta y_{PS}}{2}
\end{aligned}$$

B.2 Boundary Control Volumes

Fig.B.4 depicts a boundary control volume. Derivatives and values at $ip = 1, 2, 7,$ and 8 are calculated exactly the same as before since they are interior integration points.

When the surface is isothermal, integration points at the boundary (at the surface) are combined to a single one at the node P since the surface emissive power (σT_s^4) is uniform. For this integration point, q_{ip} is calculated from Eq.(2.26):

$$\mathbf{q}_{ip} \cdot \mathbf{n}_{ip} = q_{ip} = \epsilon_s I_{a,p} \sum_{\mathbf{N}^l \cdot \mathbf{n}_{ip} > 0} \alpha_P^l \mathbf{N}^l \cdot \mathbf{n}_{ip} - \epsilon_s \sigma T_s^4$$

where \mathbf{N}^l is a vector and its components

$$N_i^l = \int_{\omega^l} s_i d\omega$$

are calculated as

$$\begin{aligned} N_1^l &= \int_{\omega^l} s_1 d\omega = \int_{\phi_-^l}^{\phi_+^l} \int_{\theta_-^l}^{\theta_+^l} \sin^2(\theta) \cos(\phi) d\theta d\phi \\ &= \frac{1}{4} [2(\theta_+^l - \theta_-^l) - (\sin(2\theta_+^l) - \sin(2\theta_-^l))] \times [\sin(\phi_+^l) - \sin(\phi_-^l)] \end{aligned}$$

$$\begin{aligned} N_2^l &= \int_{\omega^l} s_2 d\omega = \int_{\phi_-^l}^{\phi_+^l} \int_{\theta_-^l}^{\theta_+^l} \sin^2(\theta) \sin(\phi) d\theta d\phi \\ &= -\frac{1}{4} [2(\theta_+^l - \theta_-^l) - (\sin(2\theta_+^l) - \sin(2\theta_-^l))] \times [\cos(\phi_+^l) - \cos(\phi_-^l)] \end{aligned}$$

At the boundary integration point (at node P) shown in Fig.B.4, $n_{ip} = -\mathbf{e}_1$ and q_{ip} is calculated as

$$q_P = -\epsilon_R I_{a,p} \sum_{-\mathbf{N}^l \cdot \mathbf{e}_1 > 0} \alpha_P^l N_1^l - \epsilon_R \sigma T_R^4$$

Inserting this flux and $q_1, q_2, q_7,$ and q_8 in Eq.(2.25) gives an equation like Eq.(B.6)

in which

$$\begin{aligned}
a_P &= \frac{3}{4\kappa_P} \left[\frac{\Delta y_P}{\Delta x_{EP}} T_{xx}^P + \left(\frac{\Delta x_P}{\Delta y_{NP}} + \frac{\Delta x_P}{\Delta y_{PS}} \right) T_{yy}^P \right] + \epsilon_R C \Delta y_P + \\
&\quad \frac{3\Omega}{8} S_x^P \Delta y_P + 4\pi K_P \Delta x_P \Delta y_P \\
a_N &= \frac{1}{8\kappa_P} \left[-\frac{\Delta y_{NP}}{\Delta x_{EP}} T_{xx}^N + \frac{6\Delta x_P}{\Delta y_{NP}} T_{yy}^N \right] - \frac{\Omega}{16} (S_x^N \Delta y_{NP} + 3S_y^N \Delta x_{EP}) \\
a_S &= \frac{1}{8\kappa_P} \left[-\frac{\Delta y_{PS}}{\Delta x_{EP}} T_{xx}^S + \frac{6\Delta x_P}{\Delta y_{PS}} T_{yy}^S \right] + \frac{\Omega}{16} (-S_x^S \Delta y_{PS} + 3S_y^S \Delta x_{EP}) \\
b_P &= 4\pi K_P \Delta x_P \Delta y_P I_{b,P} + \epsilon_R \sigma T_R^4 \Delta y_P
\end{aligned}$$

where

$$C = - \sum_{-\mathbf{N}^l \cdot \mathbf{e}_1 > 0} \alpha_P^l N_1^l$$

and is positive. a_E , a_{NE} , and a_{SE} are the same as before (for interior nodes) and $a_W = a_{NW} = a_{SW} = 0$.

All coefficients and source terms in the other interior and boundary control volumes are calculated in exactly the same manner. Once those values are obtained, we will have a set of algebraic equations where the only unknowns are I_a values at the computational nodes.

B.3 The In-Scattering Term

Solving the Q_L equations gives the I_a field while the \bar{I} values are required in the FVM and generally, these two are not equal. It may be useful to show how \bar{I} can be evaluated once the I_a and α^l distributions are known.

It was shown in Eq.(1.7) that

$$\bar{I}_P^l = \frac{1}{4\pi} \sum_{l'=1}^L I_P^{l'} \bar{\Phi}^{l'l}$$

By using $I_P^{l'} = \alpha_P^{l'} I_{a,P}$ from Eq.(2.11), this equation becomes

$$\bar{I}_P^l = \frac{1}{4\pi} I_{a,P} \sum_{l'=1}^L \alpha_P^{l'} \bar{\Phi}^{l'l} \quad (\text{B.7})$$

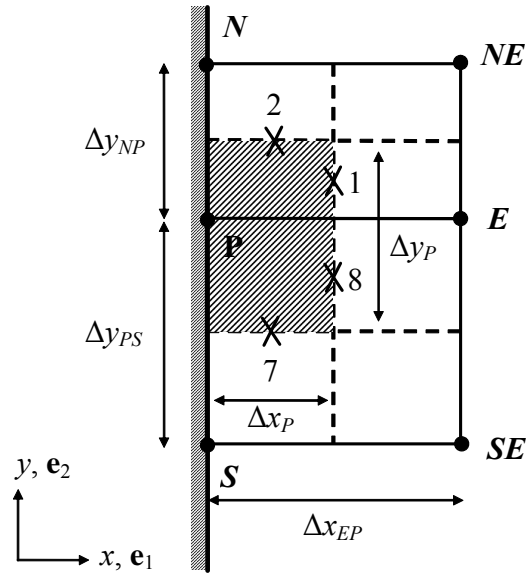


Figure B.4: A boundary control volume in a 2D Cartesian grid.

which relates the \bar{I} values to the I_a field.

Appendix C

Acceleration of the P_1 Solution

The P_1 method converts the governing equations of thermal radiation from very complex integro-differential equations to relatively simple partial differential equations with an elliptic nature. These equations are easily solved by iterative solvers; but the only problem is the slow convergence rate, especially when the optical thickness is small. The boundary condition, which is of the third kind, is culprit for this slow convergence rate. A connected problem is that the unconverged solution of the P_1 equations does not satisfy the conservation of radiant energy over the solution domain; therefore, when the P_1 method is coupled with a fluid flow solver, the total energy is not conserved over the solution domain, which adversely affects the convergence rate of the fluid flow and heat transfer solution.

These two problems have been studied by Li and Modest [68]. They proposed a multiplicative correction factor to ensure the satisfaction of the radiant energy over the solution domain which is also shown to accelerate the convergence rate substantially. This method is introduced as a reduced mesh rebalance method and the correction factor is interpreted as a uniform phase weight. This corrective procedure has been employed recently in parallelization of the P_1 method by Krishnamoorthy and co-workers [69].

This appendix may be seen irrelevant to the rest of this thesis which is about the Q_L method; but in fact, there are two reasons which make it valuable to study the convergence rate and conservation of the radiant energy in the P_1 solution:

1. In spite of the limitations and disadvantages of the P_1 method, which were explained in Chapter 1, this method is popular and widely used because of its simplicity and low solution cost.

2. The P_1 and Q_L equations have very similar natures: the Q_L solution has a very slow convergence rate in the optically thin limit and its unconverged solution does not conserve the energy over the solution domain too. Therefore, studying the P_1 method can help in improving the Q_L method.

To overcome the problem of slow convergence in the Q_L method, the additive correction multigrid solver was employed in this research which showed a satisfactory performance. It is interesting to explore the performance of the multigrid solver in the P_1 method and compare it with the performance of the correction method of Li and Modest [68].

C.1 The P_1 Equations

The P_1 equations are derived by using the Spherical Harmonics in a tedious procedure [3]. But in Chapter 2 of this thesis, a new very simple derivation procedure was introduced which gives the P_1 equations for the interior control volumes (Eq.(2.17)). In fact, using $\alpha = 1$ ($I = I_a$) in the Q_L equations gives the P_1 equations in the interior control volumes. The boundary conditions are different and the boundary condition of the P_1 method is

$$q = -\frac{2\epsilon_s}{(2 - \epsilon_s)} (\sigma T_s^4 - \pi I_a) \quad (\text{C.1})$$

C.2 Correction Method

The correction method of Li and Modest [68] is explained in this section. Conservation of the radiant energy over a control volume requires (see Chapter 2)

$$\int_{A_{s,P}} \mathbf{q} \cdot \mathbf{n} dA_s = -4\pi \int_{V_P} K (I_a - I_b) dV$$

Summing this equation over all control volume results in an equation for the radiant energy balance over the solution domain:

$$\int_{A_{s,\mathbb{R}}} \mathbf{q} \cdot \mathbf{n} dA_s = -4\pi \int_{V_{\mathbb{R}}} K (I_a - I_b) dV \quad (\text{C.2})$$

where $A_{s,\mathfrak{R}}$ and $V_{\mathfrak{R}}$ are the surface area and volume of the solution domain. Using Eq.(C.1) in the left-hand side, Eq.(C.2) in the discrete form becomes

$$-\sum_{j=1}^M \frac{2\epsilon_{s,j}}{(2-\epsilon_{s,j})} (\sigma T_{s,j}^4 - \pi I_{a,j}) A_{s,j} = -\sum_{i=1}^N 4\pi K (I_{a,i} - I_{b,i}) V_i \quad (\text{C.3})$$

where N is total number of control volumes in the solution domain and M is the number of boundary control volumes. While a converged solution satisfies this equation, an unconverged solution during the iterative solution does not. As mentioned before, this can adversely affect the convergence rate and the total energy balance over the solution domain in a coupled solution of a fluid flow and heat transfer problem.

In the correction method, satisfaction of Eq.(C.3) is used as a constraint to ensure that the radiant energy is conserved in each iteration. This is done by correcting the calculated I_a values by a uniform correction factor f , in a way that Eq.(C.3) is satisfied:

$$-\sum_{j=1}^M \frac{2\epsilon_{s,j}}{(2-\epsilon_{s,j})} (\sigma T_{s,j}^4 - \pi f I_{a,j}) A_{s,j} = -\sum_{i=1}^N 4\pi K (f I_{a,i} - I_{b,i}) V_i$$

Hence f in each iteration can be found from this equation as

$$f = \frac{\sum_{j=1}^M \frac{2\epsilon_{s,j}}{(2-\epsilon_{s,j})} \sigma T_{s,j}^4 A_{s,j} + \sum_{i=1}^N 4\pi K I_{b,i} V_i}{\sum_{j=1}^M \frac{2\pi\epsilon_{s,j}}{(2-\epsilon_{s,j})} I_{a,j} A_{s,j} + \sum_{i=1}^N 4\pi K I_{a,i} V_i}$$

This correction factor is calculated once a new I_a field is obtained, and then is used to modify the I_a field:

$$I_{a,i} = f \times I_{a,i} \quad i = 1, 2, \dots, N$$

Li and Modest [68] applied this method to a 2D problem, a cylindrical combustion chamber, with a known temperature distribution and compared the number of iterations for the Gauss-Seidel and alternating direction line-by-line TDMA iterative methods with block correction with and without the correction method. They showed that the correction method can reduce the number of iterations dramatically, especially for small optical thicknesses.

In this appendix, a simple 2D test case is studied with three solvers: the Gauss-Seidel solver, the Gauss-Seidel solver with the correction method, and the additive correction multigrid solver. The convergence rate, solution cost, and conservation of radiant energy over the domain is studied for a wide range of optical thicknesses.

C.3 Test Case

This test case is the same as Case 6 in Chapter 4. An emitting-absorbing medium in radiative equilibrium is enclosed in a square enclosure where the bottom surface is hot $T_B = T_h = 100$ K and the other three surfaces are cold $T_c = 0$ K.

$N_x \times N_y = 64 \times 64$ control volumes are used where in the multigrid solver, blocks are 2×2 and the coarsest mesh consists of one control volume, the solution domain (7 levels). The computational grid, convergence criteria, and multigrid solver are the same as Chapter 3. One iteration in the multigrid solver is defined as doing one fixed V cycle. In the Gauss-Seidel solver, sweeps are done from the bottom-left corner to the top-right corner once in each iteration. Solution cost is measured by work unit and 1WU for a specified grid is defined as the computational effort required to do 1000 Gauss-Seidel iterations.

The three solvers used in this problem are indicated by GS (w/o. correction), which means the Gauss-Seidel solver without the correction method; GS (w. correction), which means the Gauss-Seidel solver with the correction method; and Multigrid, refers to the additive correction multigrid solver.

Table C.1 reports the number of iterations and work units for four optical thicknesses: $\kappa^* = 0.01, 0.1, 1, \text{ and } 10$, for black and partially reflecting surfaces. It is seen that using the Gauss-Seidel solver with the correction method can substantially improve the convergence rate and reduce the solution cost, especially for small optical thicknesses. However, these results also show that the multigrid solver has a much better performance than the Gauss-Seidel solver with the correction method and the solution cost is much lower. Fig.C.1 shows the scaled maximum residual versus iteration for these four optical thicknesses. The enormous improvement in the convergence rate with the multigrid solver is obvious. These comparisons demonstrate the great advantage of using the multigrid solver.

The other important issue is conservation of energy over the solution domain which will be considered in the following.

In the radiative equilibrium condition, $I_a = I_b$, the radiant source term, right-hand side of Eq.(C.3), is zero. Therefore, conservation of radiant energy over the solution domain requires the radiative heat transfer over the domain (left-hand side of Eq.(C.3)) to be zero. Fig.C.2 plots this term versus iteration for $\kappa^* = 1$. Since the desired value for this term is zero, any deviation from zero can be interpreted as error. As expected, the converged solutions of all three solvers satisfy the conservation of radiant energy over the domain. But during the iterative solution, the Gauss-Seidel solver without the correction method does not conserve the energy

Scaled Maximum Residual vs. Iteration

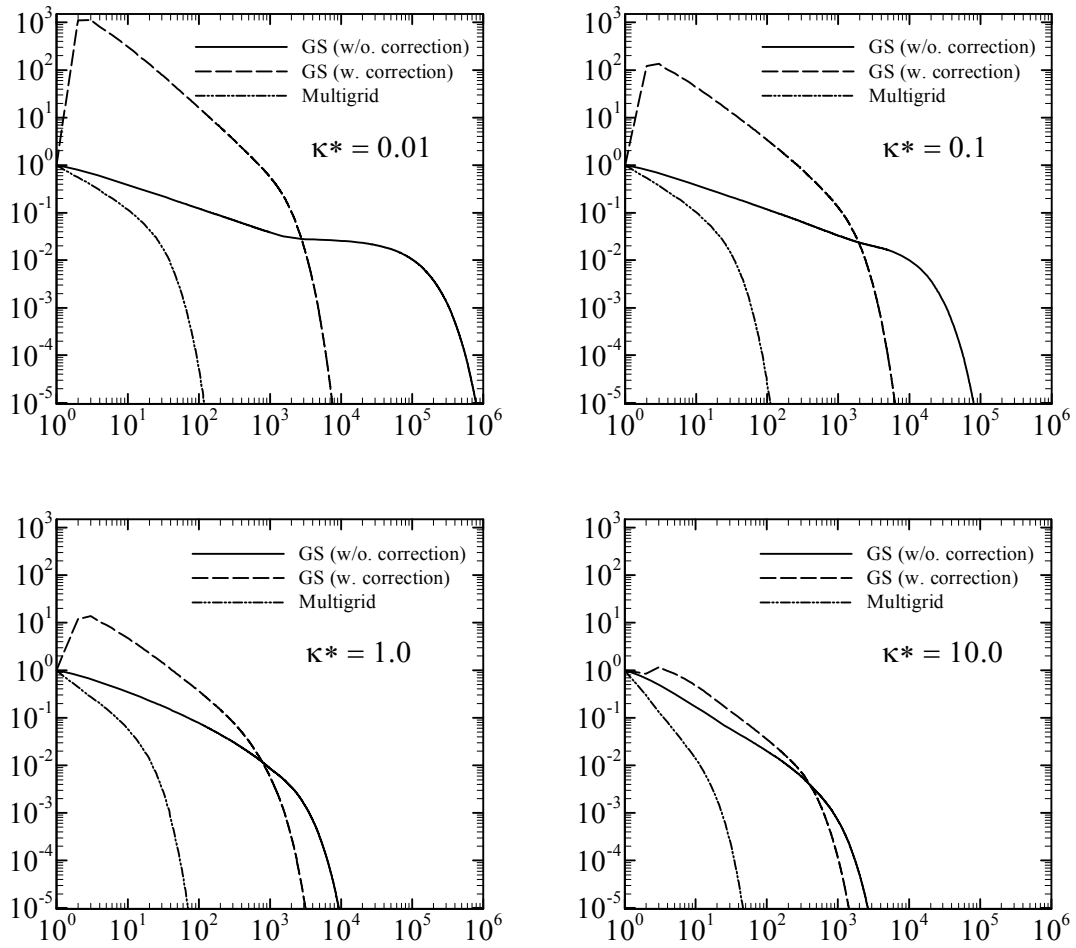


Figure C.1: Scaled maximum residual of the P_1 method with the Gauss-Seidel solver without the correction method, Gauss-Seidel solver with the correction method, and multigrid solver applied to an emitting-absorbing medium enclosed in a square enclosure with black surfaces.

Table C.1: Performance of three solvers in the P_1 method applied to an emitting-absorbing medium enclosed in a square enclosure.

		GS (w/o. correction)		GS (w. correction)		Multigrid	
κ^*	ϵ_s	it	WU	it	WU	it	WU
0.01	1	790479	794.7	7531	8.1	120	0.5
0.1	1	80216	80.3	6242	6.6	111	0.4
1	0.1	151244	151.0	6771	7.2	115	0.4
	0.5	24963	25.0	4807	5.1	94	0.4
	1	9328	9.3	3175	3.4	71	0.3
10	1	2640	2.6	1423	1.5	47	0.2

and the error is large. The multigrid solver does not conserve the energy either, but it has a very fast convergence rate and its error is small.

Fig.C.2 presents the radiative heat transfer before the correction for the Gauss-Seidel solver with the correction method. After correcting the I_a field, the Gauss-Seidel solver with the correction method does conserve the radiant energy over the solution domain and the radiative heat transfer over the solution domain will be equal to the radiant source term.

C.4 Concluding Remarks

It was shown in this appendix that the additive correction multigrid solver has a better performance in solving the P_1 equations than the Gauss-Seidel with the correction method. Conservation of radiant energy over the domain was also discussed and it was shown that the correction method guarantees this conservation while the multigrid solver does not. At the end it should be mentioned that to compare the real performance of the correction method and multigrid solver, they should be applied to non-equilibrium problems (i.e. when radiation is coupled with internal energy).

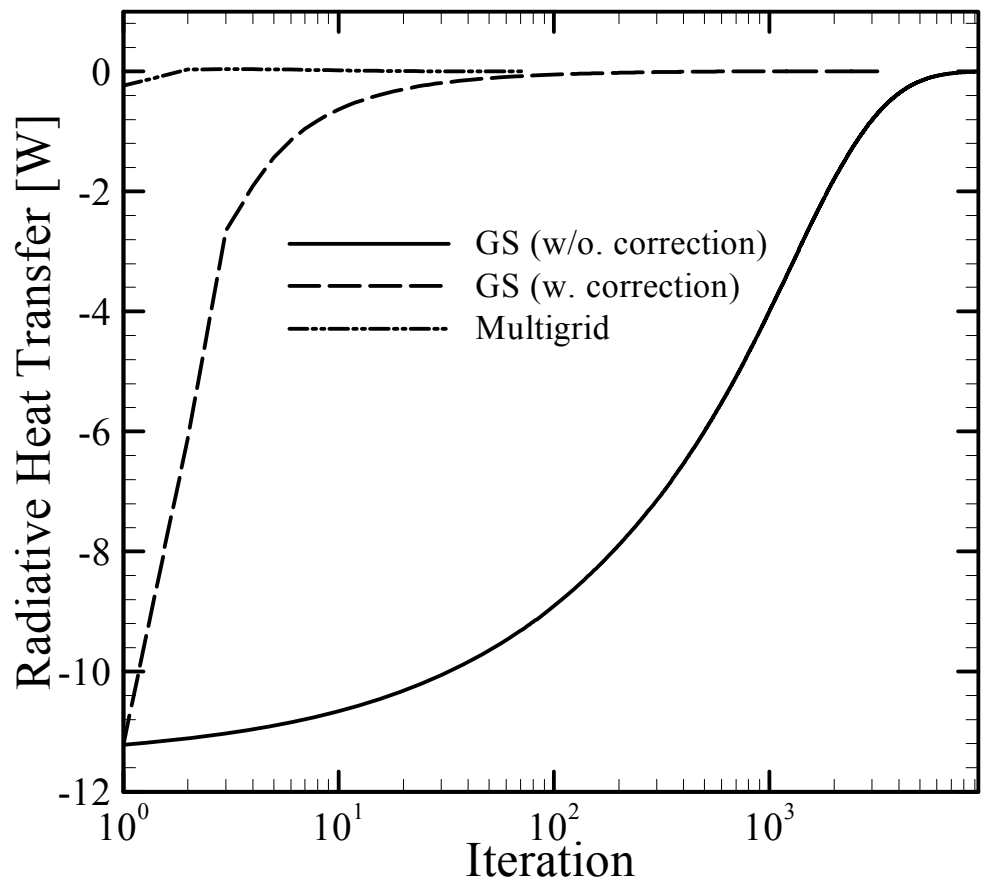


Figure C.2: Radiative heat transfer over the solution domain for $\kappa^* = 1$ obtained by the P_1 method with three solvers.